Large-area cell-tracking cytometry for biophysical measurements of single cells

by

Nicha Apichitsopa

B.S. Electrical Engineering
Johns Hopkins University, 2014
S.M. Electrical Engineering and Computer Science
Massachusetts Institute of Technology, 2016

SUBMITTED TO THE DEPARTMENT OF ELECTRICAL ENGINEERING AND COMPUTER SCIENCE IN PARTIAL FULFILLMENT OF THE REQUIREMENTS FOR THE DEGREE OF

DOCTOR OF PHILOSOPHY

AT THE

MASSACHUSETTS INSTITUTE OF TECHNOLOGY

May 2020

Author_____

Nicha Apichitsopa
Department of Electrical Engineering and Computer Science
May 15, 2020

Certified by_____

Joel Voldman
Professor of Electrical Engineering and Computer Science
Thesis Supervisor

Accepted by_____

Leslie A. Kolodziejski
Professor of Electrical Engineering and Computer Science
Chair, Department Committee on Graduate Students

Large-area cell-tracking cytometry for biophysical measurements of single cells

by

Nicha Apichitsopa

Submitted to the Department of Electrical Engineering and Computer Science
on May 15, 2020, in partial fulfillment of the requirements for the degree of
Doctor of Philosophy in Electrical Engineering and Computer Science

ABSTRACT

Utility of single-cell biophysical markers is often limited due to the low-specificity nature of biophysical markers and lack of existing techniques which can test multiple biophysical characteristics for single cells. To address this challenge, I developed a multiparameter intrinsic cytometry approach which integrates multiple label-free biophysical measurements into a versatile (can combine techniques across domains) and readily extensible (to measure more than two biophysical markers) platform for single cell analysis. The proposed multiparameter cell-tracking intrinsic cytometry utilizes label-free microfluidic techniques to manipulate cells such that information regarding their biophysical properties can be extracted from their spatiotemporal positions. Furthermore, this technique utilizes cell tracking to extract and associate the biophysical markers for single cells. The specific instantiation of the cytometry platform can measure up to five intrinsic markers of cells, and has facilitated the quantitative investigation of label-free cell profiles and classification of cell types and functional states. The applications of this approach were extended by leveraging digital holographic microscopy and deep learning technologies to monitor cells in a large field of view, enabling rapid and high-throughput assessment of biophysical phenotypes.

Thesis Supervisor: Joel Voldman
Title: Professor of Electrical Engineering and Computer Science

ACKNOWLEDGEMENTS

During the course of my PhD, I have encountered many fantastic individuals who have helped me either directly or indirectly to make this work possible.

First and foremost, I would like to express my deepest gratitude to my advisor, Professor Joel Voldman, for giving me the opportunity to join his group, and to work on this fun and exciting project. He is an amazing mentor and teacher, and a role model for me to become a critical thinker and an efficient communicator. His knowledge, technical insights, encouragement, and continual support during my years at MIT have guided me through this incredible scientific journey and helped me grow professionally. The perfect balance of freedom and supervision through his mentorship has allowed me to explore vast ranges of exciting topics and to refine my passion and research skillsets. I feel privileged to join his group, and I could not have imagined having a better mentor for my graduate study.

Secondly, I wish to thank all of my previous and current fellow lab mates in the Voldman group for the stimulating and supportive lab environment; for showing me the true meaning of perseverance and intelligence; and for making all stages of my PhD journey more enjoyable. I owe special thanks to Sarvesh Varma, Dan Wu, Haowei Su, Burak Dura, Aalap Dighe, Per Augustsson, Ismail Degani, and Jaemyon Lee, for providing me with wonderful ideas, insightful knowledge, and helpful feedbacks for the project. Of equally great values to me, I thank Alex Jaffe, Kruthika Kikkeri, Wei Liao, Yu Ting Chow (Bill), Dohyun Lee, Mahdi Aeinehvand, and Dousabel May Yi Tay, for bringing colorful uniqueness and joy to my everyday at school and for always being there when I asked for help.

I owed many thanks to the outstanding MTL staff and specialists, especially Dennis Ward, Dave Terry, and Kurt Broderick, for teaching me how to use the cleanroom equipment and for always providing me with the help and the useful tips for successful microfabrication processess.

I would also like to thank all my housemates for making the house feel like a home away from home through fun and relaxing activities. I thank all my friends at MIT and elsewhere who have never been short support and encouragement.

Last but not least, I thank my extended family, especially my parents and my brother, for their unconditional love and care. I also thank my fiancé, Chukiat Phonsom, for being my rock, my safe place, and my best cheerleader.

Table of Contents

Chapter 1

Introduction and Background

1.1 Extrinsic and Intrinsic Properties of Cells

Cells possess continuously changing biochemical and biophysical characteristics that allow them to perform specialized functions, respond to external environment, and maintain homeostasis.[1,2] They sense external cues through intricate networks of cell receptors and biochemical cascades, and respond by intracellular chemical and/or physical modification.[3,4] In addition to cellular processes (e.g., growth, division, and differentiation), pathological conditions (e.g., cancer and microbial infections) can affect and are influenced by the biochemical and the biophysical characteristics of cells to varying extents. The ability to detect these characteristics in single cells is therefore essential for the understanding of cell behaviors and disease diagnosis.

On one hand, biochemical properties (i.e., extrinsic properties) quantify the abundance and distribution of biochemical contents of cells, including proteins, RNA, DNA, reactive oxygen species, and physiologically important ions. As biochemical properties can be directly linked to specific pathways, they are highly informative and highly specific indicators of cellular functions and activities. Several analysis tools, e.g., fluorescence microscopy, flow cytometry, and mass cytometry, in conjunction with their corresponding extrinsic biochemical detection tags, e.g., fluorochromes and heavy metal ions, have been developed and are commercially available for quantifying many biochemical features in parallel.[5–8] Flow cytometry, in particular, is capable of high-content, high-throughput, single-cell assays, and has become a well-established method to interrogate and quantify cells for extensive ranges of biological and clinical applications.[9–11]

On the other hand, biophysical properties (i.e., intrinsic properties), including morphological, mechanical, electrical, and optical properties, rely on properties of cells that do not need extrinsic labels for detection. Biophysical properties are not tied to specific molecular pathways but generally represent the integrative attributes of the underlying cellular features.[12] Analyses of biophysical properties are more suitable for applications that require quick turnaround and for exploratory analysis where biochemical labels for the target cell types or functions are not known.[13,14] A variety of macroscale and microscale label-free characterization techniques have been developed to measure biophysical properties of cells such as cell size, shape, density, refractive index, mechanical, and electrical phenotypes in bulk and at the single-cell resolution.[15–17] Many of them utilize microfluidic technology, which is favorable for precise cell manipulation

and microenvironment control as microfluidics operate at the scale of cells and of unique physical phenomena.[18] Label-free microfluidic methods for single-cell analysis have been applied to many biological and biomedical applications, including cell cycle monitoring, rapid complete blood count, cancer diagnosis, parasite detection, etc.[17]

While a number of promising biophysical properties and their roles in cellular states and functions have been identified, there still lacks a versatile and comprehensive approach that can investigate multiple biophysical markers across domains (e.g., optical, mechanical, electrical) at the single-cell level. Many label-free single-cell characterization tools are generally developed to investigate biophysical markers that are within the principal domains of operations and are rarely extended across domain. My dissertation aims to contribute to this under-explored area by proposing and demonstrating an integrated approach, that reduces the complexity of combining multiple label-free measurement techniques and enables multivariate studies of biophysical markers which are not frequently profiled together.

1.2 Existing Label-Free Cell Characterization Techniques

Numerous label-free cell characterization techniques exist that can probe different aspects of cells with varying operating principles, throughput, and sensitivity. In this section, existing label-free cell characterization techniques are discussed along with their operating principles, applications, throughput, advantages, and limitations. The scope of the review is restricted to the three major domains of cell characterization techniques, including mechanical characterization, electrical characterization, and optical characterization. More emphasis is given to microfluidic single-cell techniques.

1.2.1 Mechanical Characterization of Cells

Mechanical properties of cells generally describe how a cell deforms in response to an applied load.[19] They have been shown to be a promising biomarker as 1) they can represent an integrative characteristic of the underlying components and morphology of cell cytoskeleton, nucleus, and/or plasma membrane; 2) they are directly related to cellular functions, such as migration, adhesion, polarization; and 3) they are hallmarks of numerous diseases, including cancer, cardiovascular disease, inflammation, microbial infections, etc.[13,20–22] A number of characterization techniques that can probe localized and whole-cell mechanical properties with varying deformation extent have been demonstrated. Examples of non-microfluidic approaches include Atomic Force

Microscopy (AFM), micropipette aspiration, microbead rheometry (magnetic tweezer), and optical tweezer. While these techniques can provide precise deformation measurements that can be used to extract elastic and viscoelastic properties of cells, they tend to have low throughput and are challenging to scale up.[12] To meet the high-throughput requirement, microfluidic approaches have been developed to induce cell deformation by various mechanisms, e.g., constriction channels, fluid-dynamic stresses, acoustic waves, optical forces, dielectrophoretic (DEP) forces. We review common microfluidic mechanical characterization techniques, as broadly classified by physical origins of the applied deformation,[2] along with their advantages and limitations in this section.

Structure-induced deformation

In structure-induced deformation approaches, cells are squeezed through constriction channels whose widths are smaller than cell diameter. Deformability indicators, e.g., elongation index, transit time, recovery time, can then be quantified by high-speed imaging, impedance measurement, or cantilever-based mass sensing. The designs of constriction structures that have been reported vary in shapes and arrangements and are often optimized empirically for the samples being tested. Constriction channels have been used to measure biomechanical changes in a variety of cell samples, including different stages of malaria-infected red blood cells,[23,24] leukemia cells from leukostasis-symptomatic patients in comparison to leukostatis-asymptomatic patients,[25] and malignant versus non-malignant cell lines.[26,27] Constriction-based techniques are simple in terms of device design, fabrication, and operation. They mimic structures of *in vivo* capillaries and are easily scalable to many parallel microchannels. The reported throughputs are approximately 1 – 100 cells per second, which is sufficient to process clinically relevant samples. Nevertheless, constriction-based approaches can suffer from limited control of the applied deformation per individual cells and from measurements that can be confounded by size and adhesion between cell surface and constriction surface. Research efforts have been made to mitigate these effects, e.g., by extracting size information in parallel to transit time,[28,29] adjusting the constriction height in real time according to cell diameter of incoming cells,[30] separating entry time and transit time in the analysis,[27] and applying surface treatment prior to experiment to reduce adhesion. In addition, constriction-based techniques are susceptible to clogging as cells are required to come into contact with channel structures. Sample dilution may be required to avoid clogging.

Fluid-induced deformation

In fluid-induced approaches, cells are deformed by shear stress from channel geometry or by extensional flow, and high-speed imaging is used to extract deformation index and size. As these approaches are contact-free (i.e., cells do not have to come into contact with channel surface), channel widths for fluid-induced deformation are generally comparable and slightly larger than the cell diameter. Forsyth et al. observed reduced deformation and increased instances of tumbling (a characteristic dynamic of elongation index vs time of stiff cells) of red blood cells with glutaraldehyde treatment as they travelled through an area with increased shear rate followed by an area with decreased shear rate.[31] Otto et al. has reported a real-time deformability cytometry (RT-DC), in which cells are deformed by shear stresses, with an analysis throughput of > 100 cells per second.[32] RT-DC successfully distinguished changes in deformability and size due to effects of cytoskeletal drugs, cell-cycle progression, and cell differentiation of HL60 cells. Gossett et al. reported an extremely high-throughput (~ 2000 cells per second) approach, in which cells are deformed (> 50% strain) in an extensional flow field, and demonstrated that deformability is a promising biomarker for identifying malignant cells in pleural effusions and pluripotent stem cell differentiation.[33] Overall, fluid-induced approaches for mechanical characterization of single cells are able to achieve high throughput compared to other approaches. Because these approaches are contact-free, they are less susceptible to clogging and are not confounded by adhesion properties of cells. However, they require high-speed cameras which can be costly as well as a rapid image processing pipeline in order to avoid the storage and transfer of large image stacks. Similar to the structure-induced deformation, deformability measured from fluid-induced deformation are dependent on cell size because stress fields generated from these techniques depend on cell size and shape. Therefore, size information is often extracted as an additional parameter.

Optical stretching

Optical stretchers employ two opposed Gaussian laser beams to trap and stretch cells.[34] Radii along the beam axis and radii perpendicular to the beam axis of stretched cells are then extracted from image analysis with resolution down to ±11 nm. The throughput of the optical stretcher is between 1 cell per minute to ~ 20 cells per second.[12] The optical stretcher has been used to distinguish normal, cancerous, and metastatic cell lines; characterize human myeloid precursor cells and three induced lineages; and identify malaria-infected red blood cells.[35–37] While optical

stretching benefits from being a contactless approach, it suffers from low throughput, inherently small deformation due to weak optical force, and sample heating.

DEP-induced deformation

In DEP-induced mechanical characterization (or electrodeformation), cells are trapped and deformed by dielectrophoretic (DEP) force generated from time-varying, nonuniform electric fields. Images of cell deformation are used to extract changes in deformation length or elongation index of cells. Electrodeformation has been applied to characterize deformability of human cancer cell lines, platelets, and healthy red blood cells versus red blood cells infected with *Plasmodium falciparum* malaria parasites.[38–43] Generally, electrodeformation techniques are batch processing systems with limited throughput as the measurement is made for one cell or for a small batch of cells at a time. The processes are not fully automated as manual operation for voltage control during cell trapping and deformation measurement is required. Additionally, special attention must be paid to minimize the influence of Joule heating.

1.2.2 Electrical Characterization of Cells

Dielectric properties of cells have been investigated extensively as an important biophysical marker that can be exploited to manipulate (e.g., focus, trap, or separate) and to characterize cells.[44] They have been applied to characterize blood cells, cancer cells, and stem cells. Electrical characterization results of cells are normally interpreted using the single shell model, which is a simplified electrical model of a cell. In the single shell model, a cell is represented as two uniform concentric layers of different complex permittivity.[45,46] The outer layer represents the cell membrane and the inner sphere represents the cytoplasm. The model can be fitted to the measured complex permittivity in order to extract dielectric parameters, including permittivity and conductivity of each layer. Studies have shown that dielectric properties of the cell membrane are potentially influenced by membrane area, thickness, and composition (e.g. expression of membrane proteins); whereas dielectric properties of the cytoplasm are influenced by intracellular structures and components (e.g., ion concentration).[47–51] We review common approaches for electrical characterization of cells in this section.

Impedance-based approaches

Impedance-based electrical characterization approaches measure the impedance of cells using AC excitation at one or more frequencies. These techniques have evolved from the Coulter counter principle, in which the (DC or low-frequency AC) impedance of a cell flowing through an aperture is measured by sensing electrodes on the two sides.[52] Changes in the measured impedance are used to count cells and extract cell volume. Impedance-based microfluidic cytometry generally integrates microelectrodes within the devices, and measures impedance of cells at frequencies between kHz and MHz ranges.[14] Both simulation and experimental impedance analysis studies have demonstrated that impedance measurements at different frequency ranges can provide useful information about different aspects of the cells, e.g., cell size, membrane properties, and cytoplasmic properties.[53]

Impedance-based microfluidic cytometry can be broadly categorized into two varieties based on whether cells are immobilized or are flowing when the impedances are measured.[54] In the first variation, cells are trapped by hydrodynamic trapping, vacuum aspiration, surface modification, or dielectrophoretic forces; before their electrical impedances are measured.[55–59] Trapping of cells enables measurement of impedance spectra as well as continuous impedance monitoring of the same cells over time for chemical response assessment. Nevertheless, the throughput of these techniques is limited (on the order of ~ 10 cells/study) by many factors, including capture/release time, spectra measurement time, and the number of traps and sensing electrodes that are available on the same chips.[2]

In the second variation, cells continuously flow through the devices while the impedance analysis is performed. Impedance flow cytometry, one example of a successful impedance characterization technique for flowing cells, utilizes differential impedance sensing from two electrode pairs to compare the cell impedance directly against the suspending medium and to cancel any unwanted electrode drifts.[54] The first electrode pair measures the current fluctuation caused by the presence of a cell in the detection volume, while the second pair measures the current passing through pure medium and is used for reference. For differential sensing schemes, parallel electrode pairs have been shown to be a more advantageous configuration than coplanar electrode pairs as they produce more homogenous electric field distribution and less positional variation in the impedance signals.[60] Differential impedance flow cytometry has been demonstrated to

characterize and distinguish polymer beads with different sizes, normal red blood cells and their ghost counterparts or their fixed counterparts, different stages of *Plasmodium falciparum* infected red blood cells, and different states (e.g., normal, apoptotic, necrotic) of tumor cells.[53,61,62] Overall, these characterization techniques were able to achieve high throughput (~ 1000 cells per second). Research efforts have been made to extend the applications of these techniques by improving measurement precision (e.g., via accurate positioning of cells in the detection chamber)[63], and by increasing the number of frequencies that can be measured at the same time (e.g., via maximum length sequence).[64] Another example of impedance characterization for flowing cells uses constriction channels to reduce the positioning variation and decrease the current leakage through the medium surrounding cells.[65] In this technique, single cells are aspirated through the constriction channels where the impedance measurement at one or more frequencies are made from the electrode on each side. Example applications include characterization of tumor cells, red blood cells, and stem cells.[29,65–68] The throughput of the constriction-based technique is on the order of ~ 100 cells per second. Compared to the differential impedance flow cytometry, the constriction-based approach achieves smaller throughput and is more likely to suffer from channel blockage.

DEP-based approaches

When a cell is subjected to a nonuniform electric field; the dielectrophoretic (DEP) force, which is proportional to the cell's effective polarizability (represented by the real component of the Clausius-Mossotti factor or Re[CM]), is exerted on it and can cause it to move or down the electric field gradient.[44] The time-averaged DEP force due to the non-uniform electric field can be approximated as:

$$\bar{F}_{DEP} = 2\pi R^3 \varepsilon_m Re[CM(\omega)] \nabla |\bar{E}_{rms}|^2,$$

where R is the cell's radius, $\varepsilon_m$is the permittivity of the media, ω is the applied radian frequency, and $\nabla|\bar{E}_{rms}|^2$ is the gradient of the square of the electric field magnitude. The frequency-dependent CM factor, $CM(\omega)$, is the effective polarizability of the cell and its surrounding medium:

$$CM(w) = \frac{\varepsilon_p^* - \varepsilon_m^*}{\varepsilon_p^* + 2\varepsilon_m^*}$$

where ε_p^* and ε_p^* are complex permittivity of the cell and the surrounding medium, respectively. If the cell's polarizability is greater than the suspending medium's (Re[CM]>0), the particle is

directed up the field gradient (positive DEP). If the cells' polarizability is smaller than the medium's (Re[CM]<0), the particle is directed down the field gradient (negative DEP). Both the sign and the magnitude of the Re[CM] have been utilized for electrical characterization of cells.

A common DEP-based characterization technique measures the crossover frequency of cells by observing their motion in response to changes in the applied frequency and determines the frequency at which the DEP forces exerting on the cells vanish. This technique has been applied to detect morphology changes in cells undergoing apoptosis, estimate physical properties of neurons and glial cells, and distinguish fate potential of human stem cells.[69–71] DEP crossover frequency experiment requires a very simple experiment setup. However, it can be limited by low throughput associated with batch processing, and the need to use low-conductivity media that may alter the properties of the cells being measured.

Several techniques utilize other types of forces (e.g., hydrodynamic, gravitational, optical) to balance the DEP forces in order to characterize or to manipulate cells. In Dielectrophoretic Field-Flow Fractionation (DEP-FFF), the negative DEP forces levitate cells to different equilibrium heights in a parabolic flow profile, where cells attain different corresponding velocity and eventually time or distance separation based on their dielectric properties.[72,73] DEP-FFF has been applied to separate circulating tumor cells (CTCs) from normal blood cells and separate major leukocyte subpopulations.[74–76] DEP-FFF is a promising technique as it allows high throughput and it does not require the use of low-conductivity media. DEP-FFF technology has been commercialized (e.g., ApoStream®).

Iso-dielectric separation (IDS) is another unique continuous-flow technique to characterize the electrical properties of cells, independently from cell size, at the throughput of ~ 150 cells per second.[77–79] In IDS devices, cells travel in single file along the nDEP barrier (i.e., generated by coplanar or parallel electrodes, which are positioned slightly slanted from the flow direction) from high-conductivity media to low-conductivity media. As the conductivity of their surrounding media decreases, cells experience lower negative DEP force (due to decrease in the magnitude of the Re[CM]). Cells eventually pass through the electrode barrier at the iso-dielectric point (IDP), where the drag force overcomes the negative DEP force, and remain in this position on the conductivity gradient axis. IDS technique has been demonstrated to be a promising, label-free tool to rapidly quantify the number of leukocyte activation, which is more predictive of the clinical

sepsis severity indicator than the complete blood count, in human patients.[80] One downside of the IDS technique is that a conductivity gradient has be generated inside the device for the measurement.

Su et al. has demonstrated a force-balance method called the DEP Spring technique, which allows the Re[CM] of cells to be inferred from the balance position between the hydrodynamic drag force and the DEP force.[81] In this technique, cells, subjected to the drag force, migrate along the channel flow direction. As they move closer to the coplanar electrodes, which are placed slightly slanted from the channel flow direction, they experience larger negative DEP forces, pushing them from the electrode centerline. If the exerted DEP force is sufficient to counteract the drag force, then the cells continue to travel along the electrode centerline at the constant distance perpendicular to the electrode centerline (balance position). This technique has enabled rapid and automated screening of conditions (applied AC frequency and medium conductivity) that can discriminate activated and inactivated neutrophils.[81] As a continuous-flow method, this technique is able to achieve sufficiently high throughput of ~10 cells per second. An extension of this technique, introduced by Jaffe et al., measures the balance positions at three different frequencies of single cells.[82] The authors have determined a set of three frequencies as the optimal combination of frequencies for cell discrimination using Monte Carlo simulation, and have demonstrated that improved classification in cell states was achieved when the measured balance positions at all three frequencies were used.

Electrorotation (ROT)-based approaches

When a cell is subjected to rotating electric fields, an induced torque causes the cell to rotate with a rotation rate (R_{ROT}) that is proportional to the imaginary part of the CM factor (Im[CM]):

$$R_{ROT} = -\frac{\epsilon_m |E_{rms}|^2}{2\eta} Im[CM(\omega)]K,$$

where η is the viscosity of the surrounding medium and K is a scaling factor.[83] The most common ROT setup places a cell at the center of four electrodes which are connected to sinusoidal waveforms with 90^o phase offset. The rotation spectra are measured from the rotation rates of the cell at different applied frequencies (typically between 1 kHz and ~ 1 MHz). Electrorotation has been applied to characterize white blood cells, human cancer cells, … Because the target cell rotates in the same position, the amplitude of the electric field remains unchanged, and is simple

to obtain in order to extract the electrical properties of the cell from the rotation spectra. Electrorotation technique is limited by throughput (estimated to be 12-20 cells per hour) as cell positioning and the spectra measurement can be slow.[84] Recently, Keim et al. reported an improvement in throughput (~ 600 cells per hour) by using single-cell arraying, selective release, and batch measurement.[84]

1.2.3 Optical characterization of Cells

It is well recognized that label-free images and intrinsic optical characteristics (e.g., light scattering, refractive index, absorption, Raman scattering) of cells provide useful information about cell types and states.[85–88] For example, along with fluorescence measurement, flow cytometry is equipped for the measurement of forward-scattered light (FSC), which has some similarity to size, and side-scattered light (SSC), which has some similarity to cell granularity and internal complexity. FSC and SSC parameters are often used to gate viable cells from debris and nonviable cells, prior to fluorescence gating analysis. It has also been demonstrated that FSC and SSC can be used to distinguish major leukocyte subpopulations (i.e., granulocytes, lymphocytes, and monocytes). In addition, with the recent advances in deep learning technologies, applications of label-free imaged-based characterization of single cells have been demonstrated.[89,90]

Microfluidic technology has been integrated with optical detection and image detection in several applications.[88] Particularly, the microfluidic technology is mainly used to continuously introduce single cells through the detection zone, reduce the required sample/reagent volume, minimize manual operation, increase portability, and facilitate high-throughput measurement.[91] Several integrated systems also incorporate microfluidic manipulation techniques, e.g., hydrodynamic focusing, inertial focusing, acoustic focusing, dielectrophoretic focusing, to focus and order cells into single or parallel stream(s) prior to detection. Focusing and ordering of cells improve the precision and efficiency of the overall system by reducing out-of-focus instances as well as mitigating the instances when no cell or more than one cell appear in the detection zone.

Optical flow cytometry

Several label-free optical microfluidic flow cytometers have been developed for low-cost point-of-care applications, by measuring light scattering. Chen et al. developed a microflow cytometer equipped with small-angle forward-scattered light measurements for particle counting and sizing, by using a commercial photovoltaic cell, an adjustable power laser module, and a

PDMS microfluidic chip.[92] They found that the intensity of the forward scattering light linearly correlate with particle size, with a 20% – 30% coefficient of variation (CV). Fu et al. reported an optical microflow cytometer to count and size non-fluorescent and fluorescent particles based on external total reflection.[93] In this system the total number and size of the particles passing through the detection region is extracted from the nonscattered light signal reflected from a plane mirror positioned over the microchip, while the number of fluorescence-labeled particles is extracted from the back scattered fluorescence signal. Su et al. reported a microscope-based microfluidic cytometer, which records 2D patterns of the light scattering. They show that CD34+ hematopoietic stem cells can be distinguished from myeloid precursor cells. Dannhauser et al. reported a microfluidic flow system to measure the light scattering profiles over a wide angular range of red blood cells and match the profiles to simulation to obtain morphological properties of cells.[94]

Imaging flow cytometry

Imaging flow cytometry combines the high-throughput capability of flow cytometry with the high spatial resolution of microscope imaging, and enables studies that are not possible using either technique alone.[95] The commercially available Amnis® ImageStream® imaging flow cytometry can acquire single cell images at rates up to 5,000 cells per second in up to 12 channels, including brightfield, scatter, and fluorescence.[96] The system is equipped with a machine-learning-based image analysis software to circumvent hand-crafted feature selection and enable rapid automated analysis. It has been demonstrated, using the ImageStream® platform and deep-learning based analysis, that the brightfield and darkfield images of single cells can be used to assess stages in the cell cycle as well as identify red blood cell storage lesions in a label-free manner.[95,97,98]

There are two main detection modalities for microfluidic imaging flow cytometry: camera-based and photodetector-based.[91] For camera-based detection modality, a large number of cells in a large detection area are introduced to the detection zone (possibly at reduced velocity compared to the photodetector-based scheme), and are monitored in parallel by a high-speed camera. Hur et al. reported the first example of a high-throughput, microfluidic parallel-flow cytometer by integrating sheathless inertial focusing and high-speed bright-field imaging (between 190,000 and 500,000 fps). The microfluidic platform consists of 256 parallel channels, enabling a sample rate up to 1 million cells per second. The platform is used to automate red blood cell and leukocyte counts on diluted whole blood. Nevertheless, the system is limited in terms of spatial resolution

due to bright-field mode, and is not suitable for morphological analysis.[99] Schonbrun et al. reported a multiple field of view imaging flow cytometry, using parallel microfluidic channels and diffractive lenses to monitor 16 fields of view with a 45X magnification and submicron resolution. They used the system to image latex beads, red blood cells, cancer cell line at the rate of 2,000 – 20,000 instances per second.[100] Rane et al. reported a high-throughput, multi-parametric method that can acquire bright field, dark field, and blur-free fluorescence image, using inertial focusing and stroboscopic epifluorescence imaging. The extrapolated throughput of this technique was ~ 50,000 cells per second.[101] Seo et al. reported a high-throughput on-chip blood analysis, using lens-free digital holographic microscopy to extend the imager's field of view. The system was used to automate counting of red blood cells and 3-part differentiation of white blood cells.[102] This system was able to achieve a spatial resolution of ~ 1.4 μm with the field of view of ~ 24 mm^2. For photodetector-based detection modality, cells are introduced one at a time in a high-speed flow to the detection zone, and the time-stretch imaging method is used to acquire images of fast-moving cells without motion blur. This concept was demonstrated by Goda et al. with the throughput of 100,000 cells per second.[103] Additionally, Asymmetric-detection Time-stretch Optical Microscopy (ATOM) has been demonstrated to improve the time-stretch imaging further by enhancing the image contrast of unlabeled cells.[104]

1.3 Combining Measurements of Multiple Biophysical Markers for Single Cells

There are several benefits to measure multiple biophysical markers for single cells. First, it enables us to study the influences of one marker on the measurement of the other markers, and potentially decouple those effects. For example, various label-free cell characterization techniques are dependent on cell size; therefore, cell size is often extracted out from these experiments as an additional marker. Deformability of cells (which is quantified as elongation index, transit time, Young's modulus) is often reported with cell size in two-dimensional dot plots, which allows us to extract the variations of the deformability marker for the same cell size.[30,32,33,105–108] Similarly, since the electrical impedance at low frequency is associated with cell size, the electrical impedance is often measured at more than one frequency.[61,109] The impedance markers measured from two frequencies are often reported in two-dimensional plots of the impedance at low frequency (related to size) versus the impedance at high frequency or the opacity (the ratio of the impedance at high frequency to the impedance at low frequency). The extraction of cell size as an additional marker illustrates the effects of size on that marker as well as the intrinsic or

measurement variations of the marker.[27] Second, it has been demonstrated, using machine learning techniques, that measuring many multiple biophysical markers significantly improves the classification accuracy of cell types and states. In addition to the elongation index during deformation and the initial diameter before deformation, Lin et al. extracted more than 20 cell motion-related and morphology-related parameters from the deformability cytometry and observed ~ 14% improvement in classification accuracy when comparing pluripotent stem cells and their derivatives.[110] Yang et al. reported 5% – 50% improved classification accuracy of breast cancer cells and their chemically-induced states, by combining the measurements of electrical impedance, deformability, and relaxation index, compared to when the individual markers were used.[111] Increasing classification accuracy can be particularly useful in diagnostic testing and drug screening. Third, it allows multivariate studies of the biophysical profiles of cells that are impossible otherwise, which can potentially be used to discover new subpopulation. This benefit has been shown extensively with flow cytometry and mass cytometry. As biophysical measurement techniques improve in terms of precision, robustness, throughput, and readiness to combine with other techniques, a biophysical phenotyping cytometry, which can measure biophysical profiles of single cells across operating domains (e.g., mechanical, electrical, optical, acoustic, magnetic), can be realized to maximize the benefits of the label-free characterization methods.

1.4 Thesis Overview

The aim of this thesis is to develop and demonstrate a multiparameter intrinsic cytometry approach to combine multiple label-free biophysical measurements for single cells, which is versatile (can combine techniques across domains) and readily extensible (to measure more than two biophysical markers). In Chapter 2, I describe and demonstrate the multiparameter cell-tracking intrinsic cytometry, which utilizes label-free microfluidic techniques to manipulate cells such that information about their biophysical properties can be extracted from their spatiotemporal positions and utilizes cell tracking to extract and associate the biophysical markers for single cells. In Chapter 3, I describe the extension of cell-tracking intrinsic cytometry approach by using digital holographic microscopy and deep learning to monitor cells in a large field of view, enabling rapid and high-throughput assessment of biophysical phenotypes. In the closing chapter, I summarize major contributions of this thesis and offer future outlook.

Chapter 2

Multiparameter cell-tracking intrinsic cytometry for single-cell characterization

Portions of this chapter are adapted from

Apichitsopa, N., Jaffe, A., Voldman, J., **Multiparameter cell-tracking intrinsic cytometry for single-cell characterization**. *Lab on a chip*, 2018.

2.1 Introduction

Cells and their states can be identified by extrinsic markers, biochemical labels that target specific molecules on or in the cells, coupled with detection tags, such as fluorochromes, quantum dots, magnetic beads, and stable isotopes. Flow cytometry and mass cytometry are powerful analysis tools that are readily extensible to investigate 10s of extrinsic markers simultaneously within single cells, making it possible to identify rare subtypes and complex states of cells within heterogeneous populations.[6,7,112] These single-cell multiparametric extrinsic measurements have enabled numerous applications in biology and medicine.[9,113,114]

Cells also possess intrinsic markers, which are the properties of cells that do not need labels to become apparent, such as size, shape, density, optical, mechanical, and electrical properties.[16] Intrinsic markers are useful for measuring cell properties that do not have biochemical markers, and can complement or substitute label-based analysis where cost or time are paramount.[115,116,20,117–119,13,120,2,22] Several label-free macroscale and microscale techniques have been developed for bulk and, within recent decades, single-cell characterization and separation based on intrinsic markers.[2] Microfluidic techniques in particular are appealing due to the plethora of different properties that can be measured and a variety of techniques that have been engineered to perform measurements of these properties.[16,44,121–125] Nevertheless, intrinsic markers are generally not tied to specific molecular pathways, but tend to integrate diverse pathways (e.g. cell size); therefore, intrinsic markers tend to suffer from a lack of specificity. In addition, similar to the case of extrinsic markers, a single intrinsic marker is often not sufficient for cell characterization in real-world applications where different cell states and populations within a complex mixture need to be identified and characterized.

To increase specificity, several studies have measured multiple intrinsic markers simultaneously within single cells. For example, size and deformability measurements of single cells have been shown together to increase specificity in a variety of samples.[26,30,126,33,127,32,105,110] Combinations of cell electrical signatures, e.g. multi-frequency impedance data, have shown similar benefits.[14,54] These multiparametric intrinsic studies show that additional intrinsic markers can be creatively extracted from the same measurement recordings without changing the experiment designs of the dominating measurement techniques, e.g. extracting size or morphology from visual readout or electrical impedance change, and that combinations of intrinsic markers can

improve characterization.[24-33] Here we introduce a more general approach to multiparameter intrinsic cytometry that is readily extensible to different types of intrinsic markers.

There are several ways to develop a multiparameter intrinsic cytometry. One approach is to serially connect the outlet of one device to inlet of the next (Figure 2-1a). To preserve cell identity, cells have to be spaced sufficiently apart to maintain their order through the tubing. Therefore, the throughput of this approach can be limited. Another straightforward and commonly used approach in both extrinsic cytometry and intrinsic cytometry is to combine different measurement techniques into the same integrated space such that different intrinsic properties can be measured simultaneously (Figure 2-1b(left)). An undeniable limitation of this approach is the difficulty of integrating increasing numbers of measurement modalities within the same space and structures. One can also spread the measurement techniques out in the same platform and use time to associate the measured properties to the same cells (Figure 2-1b(right)). However, different probes and readout systems are required, which can add to the complexity as the number of the measurement modules increase. Instead, we propose to spread measurement modules across space and record cell trajectories as they transit between modules. In this fashion, each module can be individually optimized, and the data obtained in each module can be correlated to individual cells using optical cell tracking (Figure 2-1c).

To show a specific implementation of this approach, we developed a cytometry that measures size, polarizability at multiple frequencies, and deformability of single cells. We validate performance of each module and then show how cell tracking can be used to correlate measurements back to individual cells, thus aggregating the data. We use the multiparametric data in the context of cytoskeletal disruption of HL60 cells to investigate the orthogonality between parameters and the importance of each intrinsic marker as a predictor for the classification of cell populations of interest.

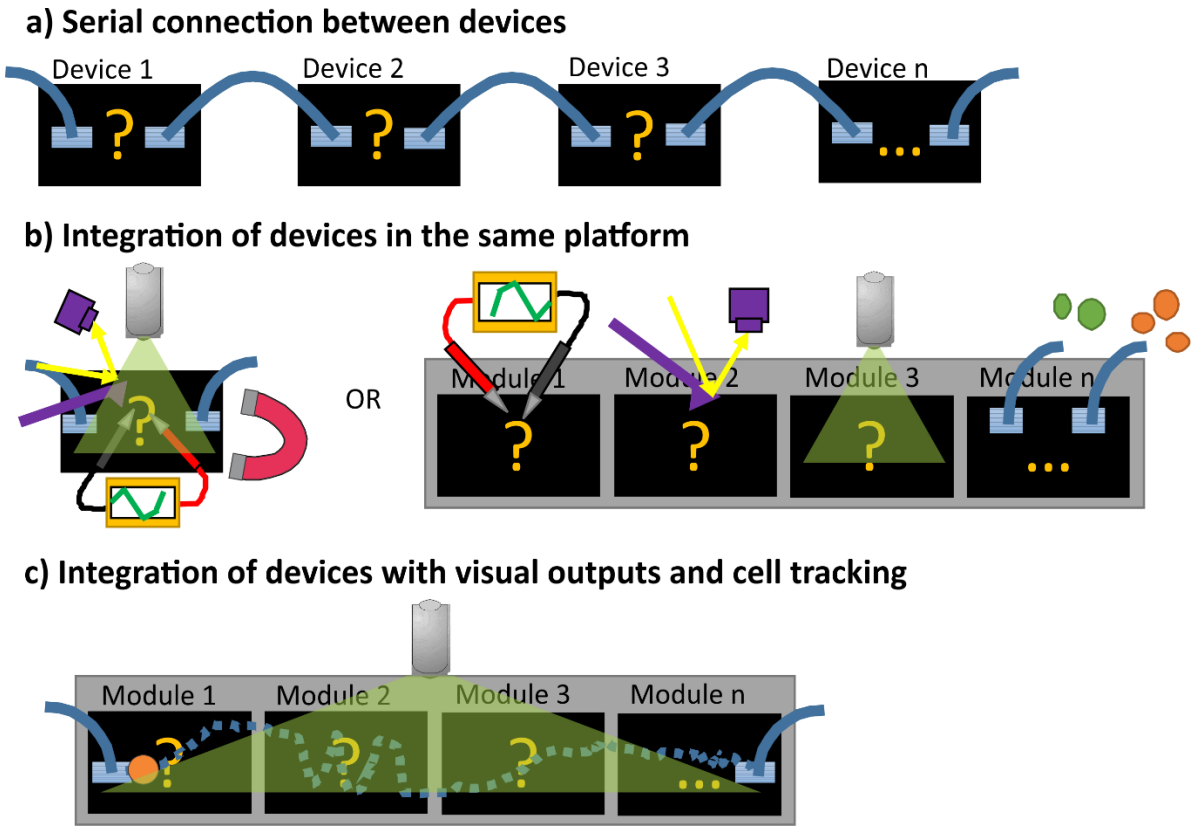

Figure 2-1. Approaches to create a multiparameter intrinsic cytometry. (a) Serial connection via tubing. (b) Integration of devices, within the same platform in the same physical space (left) or spread out in space (right). (c) Integration of devices with visual readout capability and cell tracking.

2.2 n-DEP Spring Overview

The n-DEP spring method utilizes the force balance between the negative DEP force and the hydrodynamic drag force to infer polarizability of cells.[81] In this method, a non-uniform electric filed is created by a pair of coplanar electrodes, which are positioned slightly slanted from the flow direction. As cells flow down the channel and move closer to the centerline of the electrodes, they experience stronger negative DEP forces that counter the drag forces, deflecting them from the electrode centerline. The perpendicular distance from the electrode centerline at which the DEP force acting on the cell is equal to the drag force is termed the balance position (δ), and is used to infer cell polarizability.

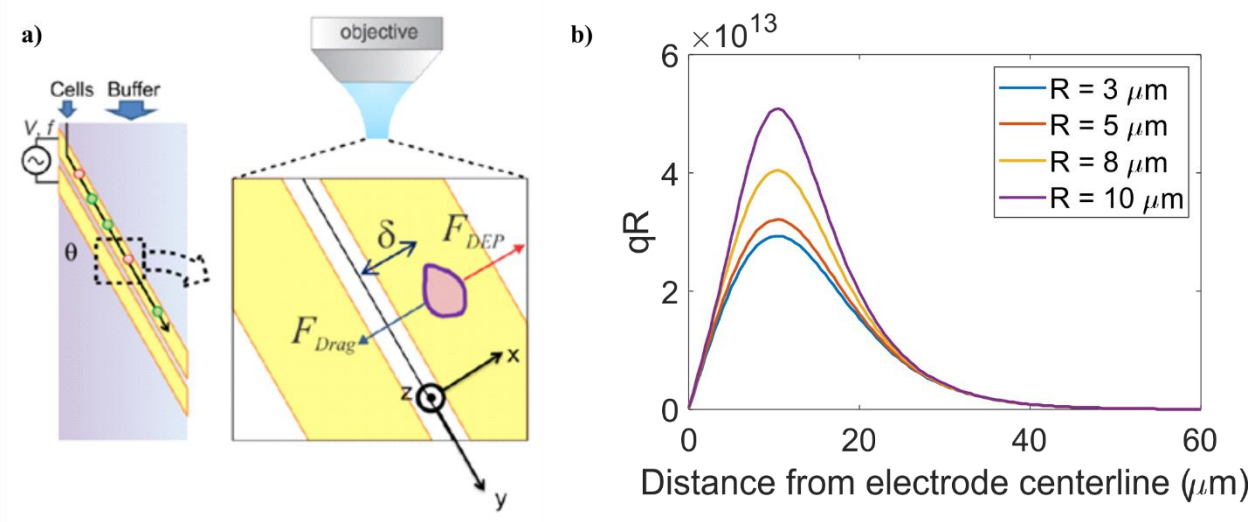

Figure 2-2. a) n-DEP spring overview, reprinted from Su *et al.*[81] b) The positional dependency of the DEP force in x-direction for different particle radii, as calculated by conformal mapping using the device geometry specified in this study.

The hydrodynamic drag force (F_{Drag}) acting on a cell in a uniform Stokes' flow (Reynolds number << 1) in the *x*-direction is given as

$$F_{Dragx} = -6\pi R\eta v_x$$

where R is the cell radius, η is the viscosity of the media, and v_x is the average velocity of the flow at the center of the cell in the *x*-direction. The average velocity in the *x*-direction of the flow at the center of the cell can be estimated from the parabolic flow profile along the *z*-axis, assuming that the cell is pushed toward the ceiling by the upward DEP force, as

$$v_x = \frac{6Q}{wh^3} R(h-R)\sin\theta$$

where Q is the volumetric flow rate, w is the channel width, h is the channel height, and θ is the angle between the electrode centerline and the flow direction.

The negative DEP force acting on a cell is given as

$$F_{DEPx} = 2\pi R^3 \varepsilon_m Re[CM] \frac{\partial E^2(x, h-R)}{\partial x}$$
$$= 2\pi R^3 \varepsilon_m Re[CM] q_R(x) V_{RMS}^2 p(f, \sigma_m)$$

where ε_m is the permittivity of the media, $Re[CM]$ is the real component of the Clausius-Mossotti (CM) factor (a measure of the cell's effective polarizability), $E^2(x, h-R)$ is the RMS value of

the electric field strength for an applied RMS voltage V_{RMS} at location x and height h - R, q_R is a function that reflects positional dependency of the DEP force, and $p(f, \sigma_m)$ is a function that corrects for frequency-dependent voltage drop at the electrode/solution interface.

At the balance position (δ),

$$\bar{F}_{DEPx} + \bar{F}_{Dragx} = 2\pi R^3 \varepsilon_m Re[CM] q_R(\delta) V_{RMS}^2 p(f, \sigma_m) - 6\pi R\eta \left[\frac{6Q}{wh^3} R(h-R)\sin\theta\right] = 0$$

The balance position is, therefore, defined as

$$\delta = q_R^{-1}\left(\frac{3\eta \sin\theta \left[\frac{6Q}{wh^3}(h-R)\right]}{R\varepsilon_m Re[CM] V_{RMS}^2 p(f, \sigma_m)}\right) = q_R^{-1}\left(\frac{18\eta \sin\theta}{wh^3 \varepsilon_m p(f, \sigma_m)} \cdot \frac{Q}{V_{RMS}^2} \cdot \frac{(h-R)}{R \cdot Re[CM]}\right)$$

For a device with fixed electrode geometry and fixed channel geometry, Q and V_{RMS} can be tuned to increase drag force or DEP force, respectively. Given that the balance positions and the radii of cells can be measured, *Re*[*CM*] can also be extracted. For cells with the same radii, an increase in the balance positions indicates an increase in the *Re*[*CM*].

2.3 Materials and Methods

2.3.1 Cell Culture

BA/F3 murine interleukin-3 dependent pro-B cell line was cultured according to ATCC protocols and were passaged ~3-4 days at 1/10 dilution. The cell culture medium was prepared from RPMI-1640 with high glucose content, L-Glutamine, and phenol red indicator, supplemented with 10% fetal bovine serum, 1% L-glutamine, 1% penicillin-streptomycin, 1% Sodium Pyruvate, and 1% MEM non-essential amino acids.

HL60 human acute promyelocytic leukemia cell line was cultured according to ATCC protocols and were passaged ~2-3 days to maintain cell density between $1x10^5$ and $1x10^6$ cells/mL. The cell culture medium was prepared from RPMI-1640 with high glucose content, L-Glutamine, and phenol red indicator, supplemented with 10% fetal bovine serum, and 1% penicillin-streptomycin.

2.3.2 Microfluidic device

For deformability experiment, the device consists of a PDMS layer which contains a 15-μm-high microfluidic channel with 32 parallel constriction channels, modified from Rosenbluth *et al*.[25]

The widths of the narrowest constrictions are 10 µm for BA/F3 experiments and are 6 µm for HL60 experiments. The two constriction widths were chosen experimentally as the constriction channels had to be sufficiently narrow to be sensitive to the change in cell deformability and sufficiently wide to avoid channel clogging which decreased the number of available channels for testing. The microfluidic channels in PDMS is molded from an SU-8 silicon master or a plastic master mold replicated from the original mold, using standard microfabrication techniques. The PDMS layer is then bonded a glass slide after 2-minute exposure to oxygen plasma.

For polarizability and size experiment, the device is as described in Su *et al.*[81] The device consists of two main components: 1) a PDMS layer with 20µm-by-2mm-by-5cm channel, which is molded from silicon or plastic master mold, and 2) a patterned electrode layer with 200nm Au and 10 nm Ti on Pyrex wafer, which is fabricated using standard lift-off protocol. The two components are plasma bonded and sealed with two-part epoxy.

For multiparameter intrinsic cytometry experiment, the integrated platform design is shown in Figure 2-3. The PDMS layer and the electrode layer of the cytometry are fabricated as previously described. The channel pattern in the PDMS layer is then aligned and plasma-bonded to the electrode patterns on Pyrex wafer. External electrical connections are soldered onto the predesignated electrode pads.

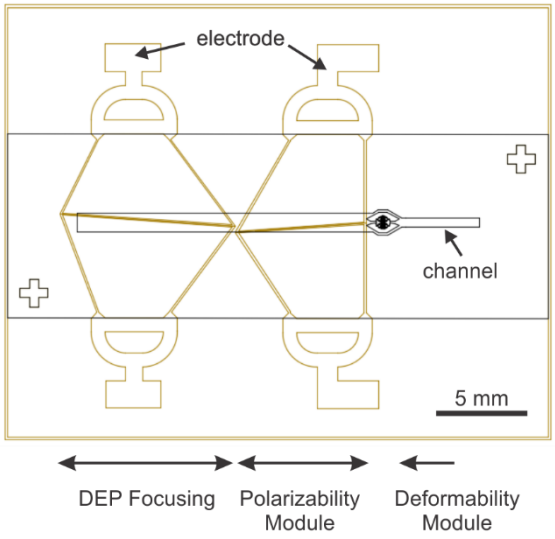

Figure 2-3. Device design. The device contains one inlet, DEP focusing, polarizability module, deformability module, and one outlet. The device footprint is ~29.27 mm (L) × 23.28 mm (W). The polarizability module

footprint, including the channel, electrodes, and the electrode contact pads, is ~7.07 mm (L) × 19.75 mm (W). The deformability module footprint is ~1.92 mm (L) × 1.35 mm (W).

2.3.3 Cell assay

For deformability study, BA/F3 cells were incubated with 4% paraformaldehyde in Dulbecco's Phosphate-Buffered Saline (DPBS) at room temperature for 10 minutes. For drug treatment studies, HL60 cells were exposed to 10% DMSO (for control), 2μM or 10 μM Cytochalasin D in addition to 1μM Calcein AM, and incubated at 37°C for 1 hour. Calcein AM was added to cells to improve cell detection accuracy. Before each experiment, prepared cells are re-suspended in DPBS with 13%(w/v) Dextran at 1 $x10^5$-$2x10^5$ cells/mL.

2.3.4 Cytometry experiment

Microfluidic channels are flushed with 0.5% (w/v) Pluronic-F108 in DI water until all bubbles are removed, and are passivated with 2% bovine serum albumin in DPBS for 1-2 hours to reduce non-specific binding between cell samples and channel walls. Typical experiment setup is shown in Figure 2-4. Cell samples are loaded into 1 mL Hamilton Syringe, which is connected to the device via 0.01 ID PEEK™ tubing and sample-loop configuration. The device is connected to function generators via 50Ω coaxial cable with BNC connectors. Constant flow is delivered by Chemyx Fusion 200 syringe pump. Due to difference in channel structures and cell diameters, flow rate is 1 μL/min for BA/F3 experiments and 0.3 μL/min for HL60 experiment. Customized MATLAB GUI (Figure 2-5), modified from Su *et al.*,[81] is used to control Agilent 33220A function generator (for frequency < 20 MHz), Aim TTi TGR1040 RF signal generator (for frequency ≥ 20 MHz) and PCO Sensicam QE camera. Imaging is performed with Zeiss Axio Imager m1m upright microscope. Once initiated, MATLAB GUI records time-lapsed videos along with the frame-by-frame frequency sequence generated by the function generator. The video recording settings including FOV, frame rate, and recording time, were optimized in terms of cell measurement throughput under the constraint of RAM capacity. Therefore, the recording conditions were different for the deformability module validation, polarizability module validation, and the integrated platform experiments. The field of view (FOV) for the deformability module validation, polarizability module validation, and the integrated platform experiments were ~206 μm × 757 μm (H x V), 1373 μm × ~103 μm (H x V), and ~2065 μm × 757 μm (H x V), respectively. The recording frame rates for the deformability module validation, polarizability module validation,

and integrated platform experiments were ~20 frames per seconds, ~32 frames per seconds, and ~5.3 frames per seconds, respectively.

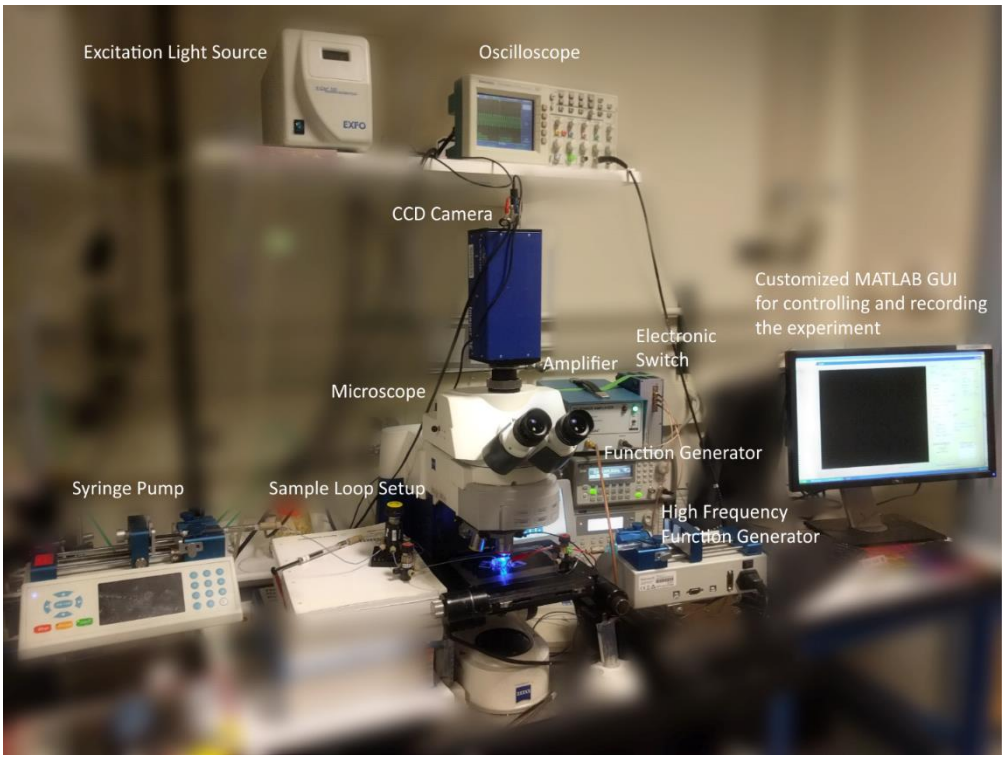

Figure 2-4. Cytometry experiment setup.

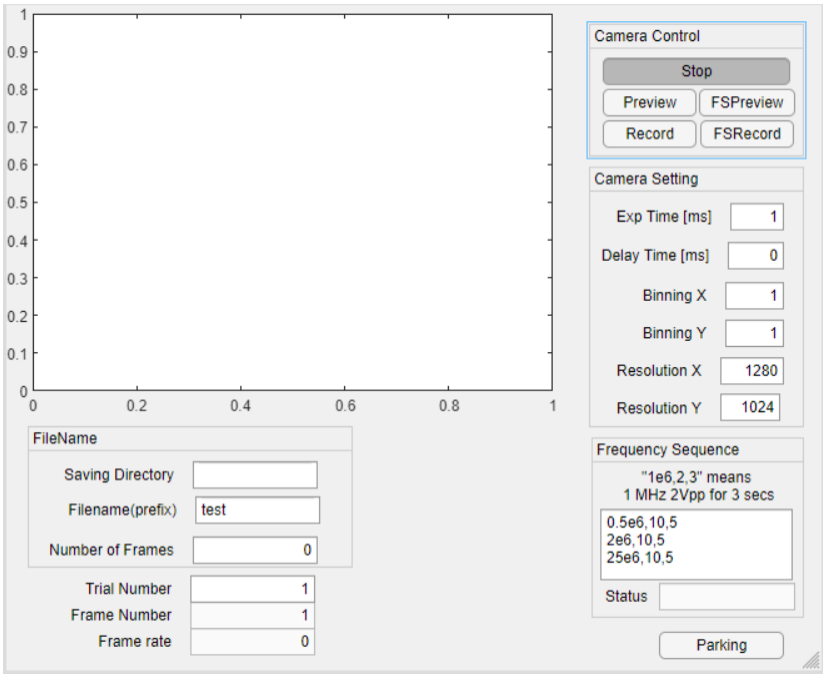

Figure 2-5. Customized MATLAB graphic user interface (GUI) for the cytometry experiment.

2.3.5 Cell detection and tracking

All image processing and analysis are performed in MATLAB®R2017a. For cell detection, intensity image in each frame of the time-lapsed videos is binarized via adaptive thresholding and connected components within specified area constraints are considered potential cell detections. The extracted cells centroid locations in each frame are then applied to the customized multi-object tracking algorithm.

For tracking, cell detections which correspond to the same cell across time are assigned to the same track by the Hungarian algorithm. The cost matrix supplied to the Hungarian algorithm can be depicted by,

$$cost(i,j) = distance\ between\ detection\ 'i'\ from\ previous\ frames \\ and\ detection\ 'j'\ from\ the\ current\ frame\ \times direction\ parameter \\ \times channel\ geometry\ parameter,$$

where i and j are indices for each detection of the previous frames and for each detection of the current frame, respectively. The distance between detections is used as one of the parameter in the cost matrix under the assumption that detections between frames of the same cells are closer together than detections between frames of different cells. Therefore, assignment of cells to tracks

can be achieved by minimizing the distance or the cost matrix. Direction parameter and channel geometry parameter are included in the cost matrix to prevent assignment of any cell motions which are not possible, given a priori knowledge about the flow direction in the channel and the channel geometry. The distance cost will be replaced with an infinite cost if any impossible motion between detections are detected and the assignment between those detections will not be made as the Hungarian algorithm will try to minimize the cost function. For each frame of the time-lapsed video, the cost matrix is computed and the track assignments made by the Hungarian algorithm are updated. Any unassigned detections in the current frame will be assigned to new tracks and any tracks from the previous frames that are unassigned will be marked invisible and penalized. After a track has been penalized for more than predetermined number of frames, the cell corresponding to that track is considered to have left the field-of-view.

2.3.6 Data extraction

After tracking, locations of individual cells with respect to channel structure across time are specified. In addition to equivalent diameters, transit times, and balance positions at three frequencies of individual cells are extracted. Equivalent diameter is calculated from $2 \times \sqrt{area/\pi}$. Transit time is calculated from number of frames a cell stays in the deformability ROI divided by number of frames per seconds. Balance position at each frequency is calculated from the perpendicular distance from the electrode centerline to the cell centroid detected within the polarizability ROI when waveform of that specific frequency is applied. If there are more than one measurement of a specific parameter for a cell, the measurements are averaged to give the final extracted values.

2.3.7 Data analysis

The Wilcoxon rank sum tests (equivalently the Mann-Whitney U-test) were performed to compare transit time distributions with determination of statistical significance between populations.

Two-dimensional visualization of the multiparameter single-cell data was produced by visual interactive stochastic neighbor embedding (viSNE),[128] a nonlinear dimensionality reduction technique that maps data points from high-dimensional space to low-dimensional space while conserving the spatial relationship between nearest neighbors. The resulting two-dimensional projections, i.e. viSNE maps, allow visualization of the high-dimensional data, making it easier to

analyze and interpret. To study relationship between the measured intrinsic markers and cell population, data points in viSNE maps representing single-cell data can be re-colored according to the cell population or according to measurement of each marker.

To evaluate the orthogonality between the measured intrinsic markers and the importance of each marker, we plot Pearson's linear correlation coefficients between all pairs of intrinsic markers and trained supervised machine learning algorithms, including random forest and SVM, to classify cell populations with 70% of the dataset and withhold the rest for testing. We trained with all 31 possible combinations of five markers used for classification ranging from one marker to five markers used. To elaborate, there are five cases each where number of markers used is one and four, and there are 10 cases each where number of markers used is two and three, and there are only 1 case where all five markers are used. In all cases, optimal training parameters were determined with Bayesian optimization, which searches for hyperparameters that minimize five-fold cross validation loss. We computed the average of the classification accuracy on the test set in different conditions and grouped them in terms of number of markers used. Impact of each marker on the model accuracy is evaluated by permuting values of that marker and observing decrease in model accuracy.

2.4 Results and Discussion

2.4.1 Cytometer architecture and choice of modality

Cell-tracking cytometry comprises of three main subsystems: a microfluidic platform, microscope imaging, and image processing (Figure 2-6). The microfluidic platform consists of measurement modules for the intrinsic markers of interest. These modules are designed such that they encode the intrinsic markers of interest into the relative temporal and spatial positions of cells. Microscope imaging enables observation and recording of cell spatiotemporal positions in the microfluidic platform in the form of information-rich image stacks. The image processing subsystem then detects, tracks, and extracts the intrinsic markers of cells from the image stacks as well as associates intrinsic marker measurements from different modules corresponding to the same cells across the platform. This tracking-based intrinsic cytometry approach, which spreads the measurement modules out in space on the same microfluidic platform and links them via tracking, minimizes constraints on area and volume of microfluidic investigation chamber and on the measurement techniques (e.g. synchronization of readout signals or probing requirements).

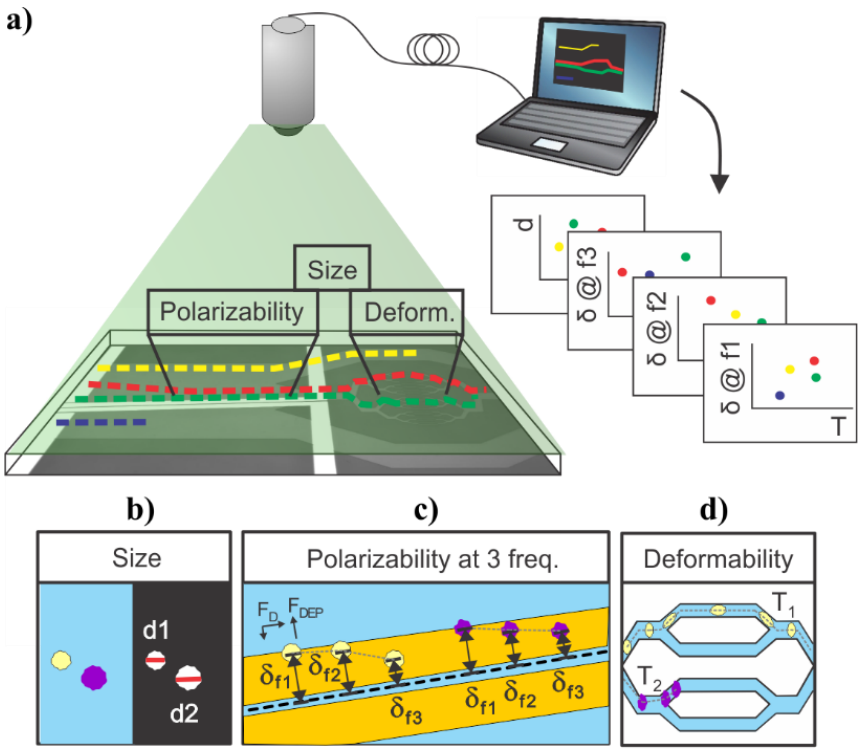

Figure 2-6. Multiparameter intrinsic cytometry. (a) Overview. Combining different microfluidic modules on one substrate along with cell tracking to correlate per-cell information across modules allows acquisition of multiparameter intrinsic properties. (b-d) Specific instantiation with five parameters. (b) Size module. Cell size (d1, d2) is obtained optically from images as cells flow through modules. (c) Multi-frequency nDEP spring module. Cells driven by hydrodynamic flow forces (FD) experience an opposing nDEP forces (FDEP) as they approach coplanar electrodes and reach different equilibrium positions (δf1, δf2, δf3) based on their polarizability at the applied frequency. By applying a sequence of three different frequencies, we obtain 3 measures of polarizability. (d) Deformability module. Cells deform as they transit through narrow channels. The transit time (T1, T2) is related to their deformability.

While different intrinsic markers can reflect different aspects of cells, we chose to study size, deformability, and polarizability of single cells on our platform. We chose size because cell size is determined by both intrinsic developmental programs and extracellular signals.[129] Cell size has been used as a marker to coarsely separate cell types and cell states, e.g. blood cell fractionation, platelet activation, separation of neuroblastoma cells and glioma cells.[130–132] Cell deformability signifies cytoskeletal or nuclear changes associated with disease progression and changes in cell states, and has been used to characterize changes of malaria-infected red blood cells, invasive cancer cells compared to benign cells of the same origin, activated and inactivated leukocytes, and pluripotency of stem cells.[13,22] Finally, cell polarizability consolidates information about cell morphology and composition, and has been shown to distinguish subtle changes in biological

phenotypes, e.g. induced apoptosis in HL60 cells, stimulation of T and B lymphocytes, and induced differentiation in Friend murine erythroleukemia cell lines.[133] Overall, size, deformability, and polarizability of cells are promising label-free biomarkers that have been extensively investigated individually, but rarely studied all together.

Each intrinsic marker can be measured by a variety of techniques. Cell deformability measurement techniques include optical stretching, cell transit analyzers, hydrodynamic forces, and others.[2] Electrical properties of single cells can be measured by impedance cytometry, dielectrophoretic force balance techniques, and electro-rotation techniques.[54,133] Size can be measured with image processing, Coulter resistive sizing, deterministic lateral displacement array, etc.[30,52,134] Here we chose techniques that translate the properties into spatiotemporal positions and are thus compatible with the cell-tracking cytometry approach.

2.4.2 Deformability module design and analysis

We adopted a constriction-based deformability measurement platform previously introduced by the Fletcher group.[25] In the platform, suspended cells are squeezed through parallel constriction channels whose width is smaller than the cell diameter (Figure 2-7a). More deformable cells are expected to transit through the constriction faster than less deformable cells (holding cell size and cell-surface interactions constant).

On our platform, cells were detected from image stacks by thresholding the pixel intensity within the region of interest (ROI), followed by cell segmentation and tracking (Figure 2-7(b-c)). The transit time of each cell was calculated as the difference between the time stamp when the cell first entered the ROI and the time stamp when the cell exited the ROI. Multiple cells could be detected at the same time with a customized tracking algorithm (Figure 2-7d).

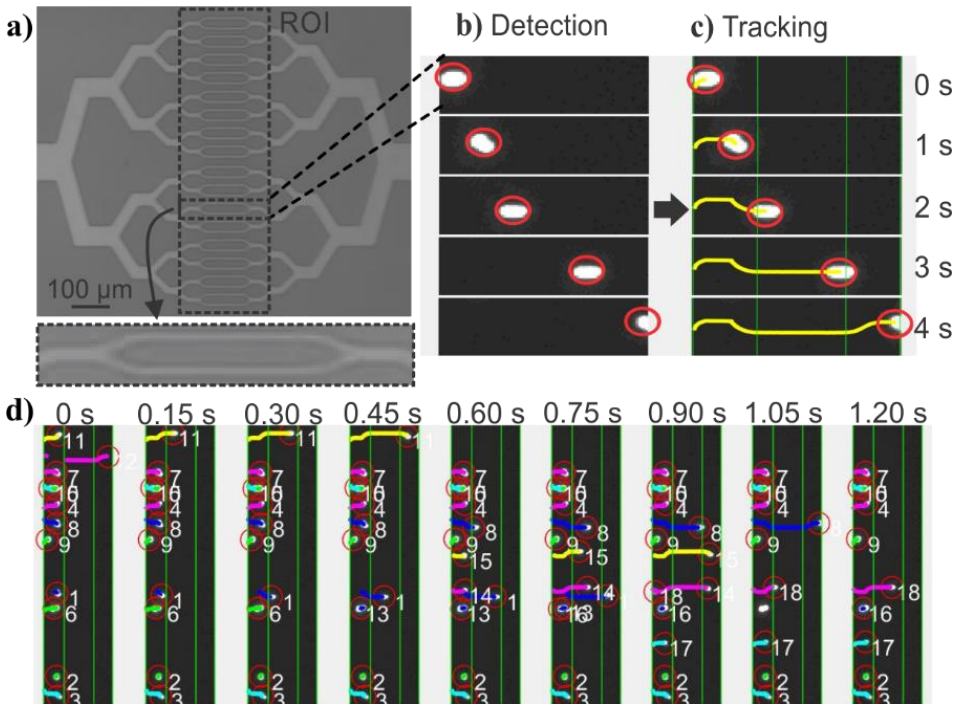

Figure 2-7. Deformability measurement module and image analysis. (a) Image of 32 parallel constriction channels and region of interest (ROI). The inset shows exploded view of two narrowest constriction channels. (b) Cell detection. Images of cells in videos are detected by adaptive thresholding and filtered by size. (c) Cell tracking. Detected cells in subsequent frames are assigned to tracks based on nearest-neighbor adjacency and direction of travel. Transit time is defined as the time for a cell to travel across the ROI. (d) Multiple object tracking. This approach allows many cell trajectories to be determined simultaneously. Shown are frames with identified cells denoted by numbers.

2.4.3 Deformability module validation

To validate the transit time measurements from the constriction-based deformability module, we performed two sets of experiments. First, we studied BA/F3 cells, a murine interleukin-3 dependent pro-B cell line, with and without 10-minute exposure to 4% paraformaldehyde crosslinking fixative, which has been previously used to provide additional rigidity to the cells. Cells that are fixed by cross-linking agents such as formaldehyde[33] or glutaraldehyde[24,107,135–138] are expected to have decreased deformability (negative change). Figure 2-8(a-b) shows beeswarm plots and histograms of the extracted transit time for control and fixed BA/F3 cells. Qualitatively, in fixed cells we observed an increase in the cell population that has > 3 seconds of transit time. Direct comparison of quartiles shows a ~2.5-fold (1.05 s vs. 0.41 s) increase in the 75th percentile population in the fixed cells (Figure 2-8c), supporting an increased transit time upon fixation.

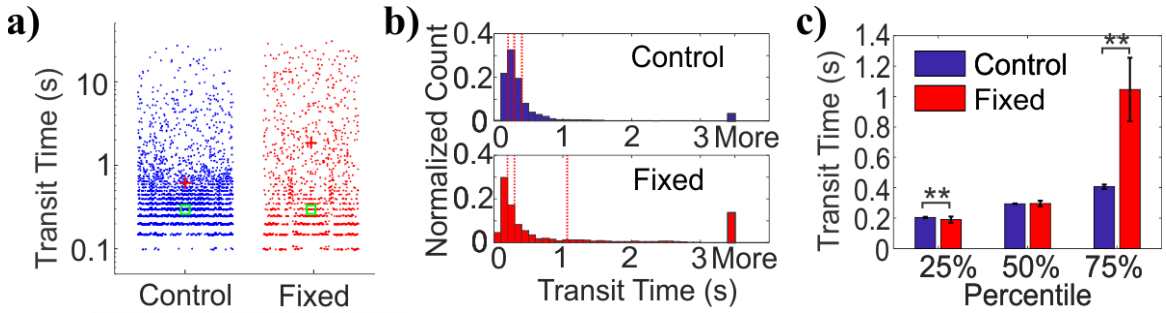

Figure 2-8. Transit time measurement of control and fixed BA/F3 populations. (a) Measured transit times from control (n=5270) and fixed (n=1418) BA/F3s. Red crosses and green squares depict mean and median of the distributions, respectively. (b) Histograms of cell transit time across 3 experiments over one device replicate. Red dashed lines depict 25%, 50%, and 75% percentile of the distribution, respectively. (c) Extracted quantiles of transit times (**, $p<0.01$). Error bars represent 95% confidence intervals.

To generalize beyond one cell type and one condition, we undertook experiments using HL-60 cells, a human promyelocytic leukemia cell line, with and without exposure to Cytochalasin D. Cytochalasin D is a potent actin polymerization inhibitor, which has been shown to increase cell deformability (positive change) by various deformability measurement techniques.[25,32,139] Figure 2-9(a-b) show beeswarm plots and histograms of control and 2μM Cytochalasin D treated cells. The transit time distributions of the two populations are not normally distributed, but rather are heavy-tailed. Qualitatively, the shape of the Cytochalasin D treated transit time distribution is slightly more skewed toward lower transit times. In this case we find a significant decrease in the 75th percentile transit time (3.43 s vs. 5.12 s), consistent with an increase in deformability (Figure 2-9c).

Together, these results demonstrate proper functioning of the deformability module coupled with image-based cell tracking.

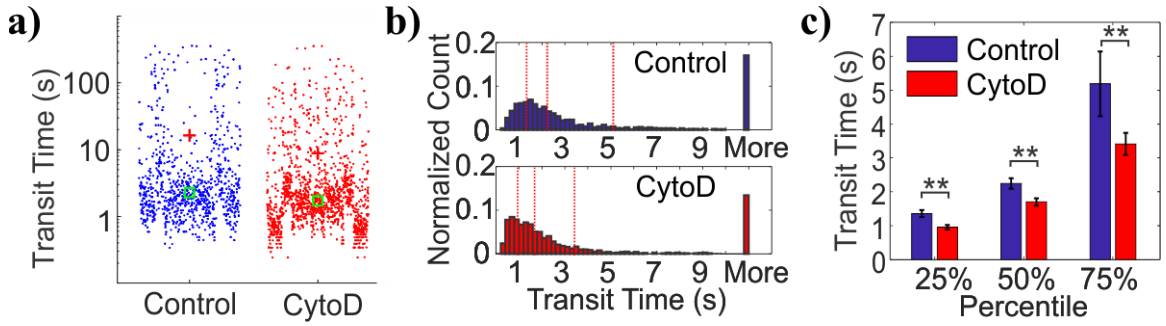

Figure 2-9. Transit time measurement of control and 2-μM Cytochalasin D treated HL60 cells. (a) Measured transit times from control (n=867) and Cytochalasin D-treated (n=1371) HL60s. Red crosses and green squares depict mean and median of the distributions, respectively. (b) Histograms of cell transit time across

6 experiments over three device replicates. Red dashed lines depict 25%, 50%, and 75% percentile of the distribution, respectively. (c) Extracted quantiles of transit times, or the 25, 50, and 75 percentiles of the transit time distribution (**, $p<0.01$). Error bars represent 95% confidence intervals.

2.4.4 Size and polarizability module design and analysis

For polarizability measurement, we use a variant of the DEP spring previously introduced by our lab.[81] In this technique, a pair of parallel coplanar electrodes is positioned slightly slanted from the flow direction (Figure 2-10a). Cells that are introduced into the channel are subjected to a hydrodynamic drag force and will migrate along the channel flow direction. Once cells encounter the electrodes, cells will be subjected to a negative DEP force that pushes the cells away from the electrode centerline. If the negative DEP force in the direction perpendicular to the electrode centerline is sufficient to counter balance the drag force, cells will continue to migrate along the direction of the electrode centerline. With this technique, the polarizability of cells can be inferred from a measurement of the balance position (δ) that arises as a competition between the fluid drag force and the negative DEP force. Cell polarizability can be reported as the real part of the Clausius-Mossotti factor (Re[CM]), which incorporates the geometry and electrical properties of cell compartments. The different compartments and their properties cause the Re[CM] to be frequency dependent. For example, subtle changes in the cytosolic compartment will be more prominent in the balance position measurements at a higher frequency range than changes in the cell membrane. Thus, probing cell polarizability at multiple frequencies provides richer electrical phenotypic information. The frequency sequence, which is a repeated set of three frequencies, was randomly chosen within the operative frequency range that will be most indicative of the Re[CM] spectra. We applied this frequency sequence to the electrodes for testing.

Similar to the deformability module, we use the image stacks to detect and track cells as they traverse the DEP spring (Figure 2-10b). We extract the distance of the cell centroids from electrode centerline, and can obtain balance position measurements at multiple frequencies by correlating the cell position in time to the temporal frequency sequence (Figure 2-10c). The imaging can also be used to extract cell diameter of each cell, using the frame stack to obtain multiple measures of the diameter as the cell traverses the field of view.

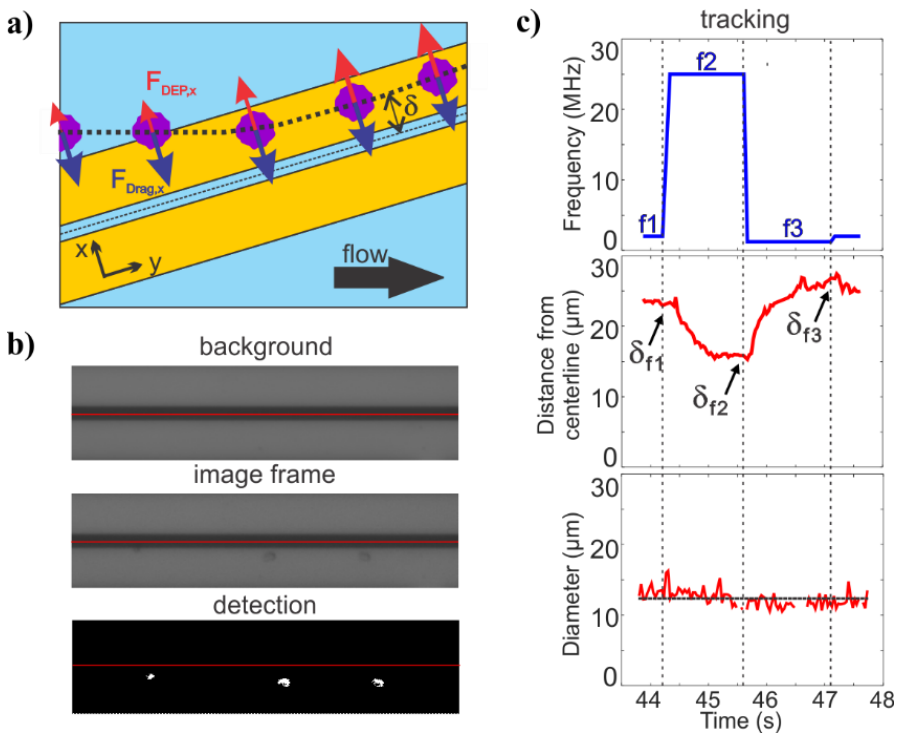

Figure 2-10. Size and multi-frequency nDEP measurements through image processing. (a) Overview of DEP spring method. Balance positions (δ) are the equilibrium perpendicular distance between the cell centroid and the center of the electrodes. Three different frequencies are applied as the cells traverse the field of view, allowing determination of three balance positions, which are related to the polarizability. (b) Images of cells on electrodes are thresholded after background subtraction. Red horizontal lines indicate the electrode centerline. (c) Extracted cell diameters and distance of the cell centroid from the electrode centerline relative to the applied frequency as a cell traversed the polarizability module. As there are many diameter measurements for each cell, the mean of the cell diameters measured across time is considered to be the extracted cell diameter.

2.4.5 Size module validation

To validate the extracted cell diameters, we compared visually measured cell diameters to those measured using Coulter sizing for all three HL60 populations. Histograms of cell diameters extracted from image processing on our platform and cell diameters measured from coulter counter measurements for all three HL60 populations are shown in Figure 2-11. The average and standard deviation of cell diameters measured from Coulter counter for control, 2μM and 10μM Cytochalasin D populations were 11.28±1.41 μm, 11.04±1.39 μm, 10.97±1.34 μm, respectively, whereas they were 10.55±1.21 μm, 9.81±1.31 μm, 9.45±1.38 μm, respectively, when measured via image processing. Thus, for each HL60 population, the average cell diameters obtained from image processing are <1.6 μm (17%) smaller than those measured via Coulter counter, which is not surprising given that image thresholding can lead to such systematic biases. While size

accuracy can be achieved by calibrating the threshold value for a particular illumination, focusing, object material and background setting, such calibration can be burdensome as the imaging setting can fluctuate slightly during experiment and more so across experiments. For size measurement on our platform, accuracy is not as crucial as precision since we are only interested in relative size within and between cell populations.

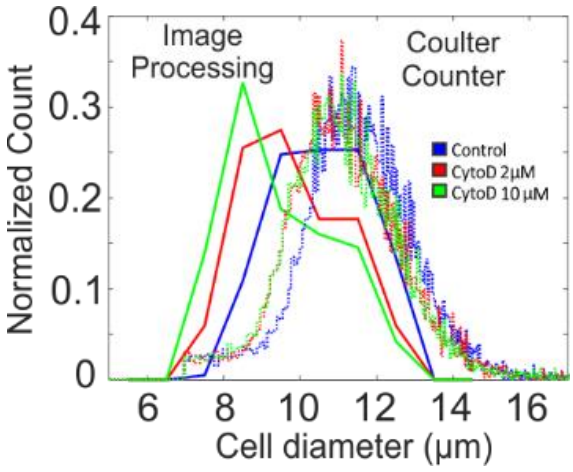

Figure 2-11. Histogram of cell diameters as extracted from the image processing and from coulter counter measurements.

2.4.6 Polarizability module validation

To validate the operation of the multi-frequency DEP spring module with cell tracking, we used HL60s exposed to Cytochalasin D, which has been shown to impact cell actin structure in a dose-dependent manner.[140] Here we measured balance positions at three different frequencies of single cells in a single device. According to the CCD camera pixel size and the selected objective lens, the measured balance positions were determined with ±1.07 μm resolution. Extracted balance positions at three different frequencies of single cells are shown in scatter plots with marginal histograms in Figure 2-12. For each population, the balance positions generally decreased as the test frequency increased. For each test frequency, we observed positive shift in balance positions as the concentration of Cytochalasin D increased even though cell diameters decreased, which implied an increase in Re[CM] magnitude. The imperfect linear relationships between all pairs of the three frequencies in the scatter plots suggest that additional information is obtained with each added frequency.

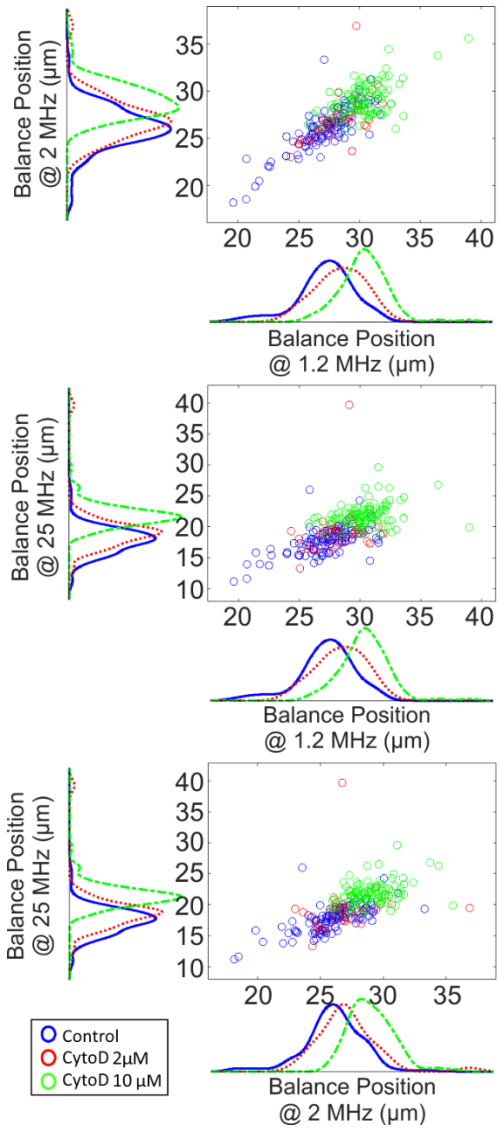

Figure 2-12. Scatter plots with marginal histograms of balance points at three different frequencies for control (n=194), 2μM (n=51), and 10μM (n=144) CytochalasinD treated HL60s.

2.4.7 Multiparameter intrinsic characterization of single cells

To show how cell tracking and can be used to correlate multiple properties across different microfluidic elements, we created an intrinsic cytometer with size, deformability, and polarizability modules (Figure 2-13a). This device incorporated both electrode-based analysis (DEP spring) and PDMS microfluidics (deformability), two common microfluidic fabrication modalities. Broadly speaking, with our approach, the multiplicative nature of the yield of data within each module can cause substantial data loss as number of modules to be integrated increase. Therefore, it is important to ensure that the throughput of the modality corresponding to each

marker in the pipeline is maximized and that the tracking algorithm is optimized to maintain the relations between markers of single cells. Particularly, on our first instantiation of this approach, we were able to extract all five markers of only 12% of cells that were detected on the platform (not shown). With further investigation and improvement on both the DEP spring module and the deformability module, we were able to increase the throughput from ~100 cells per run (~12% of all cell detections) to ~400 cells per run (~48% of all cell detections). The remaining ~50% of cell detections did not have measurements of all 5 markers, partially because 1) we exclude transit time measurements of cells that came into contact with another, 2) some cells were not focused onto the investigation region of the DEP spring module and did not experience the negative DEP force which was required for the polarizability measurements, 3) some cells travelled faster than others through the DEP spring module and did not have enough time to experience all three frequencies in the frequency sequence. The yield can be further improved by enhancing the efficiency of cell focusing prior to DEP spring module measurements, optimizing the frequency sequence, flow rate, and ROI of the DEP spring module.

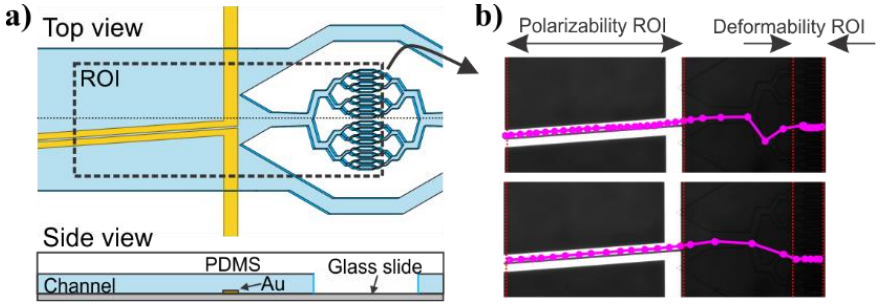

Figure 2-13. Multiparameter intrinsic measurements. (a) top view and side view of integrated platform schematic, drawn not to scale. (b) successful tracks of cells across the polarizability module and the deformability module.

We then performed assays examining the effect of Cytochalasin D on the five intrinsic markers that we measured. Unlike the separate studies for deformability and polarizability modules in previous sections, here we can measure all five intrinsic markers and maintain the connections between these markers for single cells. Examples of tracks of cells as they traverse the different modules are shown in Figure 2-13b. The extracted multiparameter data of single cells are shown in 5-by-5 scatter plots in Figure 2-14.

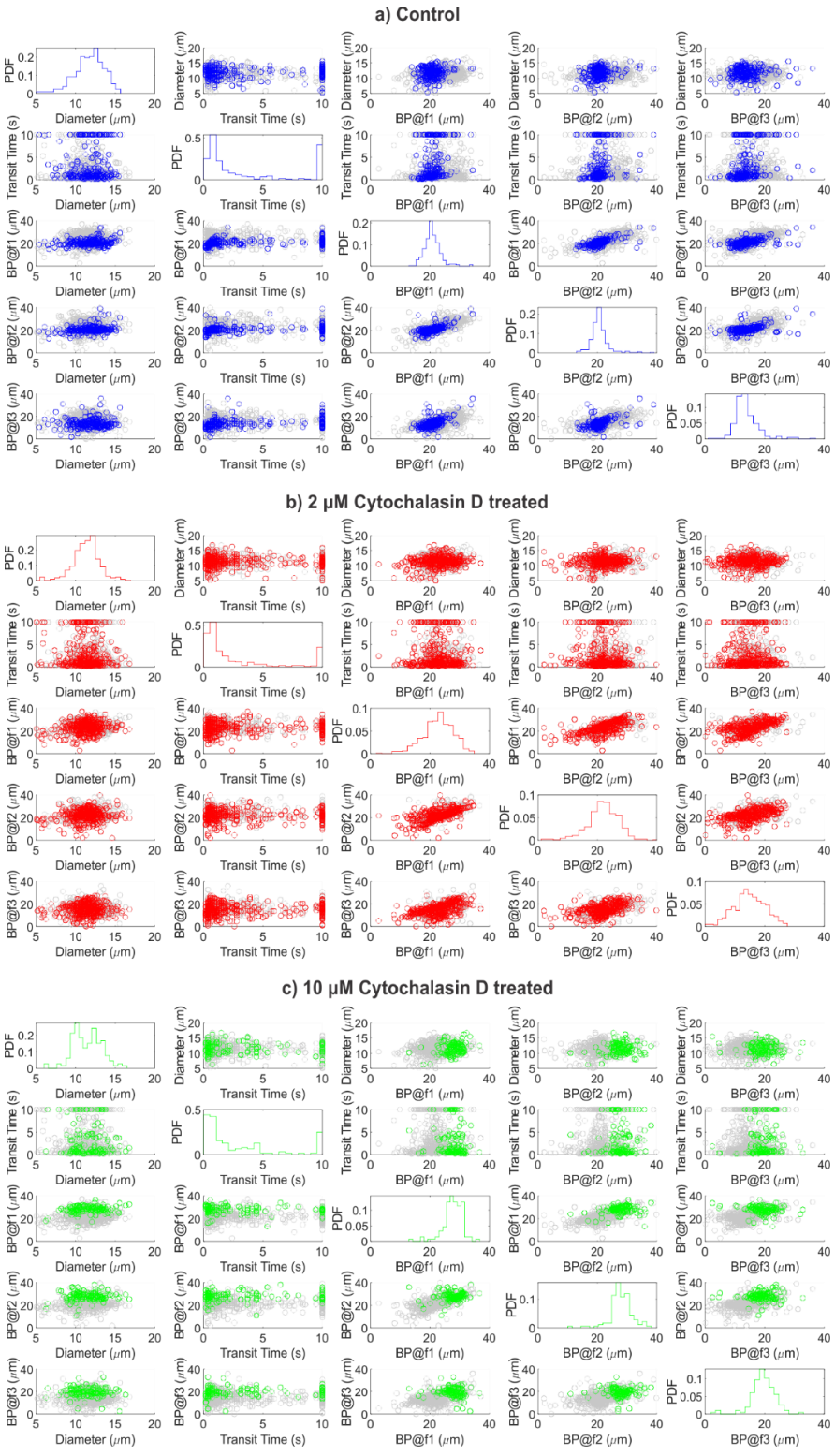

Figure 2-14. Scatter plots and histograms of the five intrinsic markers measured by the integrated platform for (a) control population (blue), (b) 2 µM Cytochalasin D treated population (red), and (c) 10 µM Cytochalasin D treated population (green)

viSNE is used to project the single-cell multiparameter data from the 5D space into 2D plots while preserving significant structures in the high-dimensional space. viSNE visualization of the multiparameter data as colored by population (exposure to Cytochalasin D) is shown in Figure 2-15a. The viSNE map reveals clear separation between the control population and the 10-µM Cytochalasin D-treated population, while there is a high degree of overlap between most of the space occupied by the two populations and 2- µM Cytochalasin D-treated population. To better understand the relations between the separation in viSNE visualization and the intrinsic marker measurements, the same viSNE map is re-labelled according to each of the five intrinsic marker measurements and shown in Figure 2-15b. In general, cells with larger size are distributed across the three natural clusters in the map while transit time gradually increases toward the tip of the cape-shaped region in the lower right quadrant of the map. Nevertheless, the trends in size and transit time did not seem to significantly contribute to the visual separation of cell populations in viSNE map. In contrast, the balance positions at three frequencies, which represent the polarizability marker, gradually increase toward the top right of the viSNE maps. Mentally overlaying the viSNE map with the population-based color scheme onto the viSNE map with the marker-based color scheme shows that the 10-µM Cytochalasin D-treated population tends to have larger balance positions at all three tested frequencies than control populations. Meanwhile, the 2-µM Cytochalasin D-treated population is not clearly separable from the other two populations with the five markers that we measured on our platform.

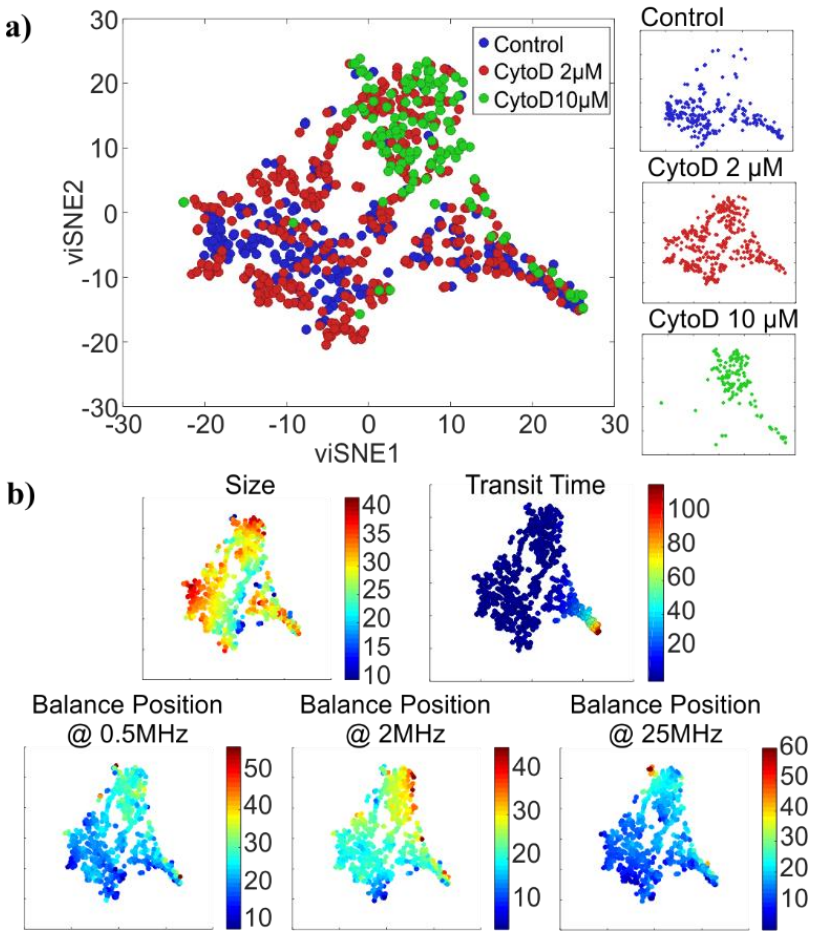

Figure 2-15. Visualization of multiparameter data by applying a nonlinear dimensionality-reduction technique, viSNE. (a) viSNE maps of the multiparameter data for control (n=240), 2 uM (n=393), and 10 uM (n=137) Cytochalasin D treated HL60s. The two axes represent arbitrary units. (b) corresponding viSNE maps as colored by individual parameter measurements, namely size, transit time, and balance positions at 0.5 MHz, 2 MHz, and 25 MHz.

To quantitatively investigate the orthogonality between each intrinsic marker measured from our multiparameter platform, we computed Pearson's correlation coefficients between all pairs of markers (Figure 2-16). If two markers are highly correlated (i.e. less orthogonal), we might not need to measure both of them. Orthogonality between markers indicates how much additional information we are able to learn from measuring them and helps determine the optimal set of markers needed for cell classification. We observed stronger correlation ($R>0.36$) in pairs of balance positions at two different frequencies than other pairs of markers ($R<0.10$). With correlation coefficients (R) between -0.01 and 0.05, variation in cell size does not seem to have contributed to variation in transit time and balance positions. Similarly, transit time is not strongly correlated to balance position at each of the three frequencies ($0.03<R<0.07$). In general, none of

the intrinsic marker pairs are strongly correlated to each other and we expect to gain additional information about the cells from each of the measured intrinsic markers.

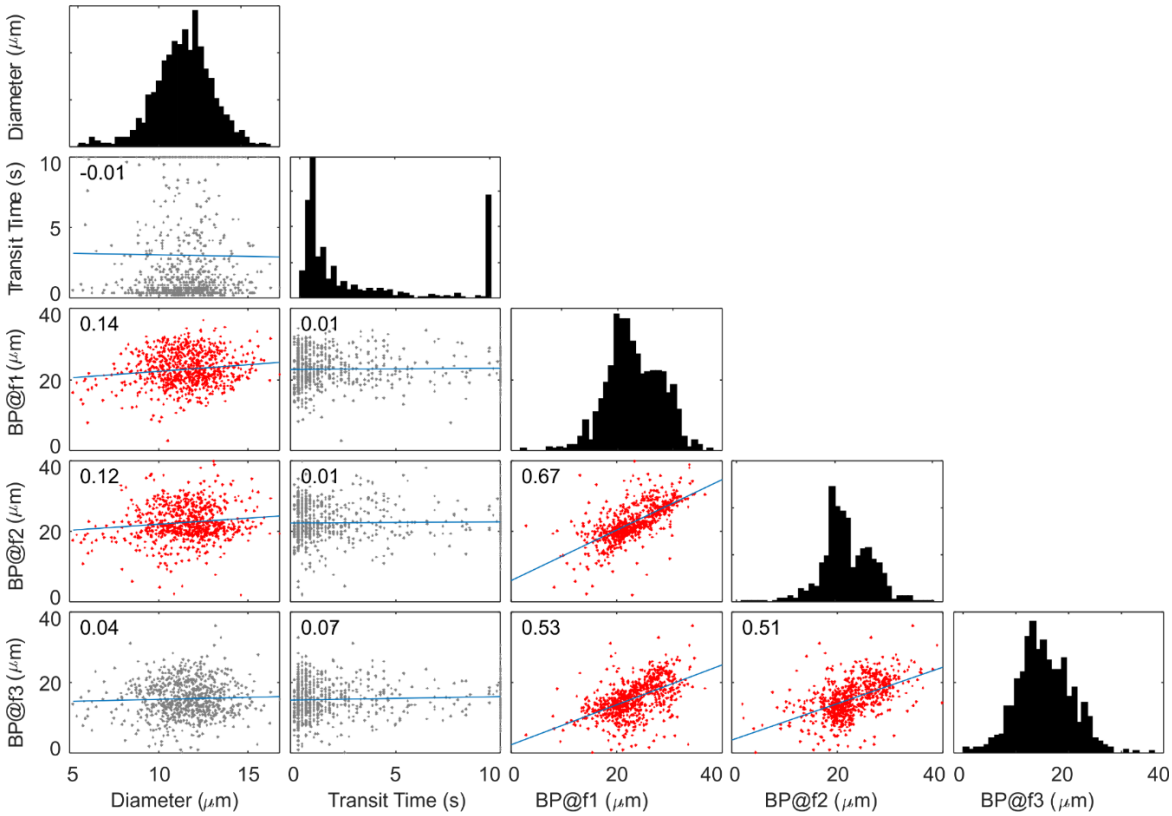

Figure 2-16. Matrix of plots showing correlation among pairs of the measured intrinsic markers for the multiparameter single-cell data across all three populations, including, control, 2 uM, and 10 uM Cytochalasin D treated HL60s. The correlation coefficients as well as the slopes of the corresponding least-square reference lines are displayed in the plots. Red dots indicate that the correlation coefficient is significantly different from zero ($p<0.05$). Histograms of markers are shown along the matrix diagonal.

To evaluate how the number of intrinsic markers measured for single cells affects the ability to distinguish between the treatment conditions, we trained random forest classifiers for all subsets of the 5 markers measured and computed averaged classification accuracies on the test set when only one intrinsic marker was used for classification compared to when 2, 3, 4, and all 5 markers were used for classification. The random forest algorithm was chosen because it is a non-parametric approach, which is intrinsically suited for multiclass classification. In other words, it does not make any assumptions about the shape of the decision boundaries between classes and therefore it is well suited for our classification problem where the decision boundaries between populations are expected to be highly non-linear. We find that the classification accuracy generally

increases as the number of intrinsic markers used increases (Figure 2-17a), suggesting that all five intrinsic markers measured contribute to the characterization of the cell states of interest, particularly the exposure level of Cytochalasin D drug. Nevertheless, even with all five markers, the average classification accuracy on the test set is ~71.4%. The confusion matrix from the representative run of the random forest algorithm (Figure 2-17c) shows that most classification errors originate from the reduced ability to distinguish the 2 μM Cytochalasin D treated population from the control population and the 10 μM Cytochalasin D treated population. This is consistent with observations from viSNE maps, which show partially overlapping regions between 2 μM Cytochalasin D treated population and the other two populations. Furthermore, the importance of each marker on the accuracy of the model can be evaluated by permuting the values of the marker of interest and observing the changes in classification accuracy. Permutation of an unimportant marker should have little effect on model accuracy while permutation of an important marker should significantly decrease it. According to Figure 2-17b, permutation of balance positions at all three frequencies decrease the model accuracy by ~6.9-10.4%, which were more than those of size (~4.8%) and transit time (~3.0%), suggesting that the balance position markers contribute to classification accuracy more than the other two markers. Similar results were obtained by the same analysis with another machine-learning algorithm, the support vector machine (SVM) with a Gaussian kernel (Figure 2-18). The only difference between the random forest model and the SVM model is the impact of size on the model accuracy.

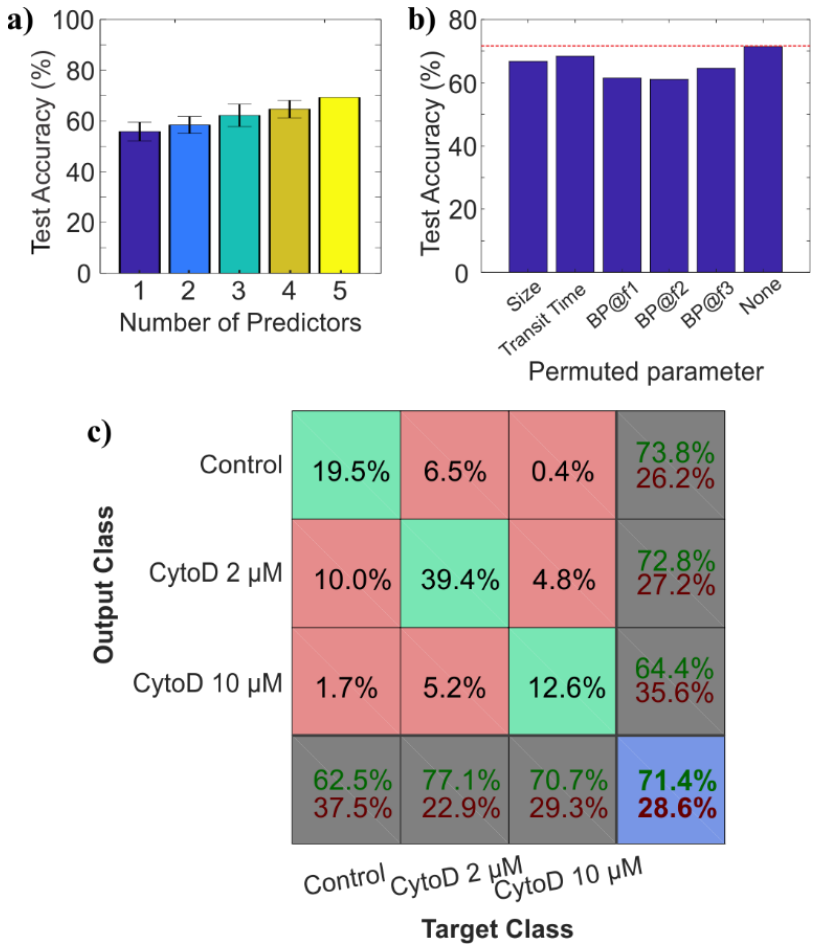

Figure 2-17. Classification of cell states from the multiparameter single-cell data containing three cell populations by random forest models. (a) Classification accuracy by the random forest classifiers on the test data set as the number of predictors used increases. (b) Impact of each intrinsic marker on the classification accuracy of the random forest model, which used all five measured markers. Larger decrease in classification accuracy is expected as the values of a more important marker are permuted. (c) Confusion matrix describing the performance of the random forest classifier with all five intrinsic markers on the test data set. Green and red boxes represent the percentages of accurate and inaccurate classifier outputs corresponding to target classes, respectively. The blue box shows the overall classification accuracy of the model.

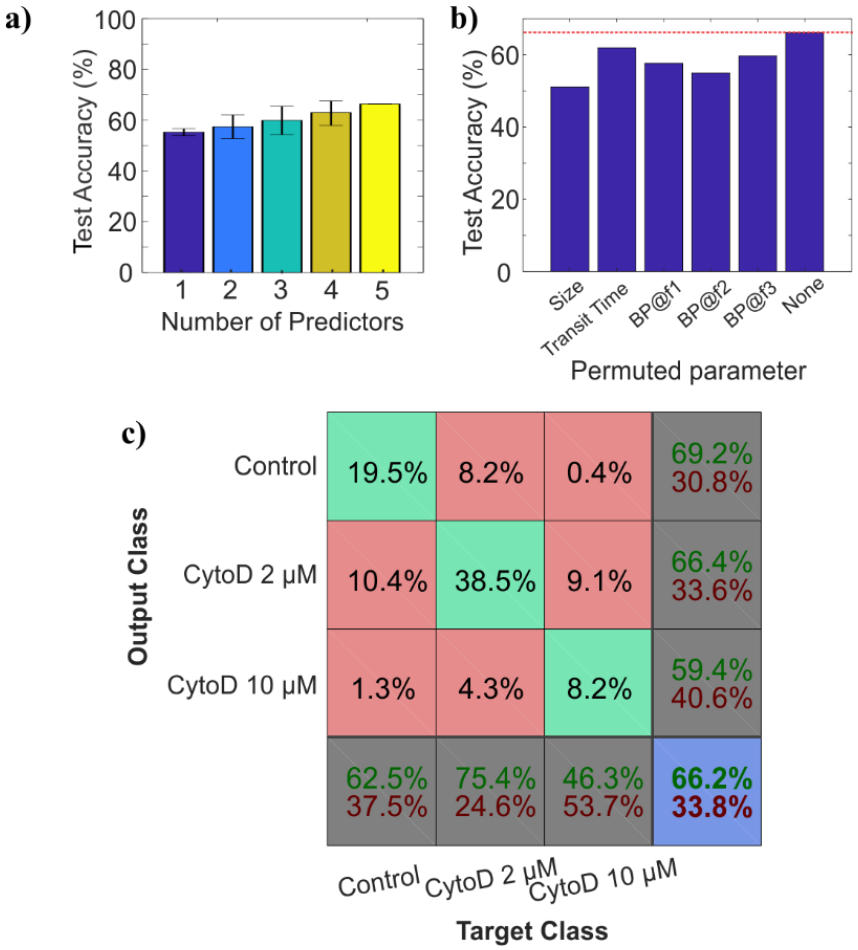

Figure 2-18. Classification of cell states from the multiparameter single-cell data containing three cell populations by support vector machine (SVM) models. (a) Classification accuracy by the SVM classifiers on the test data set as the number of predictors used increases. (b) Impact of each parameter on the classification accuracy of the SVM model. Classification accuracy as the values of each parameter are permuted. (c) confusion matrix describing the performance of the SVM model with all 5 intrinsic markers on the test data set.

Simultaneous electrical and mechanical characterizations of single cells have been demonstrated on various platforms and have been shown to improve classification accuracy when the two types of markers were combined compared to when they were individually tested.[29,65,141–144] Most of these platforms utilized electrical impedance measurements to measure cell impedance profiles as well as cell transit times through constriction.[29,65,144] While electrical-detection- based techniques are favorable for real-time applications due to simplicity in data extraction and processing, we opted for image-based techniques due to multiple reasons. First, more subtle features of cell properties can be harnessed from images without additional probes, e.g. surface roughness, aspect ratio, constriction entry time, elongation length, etc. Second, image-based

techniques allow cell measurements to be parallelized within and across measurement modules, which compensates for tracking and data extraction time. Similarly for extrinsic markers, there have been efforts to change the analytical paradigm of conventional flow cytometry in order to improve cell throughput by acoustically focus cells in a parallelized fashion and use image-based detection to extract optical parameter data in order to remove the limitations from serially investigating one cell in a single focused stream at a time.[145,146] Last but not least, image-based techniques provide ease of potential integration of additional modules. Measurement techniques that translate their property directly into electrical signals are scarce, while the set of techniques that can be read out from images is large. By restraining ourselves to measurement techniques that enable visual readouts, the integration complexity with regard to output synchronization and processing is significantly reduced. In particular, our platform utilized a force-balanced technique called the DEP spring to characterize electrical properties of cells, which allows electrical properties of cells to be embedded in their spatiotemporal positions and eliminates the need for extra probes for electrical detection as well as the requirement for an impedance analysis system.

Our platform, which measures five intrinsic markers for single cells, is only a proof-of-concept demonstration. Additional markers which might be useful for cell characterization can be retrieved from the image stacks recorded with the current setup, e.g. constriction entry time, elongation length of deformed cells, and aspect ratio of undeformed cells. Elongation index, and separation of entry and transit behaviors have been shown to improve classification of benign and cancer cells based on deformability marker as well as have been used to estimate Young's modulus, hydrodynamic resistance, and cytoplasmic viscosity of cells.[26,147] While indirect markers are sufficient for cell classification purposes, extraction of fundamental intrinsic properties such as Young's modulus, viscosity, and polarizability should be considered in the device design and analysis for comparing the same properties across different measurement techniques and for robustness in the interpretability of the results. Furthermore, for applications where cell size is not known a priori or varies broadly, one can integrate the constriction-based module with varying constriction widths right after size separation module with corresponding lateral displacement of cell size, e.g., deterministic lateral displacement array, in order to maintain the ratio of cell size to constriction width, or choose to substitute the constriction-based module with other deformability measurement techniques which are less susceptible to cell size. Regardless, the main advantage of tracking-based intrinsic cytometry is versatility in the design and optimization of the microfluidic

platform. The collection of intrinsic markers studied can be further expanded and optimized by adding or substituting the measurement modules on the platform, as currently we used only 24% of the entire field-of-view of the microscope with 5X objective. One can imagine extending the device footprint further by using 2.5X objective with trade-off on the image resolution and accuracy of the distance- or size- related measurements. With numerous label-free microfluidic techniques for measuring cell intrinsic properties, especially those equipped with visual readout capabilities, e.g., deterministic lateral displacement array, inertial microfluidics, acoustophoresis, optical techniques,[16] there are many combinations of the microfluidic measurement modules that can be integrated with this approach to allow several intrinsic markers of single cells to be studied simultaneously. We envision our proposed approach as a general strategy to develop multiparameter intrinsic cytometry tools.

2.5 Conclusions

We proposed a new multiparameter intrinsic cytometry approach for characterizing single cells, by combining measurement of ≥2 intrinsic markers on the same platform and associating markers to single cells via tracking. In contrast to conventional approaches that integrate different measurement techniques in the same physical space and measure properties of single cells simultaneously, our approach distributes measurement across space and measures properties of cells in parallel fashion. This adaptation allows each measurement module to be optimized individually and makes the platform readily extensible to more measurement techniques as constraints on investigation space are mitigated. We demonstrated a proof-of-concept implementation that can measure five intrinsic markers of single cells, including size, deformability, and polarizability at three frequencies. By studying cell samples with drug-induced changes in cytoskeleton, individual modules were first validated separately and the fully integrated platform was demonstrated. Analyses of Pearson's linear correlation coefficients and supervised classification accuracy results both confirmed that additional information about the drug-induced structural changes of cells could be obtained with each additional intrinsic marker that we measured. Similar to the development of extrinsic markers and their countless biomedical applications, we anticipate intrinsic markers to become more useful in complex real-world applications once combinations of intrinsic markers can be investigated with ease.

Chapter 3

Real-time, large-area, cell-tracking intrinsic cytometry with digital holography and deep learning

Portions of this chapter are adapted from

Apichitsopa, N., Voldman, J., **Real-time, large-area, cell-tracking intrinsic cytometry with digital holography and deep learning**. (submitted manuscript, 2020)

3.1 Introduction

The cell-tracking intrinsic cytometry using microscope imaging reported in Chapter 2 has many benefits. First, there is a vast pool of image-based microfluidic methods which can be combined with this approach. Second, because the measurement modules are spread out in space, each module can be independently optimized. Third, parallelization within and across modules is straightforward as cells' positions in time and two-dimensional space can be linked via multiparameter object tracking. Regardless, as cell tracking has to be maintained across measurement modules, one limitation of this approach is the need to keep the entire interrogation area of the platform within the microscope FOV. The restricted microscope FOV limits the active area of the microfluidic platform, which in turns limits throughput and specificity of the overall analysis. In addition, as cell-tracking cytometry is an image-based approach, rapid image processing is required to achieved quick turnaround time. In this chapter, we explore solutions to mitigate these two challenges.

More generally, observation and analysis of particle motion in fluids is indispensable in microfluidics.[148] Dynamics of particles (e.g., , cells, organisms) inside microfluidic channels are routinely studied for various applications, including characterization of fluid dynamics underlying a carefully designed microenvironment and investigation of cell behaviors in vitro, sometimes in response to controlled stimulation and manipulation.[149–152] Several detection methodologies have been developed to detect and measure particle dynamics in microfluidic devices, including photodetector-based imaging, camera-based imaging, impedance sensing, etc.[17,91,149,153,154] The most prevalent of these is camera-based imaging via conventional benchtop microscopes due to the rich spatial information that images provide, and their availability, ease of use, and versatility across a wide range of imaging applications.[155–157]

Despite many benefits, there are a few challenges for investigation of particle motion in microfluidic platforms using the camera-based imaging technique via benchtop microscopes. First, the ability to detect moving microscale particles sensitively with a benchtop microscope imaging system, especially in bright-field images, imposes a lower limit on the imager's spatial resolution, which then dictates the upper limit for the microscope's field of view (FOV) and the probe area of the microfluidic platform. This limitation renders a mismatch between the field of view of microscope objective (< a few mm^2 scale) and the active area of microfluidic chips, which can be

more than an order of magnitude larger. In effect, the fundamental trade-off between spatial resolution and field of view in most microscope objectives limits the sensitivity and scalability of the image readout. While mechanical scanning and tiling approaches may be used to tackle resolution-FOV trade-off for static samples and samples with slow movement, they are not feasible in continuous-flow platforms where rapid dynamics of moving particles need to be captured and where particle identity across the platform needs to be maintained.

Second, as with any other image-based detection techniques, a fast and accurate image processing pipeline is required to achieve high analytical throughput and to avoid storing a large number of image stacks for post-experiment processing.[158] Extracting relevant data from information-rich image stacks generally incorporates two main steps, namely object detection, which locates objects' bounding boxes in each still frame, and object tracking, which associates the detected bounding boxes across frames for the same objects. Detection of objects flowing through obstacles in bright-field microscope images can be computationally complex as a result of low signal-to-noise ratio, high and fluctuating background noise, and inconsistency in shape and intensity of the object images. Object tracking can suffer when multiple objects travel through the platform at varying speed and when there are false positives and missed detections.[159] To reflect the fluidic throughput and maximize the final throughput, both object detection and object tracking need to be optimized in accuracy and processing time.

Here, we implement two technologies to extend the capability of the image-based detection system for single-cell intrinsic cytometry. First, large-FOV digital holography,[160] a well-developed lens-free computational imaging technique, is used to overcome the microscope's FOV limitation and image cells inside a large-scale microfluidic cytometry platform that contains two pairs of coplanar electrodes for multi-frequency polarizability measurement[81,82] and 72 parallel constriction channels for deformability measurement.[25] While large-FOV digital holography has been applied to observe dynamic of biological samples, e.g., blood cells and sperms, both in straight microchannels and in large microchambers,[102,161,162] it has rarely been applied to observe cells in more complicated microstructures, e.g., constriction channels, micropillars, and coplanar electrode layers, which are essential for probing biophysical properties of cells and for manipulation of cells. Second, a deep learning You Only Look Once (YOLO) object detection algorithm[163–165] is used to detect cells' spatiotemporal positions in hologram images without digital

reconstruction even in the presence of cell deformation and physical microstructures that create interference in the optical path of the cell holograms. Together with a customized tracking algorithm, multiple cells are detected and tracked as they traverse the microfluidic platform in a real-time manner. The integration of deep learning in an image processing pipeline enables rapid and automated detection of defocused and deformable cell hologram patterns, avoiding the process of manual feature extraction and selection.

We show that more than one hundred cells can be monitored simultaneously by the integrated system as they navigate through various microfluidic measurement modules within an enlarged field of view of ~21 mm^2. Five intrinsic markers, including electrical polarizability at three applied frequencies, transit time, and cell diameter, are extracted from the image stacks. Cell diameters obtained from the integrated system are shown to be highly correlated ($R = 0.95$, $p<0.05$) to those obtained from a Coulter Counter. Intrinsic markers, which are related to spatiotemporal positions of tracked cells (i.e., electrical polarizability at three frequencies and transit time), are obtained from the integrated system and validated with those obtained from a microscope system. With the integrated system, we demonstrate high-throughput multi-parameter measurements and classification of three leukocyte cell lines.

3.2 Digital Holographic Microscopy Overview

Digital holography is a computational imaging technique that allows a three-dimensional optical field to be recorded and reconstructed.[166] It has been widely used for a variety of applications, e.g., imaging, particle characterization, 3D object tracking, and microscopy.[167,168] Digital holography consists of two main operations: recording and reconstruction.[169] For recording, a known reference wave is introduced to coherently interfere with an unknown object wave, allowing the phase information of the unknown object wave to be converted to intensity variation. The intensity of the sum of the two complex wavefields, which now contains both the amplitude and phase of the unknown object wave, are then recorded by the recording media (e.g., CMOS sensor), which are only sensitive to the intensity of light. As a result, the recorded interference patterns (i.e., a hologram) can be digitally reconstructed to obtain an image of the original object. One commonly used image reconstruction technique is the angular spectrum approach. This approach is achieved by computing the Fourier transform of the recorded hologram,

multiplying it by the transfer function of propagation, and computing the inverse Fourier transform. The transfer function of propagation through linear isotropic meida is given as

$$H_z(f_x, f_y) = \begin{cases} e^{j2\pi z\frac{n}{\lambda}\sqrt{1-\left(\frac{\lambda f_x}{n}\right)^2-\left(\frac{\lambda f_y}{n}\right)^2}}, & \sqrt{f_x^2+f_y^2} < \frac{n}{\lambda} \\ 0, & otherwise \end{cases}$$

where f_x and f_y are the spatial frequencies, z is the distance between the sample plane and the sensor plane, n is the refractive index of the medium, λ is the wavelength of the light source.[160]

Various recording and processing schemes of digital holographic microscopy have been used in the literature, and are different in architectures, illumination sources, and modulation methods, among other aspects.[160,169,170] For example, digital holographic microscopy can be configured to operate in either transmission or reflection modes, using in-line or off-axis architectures, respectively.[171–173] Additionally, light sources with varying degrees of temporal coherence (which is related to their spectrum bandwidth) and spatial coherence (which is related to their size and implemented propagation distance) have been reported to affect the quality (e.g., sharpness, speckle noise) of the recorded holograms and of the reconstructed images.[174] Conventional holography uses light sources with near perfect spatial coherence (e.g., a laser on a small aperture (1-2 μm)) for illumination, and is disadvantageous as the usage of the small aperture size in these setups requires the setup to be mechanically stable and carefully aligned.[160] Incoherent or partially coherent sources with and without lenses have also been demonstrated for digital holography and have been shown to suppress the undesired coherent speckle noise, and allow simpler and robust optical setups.[175]

One variant of digital in-line holographic microscopes has been reported to image a transmissive sample with a large field of view and without the need for coherent sources or any bulky optical components. In this setup (Figure 3-1.), a light emitting diode (LED) butt-coupled to a pinhole is used to illuminate the sample.[160] It has been shown through a theoretical analysis that an incoherent illumination through a large aperture can be considered equivalent to coherent illumination of each object individually when the sample plane is close to the sensor plane (i.e., $\frac{z_1+z_2}{z_1} \sim 1$).[160] The interference fringe patterns between the light diffracted from the object and the unscattered light, which contain both the amplitude and phase of an object wave, are recorded on the sensor. This simple lensless incoherent holographic microscope was able to achieve subcellular

resolution (~1 to 2 μm) over a field of view of ~24 mm^2, making it suitable for applications that require collection or monitoring of a large number of microscale samples. This approach and its variations (e.g., color imaging, pixel super-resolution) have been applied to observe static polystyrene beads, blood smear, Papanicolaou smear, *Caenorhabditis elegans* samples, and to record three-dimensional trajectories of human sperms.[162,167,176]

More recently, deep learning has been applied to digital holography for image reconstruction and enhancement.[177] For example, AlexNet-based and VGG16-based architectures have been trained to predict the in-focus reconstruction depth from a single hologram of Madin-Darby Canine Kidney (MDCK) cell clusters.[178] Deep learning has also been implemented to infer phase recovery (i.e., removal of twin image artefacts) from a single hologram intensity after back-propagation has been applied. This technique enables a phase recovery that is 4-30 times faster than the state-of-the-art iterative reconstruction approach.[179] Wu et al. demonstrated a U-Net-inspired model that simultaneously perform autofocusing and phase recovery from a single hologram to extend the depth of field and reduce the reconstruction time of the holographic imaging system.[180] Cross-modality image transformation from the back-propagated holograms to the bright-field microscope images have also been reported using a generative adversarial network (GAN). With this network, a single recorded hologram is back-propagated at different depths and the back-propagated holograms are used to infer the high-contrast artefact-free bright-field microscope images.[181] Deep learning-enabled image enhancement, including super-resolution, and color imaging, have been shown by GAN-based approaches.[182,183] Furthermore, a U-Net model has been applied to accurately identify stained cells directly from holograms with high accuracy for the diagnosis of lymphoma.[184]

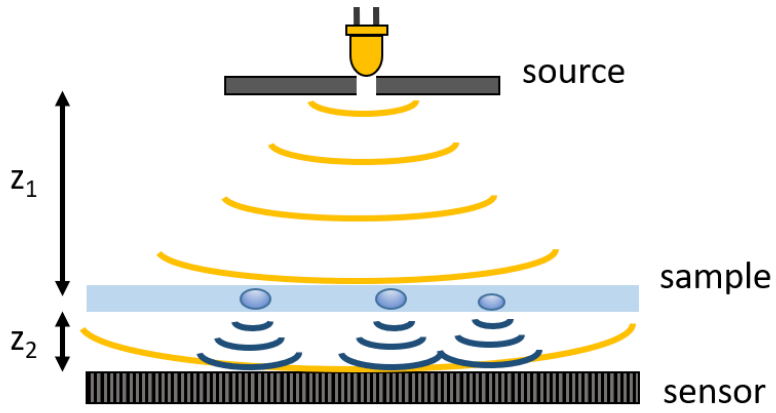

Figure 3-1. Digital holographic microscopy using partially coherent illumination. The system consists of an LED butt-coupled to a pinhole (~50-100 µm in diameter) and an optoelectronic sensor array. z_1 and z_2 represent the distance from the sample plane to the source and the distance from the sample plane to the sensor plane, respectively.

3.3 Materials and Methods

3.3.1 Digital holographic imaging system

The digital holographic imaging system is comprised of an Ultrabright LED (TLCY5800, Vishay Semiconductors), an aspheric condenser lens (Thorlabs), a 100-µm mounted precision pinhole (P100H, Thorlabs), and a 5-megapixel image sensor (MT9P031, Aptina/On Semiconductors). The LED light source ($\lambda = 590 \pm 17$ nm) was mounted in line with the condenser lens, the pinhole, and the CMOS image sensor (image format = 2592x1944, pixel size = 2.2 µm x 2.2 µm) as shown in Fig. 1. The microfluidic chip was mounted on the XY translational sample holder (XYFM1, Thorlabs) between the pinhole and the CMOS sensor. The distance from the pinhole to the microfluidic chip was ~3-5 cm. The distance between the microfluidic chip and the CMOS was ~2-3 mm.

3.3.2 Microfluidic platform

The microfluidic device was made of two components: 1) a 20-µm-high PDMS channel and 2) glass substrate with an ITO electrode layer (Figure 3-2 and Figure 3-4). The PDMS layer was fabricated by standard soft lithography and replica molding. The channel pattern contains a straight channel for the polarizability module and 72 parallel constriction channels for the deformability module. The glass substrate contains four pairs of ITO electrodes for DEP focusing and polarizability module. DEP focusing was used to concentrate cell samples for the downstream polarizability module. The electrode layer was fabricated from 1200-1600Å-thick ITO-coated

glass slides (CB-50IN-S105, Delta Technologies LTD) by photolithography and wet etching with a solution of hydrochloric acid (HCL), DI water, and nitric acid (HNO_3) at a ratio of 4:2:1 for three minutes. The two components were thoroughly cleaned with acetone, isopropanol alcohol, and methanol before plasma bonding. External electrical wires were connected to ITO pads with conductive epoxy.

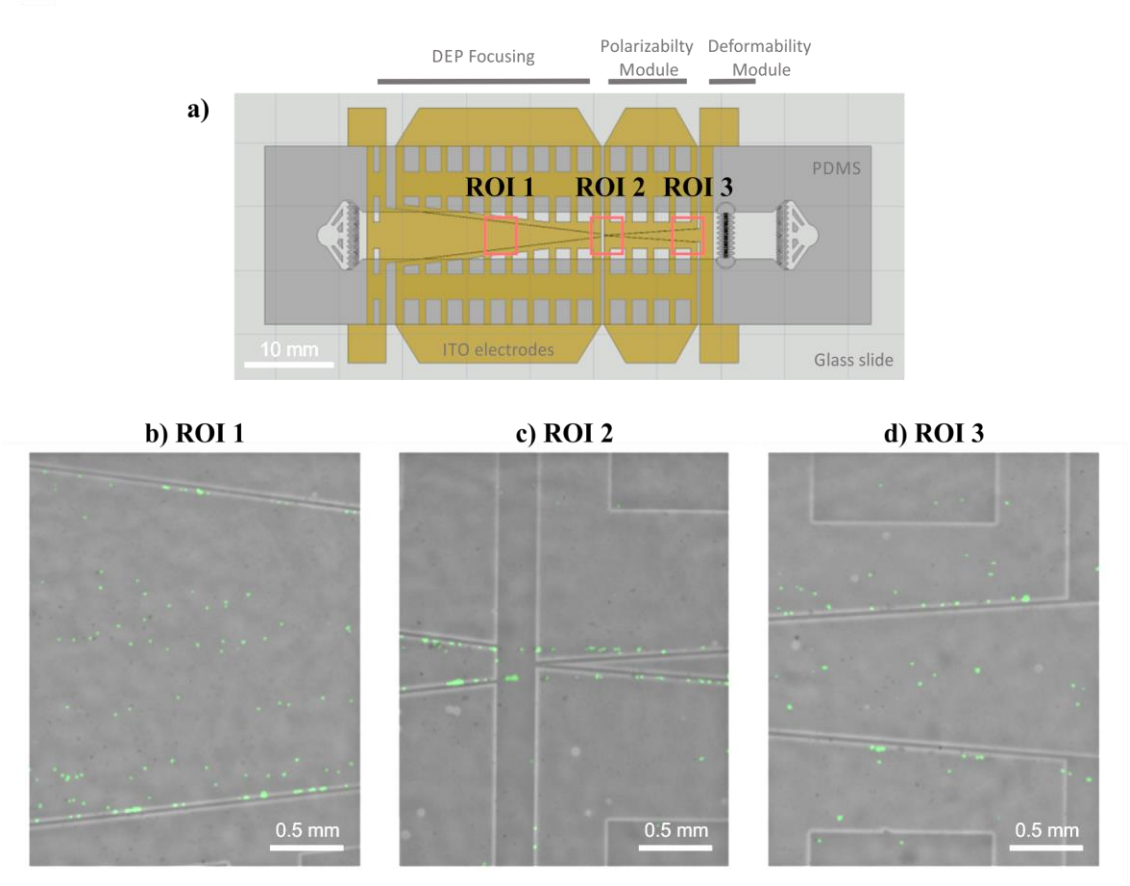

Figure 3-2. a) Device design. The device contains one inlet, DEP focusing region for cell enrichment, 2 pairs of parallel electrodes for polarizability measurement, 72 parallel constriction channels for deformability measurement, and one outlet. b-d) Bright-field micrographs with overlays of calcein fluorescence (green) of three regions of interest (ROI) in the DEP focusing region and the polarizability module.

3.3.3 Cytometry experiment

Prior to experiment, the microfluidic channel was pre-treated with 0.5% (w/v) Pluronic F108 in DI water until all bubbles were removed, followed by 7.5% bovine serum albumin for one hour to reduce nonspecific binding between cell samples and PDMS walls. For experiments, samples were resuspended in 13% Dextran in DPBS at a concentration of approximately $7x10^5$ cells/mL and injected into the microchannel by a syringe pump (Chemyx Fusion 200) with a constant flow

rate of 0.5 μL/min. The microfluidic platform was then placed under the digital holographic imaging system or a 5X objective microscope for imaging. The device was connected to function generators via a 50Ω coaxial cable with BNC connector. Customized MATLAB GUI was used to control the function generators (Agilent 33220A for frequency > 20MHz and Aim TTi TGR1040 RF for frequency > 20 MHz), mechanical SPDT switch box (USB-1SPDT-A18, Mini Circuits Laboratory), and either the microscope camera (PCO Sensicam QE) or the CMOS image sensor (Aptina/On Semiconductor). For microscopy validation, the device was observed with Zeiss Axio Imager m1m upright microscope with 5X objective and videos were recorded at ~ 11 fps for polarizability measurement and at ~ 20 fps for deformability measurement. For digital holographic imaging, videos were recorded at ~ 12 fps. The device was flushed with 13% dextran in DPBS buffer between samples.

3.3.4 Image pre-processing

All video recording, processing, and analysis were performed in MATLAB®2019b. Prior to experiment, raw holograms of the microfluidic platform without cell samples were recorded for 200 frames and median values across frames were saved as background image. Image registration was performed on the first frame of the stack by rotation and cropping such that microchannel was horizontally aligned with the horizontal axis of the image. Electrode centerlines and constriction channels were automatically located. Autofocusing was performed to estimate the distance between the sample plane and the image sensor plane. For autofocusing, the hologram was propagated to multiple z-distances within the expected distance range and Tenengrad variance[185] was calculated as relative focus measure. The z-distance with maximum focus measure was the estimated focus distance. Calculated registration parameters were saved.

During experiment, the acquired hologram image was pre-processed by background subtraction, registration, and scaling, using previously saved parameters.

3.3.5 Cell hologram detection algorithms

We created two datasets of pre-processed holograms from sixteen video recordings of four cell lines, including BA/F3, HL60, Jurkat, and K562, in two repeats of experiment. The datasets consisted image inputs as well as manually detected bounding box positions of cells. The training set contained 800 frames of holograms and the test set contained 80 frames of holograms. Each

frame contained ~80 – 200 cells. To ensure that there was no data leakage between the two datasets, the training set and the test set were derived from different video recordings.

As benchmark for automated cell detection performance, we performed image reconstruction on the full frame and used blob detection by Laplacian of gaussian filter and non-maximal suppression to detect focused cell images. Circular Hough transform and simple intensity thresholding were performed to detect cells in pre-processed holograms for comparison. Note that these algorithms required manual fine-tuning of parameters in each experiment for optimized detection accuracy.

For deep learning cell detection, a variant of YOLO v2 objector detector[164] was implemented using MATLAB Deep Learning Toolbox™. The architecture of the model is shown in Figure 3-3. It consists of a series of convolution, ReLU, batch normalization layers and max pooling layers for feature extraction, followed by YOLO transform layer and output layer, which transformed activations of the last convolutional layer into refined bounding boxes. The input image size was set to 1024 x 1024 pixels. Increasing network depth and input image size could increase detection accuracy as well as detection time. Three anchor boxes were calculated from the training dataset before training. The network was trained for 100 epochs using stochastic gradient descent with momentum at the learning rate was set to $1x10^{-5}$.

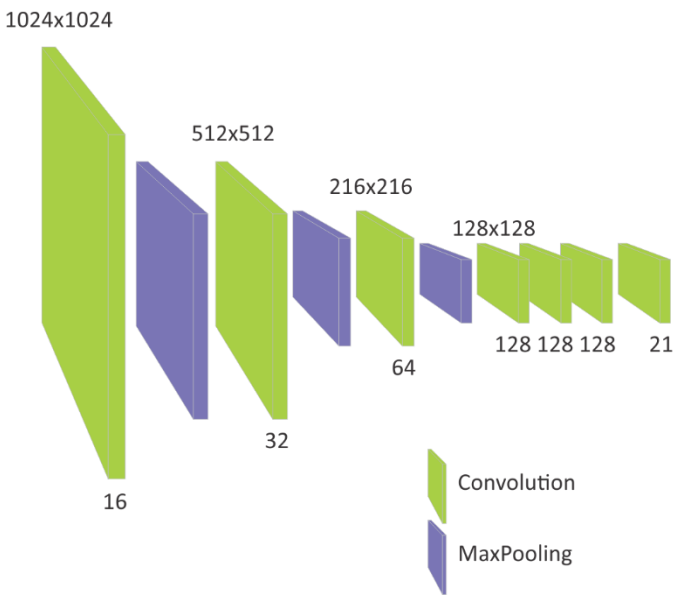

Figure 3-3. The architecture of the deep learning YOLO model for cell hologram detection. Note that all convolution layers except the last layer consist of 3 x 3 convolution kernels, and are followed by batch normalization and ReLU activation. The last convolution layer consists of 1 x 1 convolution kernels.

To evaluate performance of cell hologram detection algorithms, precision and recall of detection results compared to manually labelled data (ground truth) were computed. Detections were assigned to ground truth bounding boxes if overlap ratio was larger than 0.5. Processing time of the detection algorithms were the average processing time per frame of 80 frames in the test set.

3.3.6 Tracking algorithm

For multiple object tracking algorithm, a Kalman filter with constant velocity motion model was assigned to each new track and was used to predict location of the object in the next frame. A distance cost matrix between all possible combination of newly detected centroids on current frame and predicted centroids from previous frame were calculated. Since flow direction was known a priori, any detection-to-track assignment against the flow were assigned to infinity cost to prevent incorrect assignment. Detections were then assigned to tracks based on the optimal assignments which minimized the total cost by the Hungarian algorithm. Detections which had been assigned to tracks were used to update the Kalman filter motion model. Detections which had not been assigned to tracks initiated new tracks. Any tracks which did not have new detections for more than ten frames were saved and terminated.

3.3.7 Parameter extraction

For cell diameter measurement, cropped tiles of cell hologram in the polarizability region from detection algorithm were propagated to the focus plane. Intensity thresholding was applied, and equivalent diameter was calculated from the binary mask as $2 \cdot \sqrt{area/\pi}$.

For cell polarizability measurement, a repeating series of 0.5 MHz, 2 MHz, and 25 MHz sinusoidal waveforms were applied to coplanar electrodes with a period of 5 seconds for each frequency. Balance positions at a specific applied frequency were calculated from perpendicular distances from cell centroids to the nearest electrode centerline within the last five frames before the next frequency was applied. To extract real part of the Clausius-Mossotti factor (Re[CM]) from balance positions, we calculated average balance positions with respect to x-distance of 10-μm size standard polystyrene beads at three applied frequencies. From force balance equation, system parameter $C_1(x)$ for each frequency can be estimated from[186]:

$$C_1(x) = \frac{18Q \sin\theta}{V_{RMS}^2 w h^3 \epsilon_m p(f)} = \frac{Re[CM] \cdot R \cdot q_R(\delta)}{h - R}$$

where Q is volumetric flow rate, θ is angle between electrode centerline and channel, V_{RMS} is the applied RMS voltage, w is channel width, h is channel height, ε_m is media permittivity, p(f) is a function that corrects for frequency-dependent voltage drop at the electrode/solution interface, R is object radius, δ is balance position, and q_R is a function that reflects positional dependency of the DEP force. Re[CM] can then be extracted from cell balance positions by:

$$Re[CM] = C_1(x)\frac{\mathrm{h} - \mathrm{R}}{\mathrm{R} \cdot q_R(\delta)}$$

For deformability measurement, region of interest (ROI) was specified across the narrowest constriction channels. Time difference corresponding to the first and last frame that a cell stayed in the ROI was determined as transit time.

3.3.8 Data analysis

The nonparametric Kruskal-Wallis tests and the follow-up multi comparison tests were performed to compare the medians of >2 distributions for each intrinsic marker, with determination of statistical significance.

For classification of the three leukemia cell lines, the dataset containing the multiple intrinsic markers measured from our platform was split into training and test sets with an 80-20 ratio. The random forest models were trained to classify cell types, and were optimized for hyperparameters using five-fold cross validation. The AUC and confusion matrix of the final model performed on the test set were computed to show classification accuracy. To evaluate the impact of each marker on the classification accuracy, predictor importance were calculated by summing the improvements in the split criterion due to splits on every predictor and dividing the sum by the number of branch nodes.

3.3.9 Cell Culture

BA/F3 murine interleukin-3 dependent pro-B cell line, Jurkat human immortalized T lymphocyte cell line derived from an acute T cell leukemia, and K562 human immortalized myelogenous leukemia cell line were cultured according to ATCC protocols and were passaged ~3-4 days at 1/10 dilution. The cell culture medium was prepared from RPMI-1640 with high glucose content, L-Glutamine, and phenol red indicator, supplemented with 10% fetal bovine serum, 1% L-glutamine, 1% penicillin-streptomycin, 1% Sodium Pyruvate, and 1% MEM non-essential amino acids.

HL60 human acute promyelocytic leukemia cell line was cultured according to ATCC protocols and were passaged ~2-3 days to maintain cell density between $1x10^5$ and $1x10^6$ cells/mL. The cell culture medium was prepared from RPMI-1640 with high glucose content, L-Glutamine, and phenol red indicator, supplemented with 10% fetal bovine serum, and 1% penicillin-streptomycin.

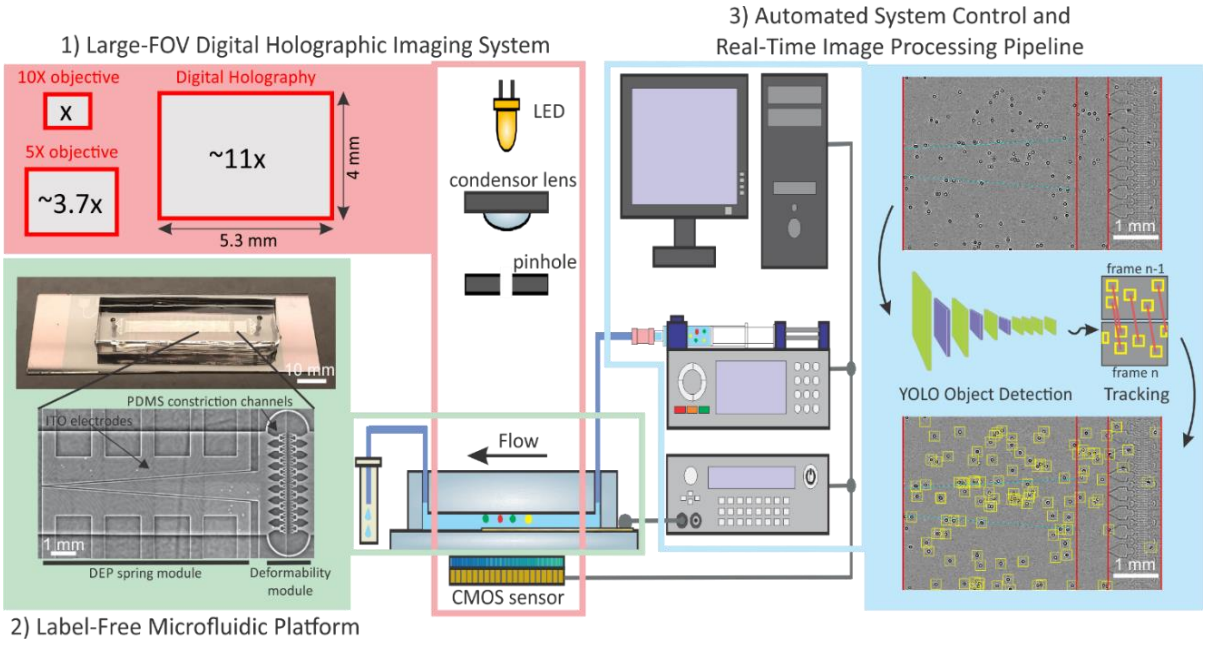

Figure 3-4. System overview of the real-time, cell-tracking, intrinsic cytometer platform, showing three main components: 1) large-FOV digital holographic imaging system, 2) label-free microfluidic platform and 3) automated system control and real-time image-processing pipeline.

3.4 Results and Discussion

3.4.1 System Overview and Design Considerations

The cell-tracking intrinsic cytometry system (Figure 3-4) consists of three main components: 1) large-FOV digital holographic imaging, 2) a label-free microfluidic platform, and 3) an automated system control and real-time image-processing pipeline.

Large-FOV microscopy for dynamic imaging can be achieved by several techniques, including optical lens systems,[187] digital in-line holography,[188–190] Fourier ptychography,[191,192] etc. Among these techniques, digital in-line holography is an attractive choice as it has the minimal overall hardware and software requirements (e.g., number of optical components, optical alignment, number of images needing to be recorded per view, and image reconstruction process) and as it can be scaled up further simply by using an image sensor with increased active area. We adapt a partially coherent digital holographic imaging technique, introduced in Mudanyali et al.[160], which utilizes a simple light emitting diode (LED), a 100-μm pinhole, and a CMOS image sensor. Digital holography is a two-step lens-free computational imaging technique, which allows information of both amplitude and phase of the diffracted waves from an object (i.e., hologram) to be recorded and to be reconstructed numerically afterwards.[169] By placing samples close to the

CMOS sensor, Mudanyali et al.[160] showed that a hologram with an area equal to the active area of the implemented CMOS sensor could be acquired. Our imaging system can acquire images with a field of view of ~ 21 mm^2, which is ~11 times larger than the FOV of a typical 10X microscope objective and ~3.7 times larger than the FOV of 5X microscope objective. To capture rapid dynamics of cells in the microfluidic platform, the CMOS sensor is set to capture videos at ~ 10-11 fps.

To maximize the usage of the imager's enlarged field of view, our previously reported multiparameter intrinsic cytometry platform[193] has been expanded to accommodate 72 parallel constriction channels for deformability measurement as well as two pairs of transparent electrodes for polarizability measurement. We used transparent indium tin oxide (ITO) layers for the electrodes to minimize optical aberrations associated with the transmission mode of the imaging system. Device designs and experimental protocols, including constriction channel width, flow rate, cell concentration, and frequency sequence setting, were optimized experimentally for the throughput-sensitivity trade-off.

An integral part of a cell-tracking cytometry is the ability to analyze large amounts of time-lapse image stacks quickly and accurately, as the final throughput and sensitivity of the overall system depend on both microfluidic throughput and image processing throughput. Visual recognition tasks such as object detection and tracking, which are intuitive to humans, are complicated computational problems.[194] Traditional object detection algorithms, including intensity thresholding, edge detection, and circular Hough transform, often rely on manual extraction and selection of image parameter, such as intensity, object area, and object shape, which can vary across experiments and conditions, and are susceptible to background noise. On the contrary, deep convolutional neural network models can be customized and trained to recognize invariant, two-dimensional features of task-specific objects, surpassing traditional methods that rely on manual feature selection in both processing time and accuracy.[195] In the next section, we investigate the performance of various object detection algorithms to determine the most suitable option for our application.

3.4.2 Cell Hologram Detection and Tracking

An example of a preprocessed hologram image is shown in Figure 3-5. Background subtraction in image preprocessing partially removed PDMS channels as well as electrode

structures, and enhanced cell hologram signals in the acquired image. In the polarizability region, cell hologram signatures were expected to appear as circular fringe patterns because shapes of suspension cells were roughly spherical. As cells traversed through constriction channels in the deformability region, cell hologram signatures became distorted into irregular shapes and intensity patterns because of cell deformation and interference from PDMS constriction channel structures.

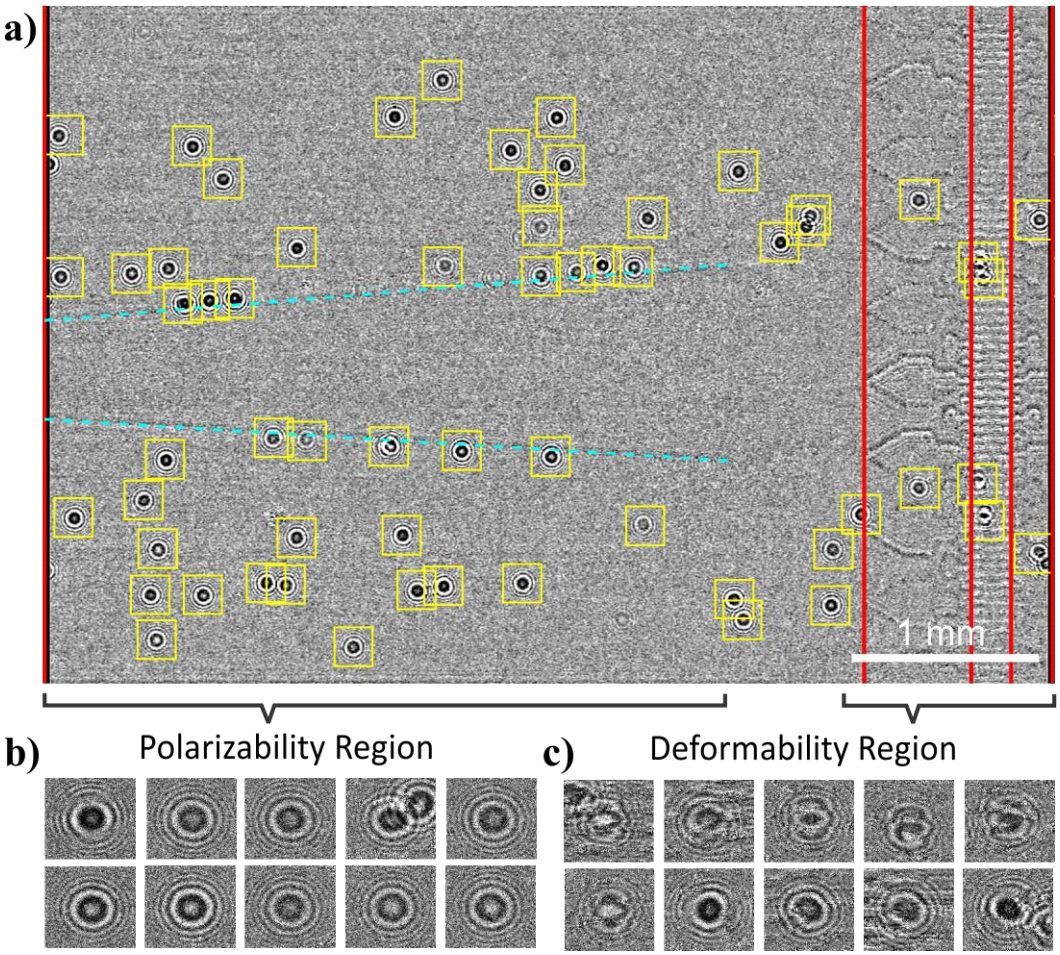

Figure 3-5. Cell hologram detection. a) A hologram recorded by the digital holographical imaging system after image registration and background subtraction. Yellow bounding boxes indicate cell detection. Cyan dash lines indicate electrode centerlines. Red dash lines depict the beginning of deformability region as well as the narrowest constriction location. b-c) multiple exploded views of cell holograms in the polarizability region and the deformability region, respectively.

To establish a benchmark for automated cell detection, we computationally reconstructed the preprocessed holograms, applied a blob detection technique, and morphological operations to detect focused cell images. On the contrary, other cell detection techniques were applied to preprocessed holograms without reconstruction to reduce the processing time. Object detection

algorithms using manual feature selection, including circular Hough transform and intensity thresholding, were implemented and tested. In addition, the deep learning YOLO object detector, the state-of-the-art real-time object detection algorithm which has been applied to detect hundreds of categories of common objects in real-world image datasets, was trained with the pre-processed cell hologram images and tested. Figure 3-6(a-b) shows the precision-recall curves of the four different object detection techniques on the test image dataset compared to the ground truth, which was manually labelled. As the number of objects and the detection performance in the polarizability and the deformability regions were expected to be different, we calculated the precision-recall curves on these two regions separately. The average precision (AP) of each cell hologram detection technique, which was the average precision value for the recall value over 0 to 1, was summarized in Figure 3-6c. High-performance object detection techniques were expected to achieve high average precision, i.e., maintain high precision (low number of false positives) as recall improved (low number of false negatives). The mean average precision over the two regions of the four techniques was 0.73, 0.66, 0.57, and 0.85, respectively.

In the polarizability region, the average precision of the benchmark blob detection on the reconstructed images, and of the circular Hough transform, thresholding, and YOLO on the hologram images were 0.96, 0.95, 0.73, and 0.95, respectively. The performance of the YOLO model was comparable to the circular Hough transform. However, the benchmark blob detection technique on reconstructed images achieved the highest accuracy because it was able to distinguish cells that were extremely close together, whereas the circular Hough transform and YOLO were not able to resolve highly overlapping cell holograms as two objects. On the contrary, intensity thresholding was not able to achieve high precision, i.e., there were still many false negatives, possibly because intensity thresholding was not able to separate two cell holograms that were touching each other.

The generally smaller area under the precision-recall curves in the deformability region (Figure 3-6b) compared to the precision-recall curves in the polarizability region (Figure 3-6a) among all tested algorithms indicated that cell holograms in the deformability region were more challenging to detect than cell holograms in the polarizability region. In the deformability region, the average precision for the four detection techniques was 0.49, 0.37, 0.41, and 0.74, respectively. Low average precision (<0.5) of the benchmark blob detection, the circular Hough Transform, and

the intensity thresholding techniques suggested that the algorithms performed poorly in this region, which was expected, since many cell holograms were no longer circular and there was high background noise in this region. In contrast, YOLO, which was trained to recognize irregular intensity patterns of deformed cells in noisy background, was able to perform significantly better than the other techniques, including the benchmark blob detection on reconstructed images which suffered from imperfect reconstruction of cell holograms in constriction channels.

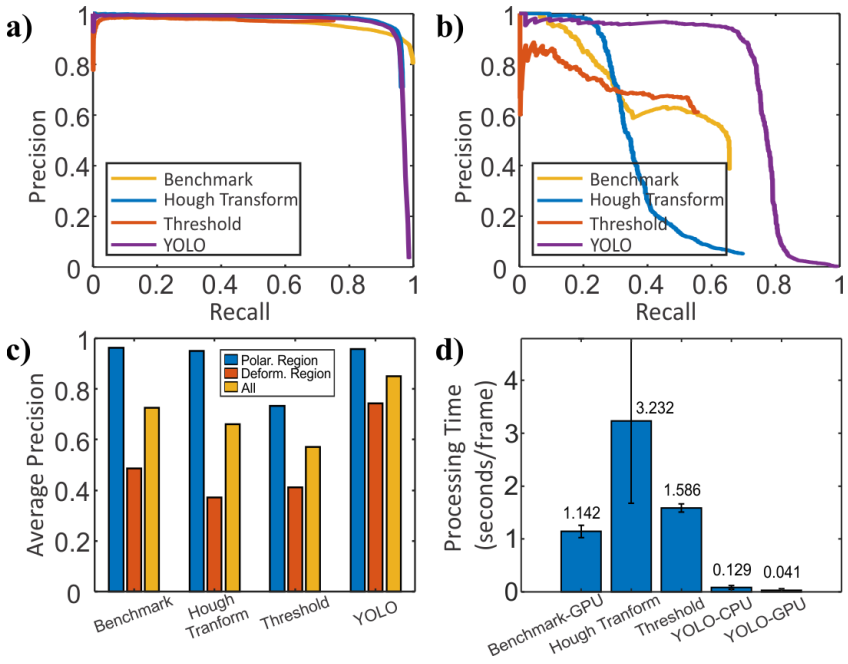

Figure 3-6. a) Precision-recall curve of four cell detection algorithms in the polarizability region, including the benchmark blob detection on reconstructed image, circular Hough transform, thresholding, and YOLO on pre-processed holograms. b) Precision-recall curve of four cell detection algorithms in the deformability region. c) Average precision of the four cell detection algorithms in the polarizability region, the deformability region, and the overall average across the two regions. d) Average processing time per frame. The error bar indicates the standard deviation.

Besides detection accuracy, another important performance measure of an object detection algorithm is the processing time. According to Figure 3-6d, the processing time of YOLO on a CPU (Intel® Core™ i7-9750H) and GPU (NVIDIA® GeForce® RTX™ 2070) was ~14 and ~40 times faster than the benchmark blob detection on the reconstructed images with the GPU. In contrast, the traditional circular Hough transform and intensity thresholding were ~3 and ~1.5 times slower than the benchmark. Among all object detectors, the circular Hough transform exhibited the largest variation in processing time because it relied on edge detection to find relevant pixels and a scoring technique to keep scores for circle centroid candidates. As more object pixels

or more noise pixels were determined to be relevant, more processing time was needed to calculate the scores. In contrast, YOLO displayed the smallest variation in processing time as the processing time of YOLO in each frame did not largely depend on the number of target objects. Taking both the detection accuracy and the processing time into consideration, we chose to integrate the YOLO object detector into our image processing pipeline.

3.4.3 Extraction and Validation of Cell Diameter obtained from Digital Holographic Imaging System

Acquired images from digital holographic imaging were not focused images of objects, but rather holographic diffraction patterns formed by interference of light waves diffracted from objects and unscattered LED light.[169] As a result, object diameters were not readily available for extraction, and numerical reconstruction of hologram images had to be performed to reconstruct focused images of objects and retrieve object diameter information. To extract the diameter of undeformed objects, we performed image reconstruction on the acquired holograms only in the designated polarizability region where objects were not expected to be deformed. Examples of holograms and reconstructed images of standard size polystyrene beads and four cell lines are shown in Figure 3-7a. As expected, we observed fringe patterns in the hologram images that were unique for each object class as the LED light was absorbed and diffracted differently by each object, depending on its size, morphology, refractive index, and subcellular components. After numerical reconstruction, intensity thresholding was applied to locate the focused images of the objects and equivalent diameters of objects were calculated. Since an object usually takes more than one hundred frames to traverse the polarizability region, image reconstruction and diameter extraction was performed every tenth frame to maintain rapid image processing. The final diameter was estimated from the median of repeatedly extracted diameter values associated with its track.

To validate extraction of object diameter obtained from digital holographic imaging, we performed diameter extraction of standard size polystyrene beads with diameters of 6 μm, 10 μm, and 15 μm, respectively, in our system and compared the obtained distribution with a diameter distribution obtained from a Coulter Counter. According to the results, the standard deviation of repeated bead diameter extraction within each track was below 7.25%, 5%, and 3.6% for 6 μm, 10 μm, and 15 μm polystyrene beads, respectively. Overall, the average deviation of the extracted diameter within each track, representing the precision of the object diameter extraction algorithm, was below ~0.5 pixels, which corresponded to 1.1 μm. Mean diameters of 6 μm, 10 μm, and 15

μm polystyrene beads measured from the digital holographic imaging system were 6.35±0.62, 9.64±0.92, 15.83±1.38 μm, respectively. Mean diameters of 6 μm, 10 μm, and 15 μm polystyrene beads obtained from Coulter Counter were 6.08±0.20, 10.03±0.67, and 15.7±0.78 μm, respectively. Figure 3-7b shows that the means of the three-sized bead distributions obtained from our system were highly correlated to those obtained from Coulter Counter ($R = 0.9974$, $p<0.05$). In addition, we compared distributions of cell diameters of four cell lines, namely BA/F3, HL60, Jurkat, and K562, obtained from our system compared to Coulter Counter measurement with one repeat (Figure 3-7c) and showed correlation of 0.9544 ($p<0.05$).

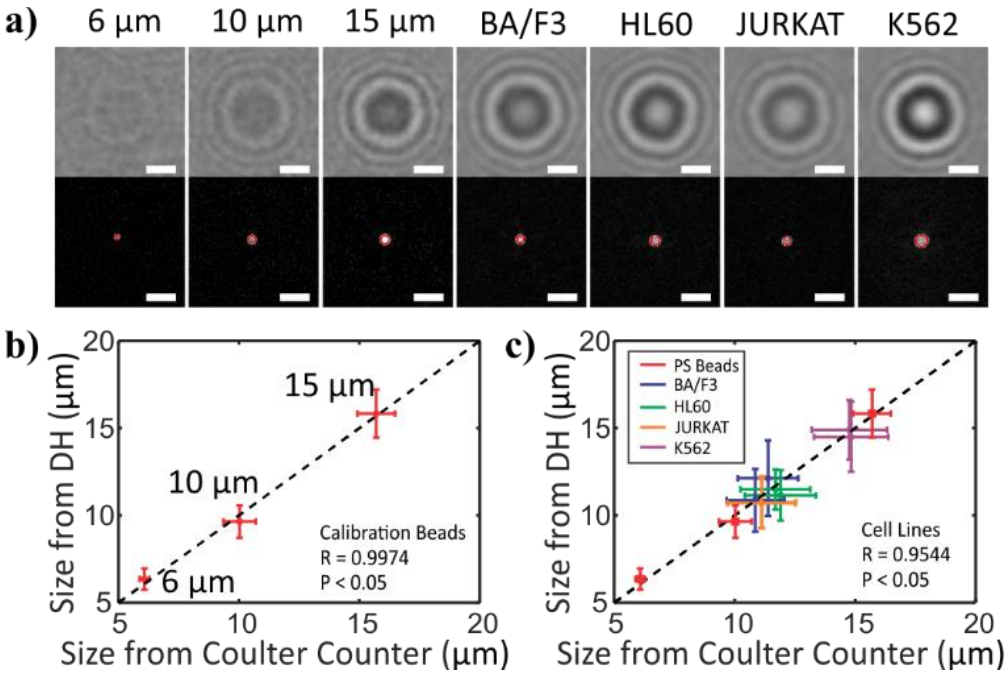

Figure 3-7. Cell diameter measurement. a) Holograms and reconstructed images of 6 μm, 10 μm, 15 μm polystyrene microspheres, and four cell lines, including BA/F3, HL60, JURKAT, and K562. Scale bars depict 50 μm. b) Size measurement from digital holographic imaging and from Coulter Counter of three sized polystyrene beads. c) Size measurement from digital holographic imaging and from Coulter Counter of BA/F3, HL60, JURKAT, and K562 cell lines

3.4.4 Extraction and Validation of Multi-frequency Polarizability and Deformability from Cell Detection on Pre-processed Holograms

Characterization of multi-frequency polarizability from balance positions with the DEP spring technique and characterization of constriction-based deformability from transit time allow these intrinsic markers to be estimated from spatiotemporal positions of cells. To associate cell hologram detections which corresponded to the same cells over time, we implemented a customized multiple

object tracking algorithm based on motion estimation using the Kalman filter. The cost matrix between all possible pairs of object centroids detected on the current frame and predicted centroids from the Kalman filter were calculated based on Euclidean distance. Detections on the current frame were assigned to tracks based on cost minimization using the Hungarian assignment algorithm. The cost of any assignment which would result in motion against the flow direction was set to infinity to prohibit such assignment. The spatiotemporal positions of cells were then recorded and stored for analysis.

Figure 3-8a shows tracking of a cell traversing across the measurement modules, as obtained from the digital holographic imaging system. For multi-frequency polarizability, the perpendicular distance from the detected cell centroids to the nearest electrode centerline and the corresponding applied DEP frequencies (0.5 MHz, 2MHz, and 25 MHz) are shown in Figure 3-8. Balance positions, determined from the perpendicular distance from the cell centroids to the nearest electrode centerline within the last five frames of each applied frequency, were extracted and used to estimate the real part of the Clausius-Mossotti factor (Re[CM]), an indicator of electrical polarizability. Figure 3-11c plots time versus x-distance of the same cell as it travelled across the deformability region. Transit time, an indicator of cell deformability, was calculated as the time span that a cell required to travel through the region of interest designated by the two red dash lines.

As the deformability measurement module has been expanded to 72 parallel channels, we quantify the variation of transit time measurement within each parallel channel as obtained from the microscope imaging. Figure 3-9 and Figure 3-10 show overlays of cell trajectories, total number of cells that pass through, and combined transit time distribution within each of the middle 56 constriction channels at two different flow rates, respectively. The overlay of cell trajectories reveals the shape of the constriction channels, which verifies our tracking algorithm, as well as the channels that might be clogged. The total number of cells that passed through each constriction channel shows lower number for channels that were clogged. On average, median transit time of each channel is 0.51 ± 0.08 seconds and 0.32 ± 0.07 seconds (mean ± SD) for the flow rate of 0.5 μL/min and 1 μL/min, respectively.

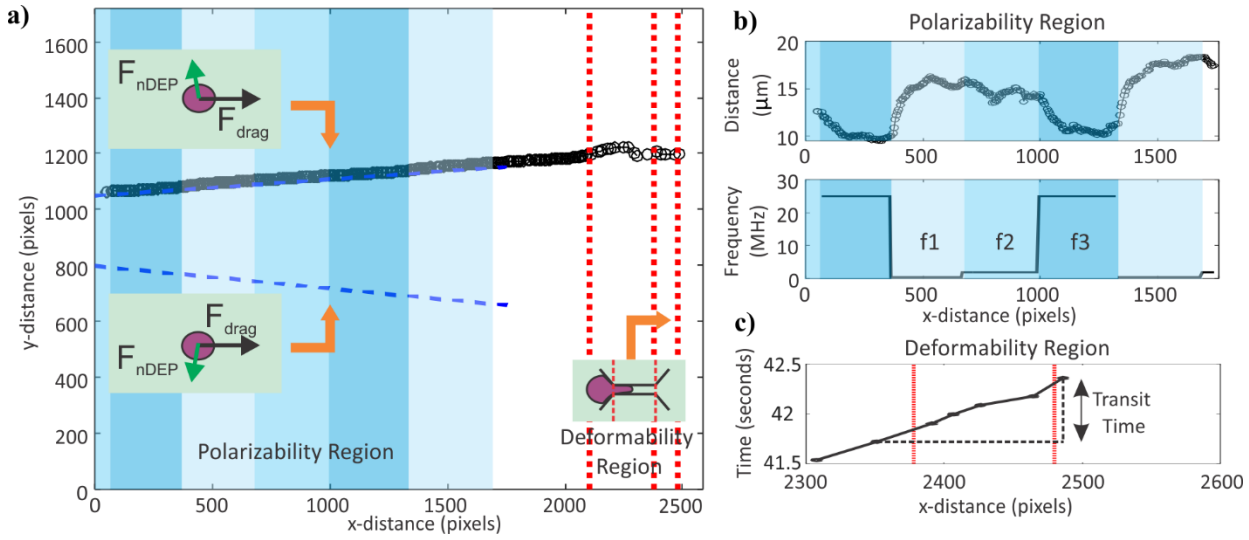

Figure 3-8. Multi-frequency polarizability and deformability measurement. a) cell trajectory across the active region of the platform. Blue dash lines depict electrode centerlines of two electrode pairs. Red dash lines indicate deformability region and measurement ROI. b) Perpendicular distance from cell centroids in a) to the nearest electrode centerline versus x-distance (top) and the corresponding applied frequency (bottom). c) Time as the cell in a) travelled across the narrowest constriction channel. Two dash lines indicate transit time measurement ROI.

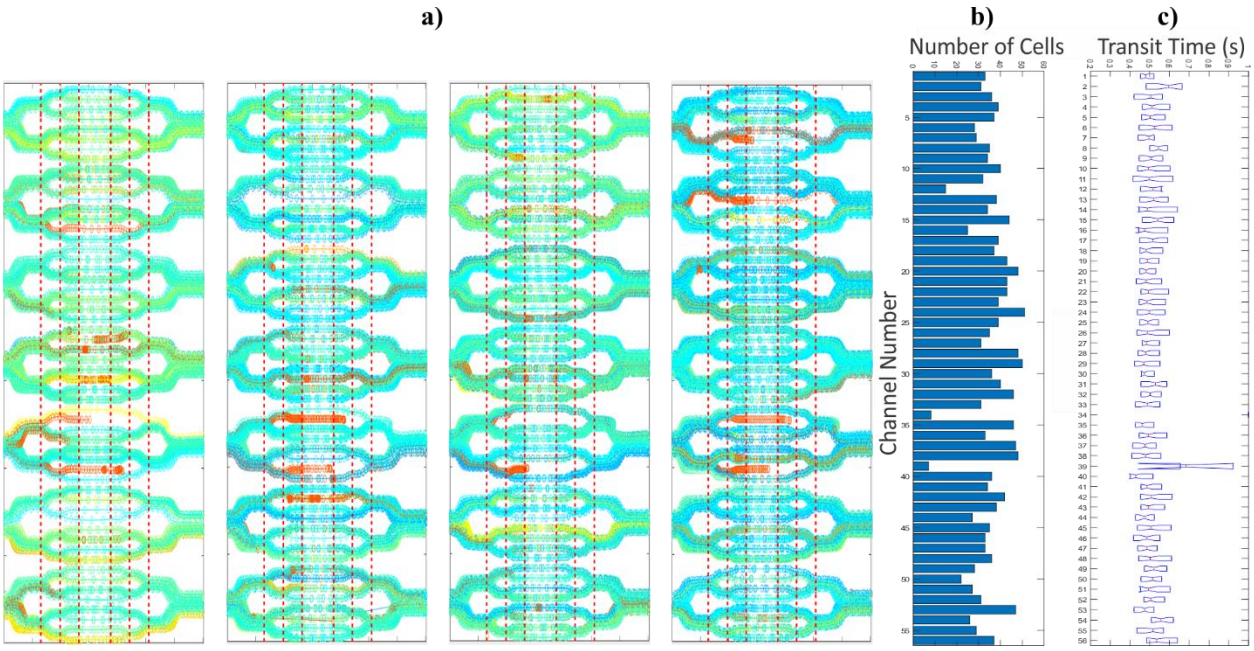

Figure 3-9. Measurement of the transit time of ~6-µm microspheres through 8-µm constrictions at the flow rate of 0.5 µL/min as obtained from the microscope imaging system. Note that the middle 56 channels out of 72 channels were monitored by the microscope imaging system due to limited field of view. a) Overlay of microspheres' trajectories from four runs within the same device. The color of each trajectory reflects the corresponding transit time (blue indicates small transit time while red indicates large transit time). b) Total

number of cells that passed through each of the parallel constriction channels. c) Boxplots showing accumulated transit time distribution within each channel.

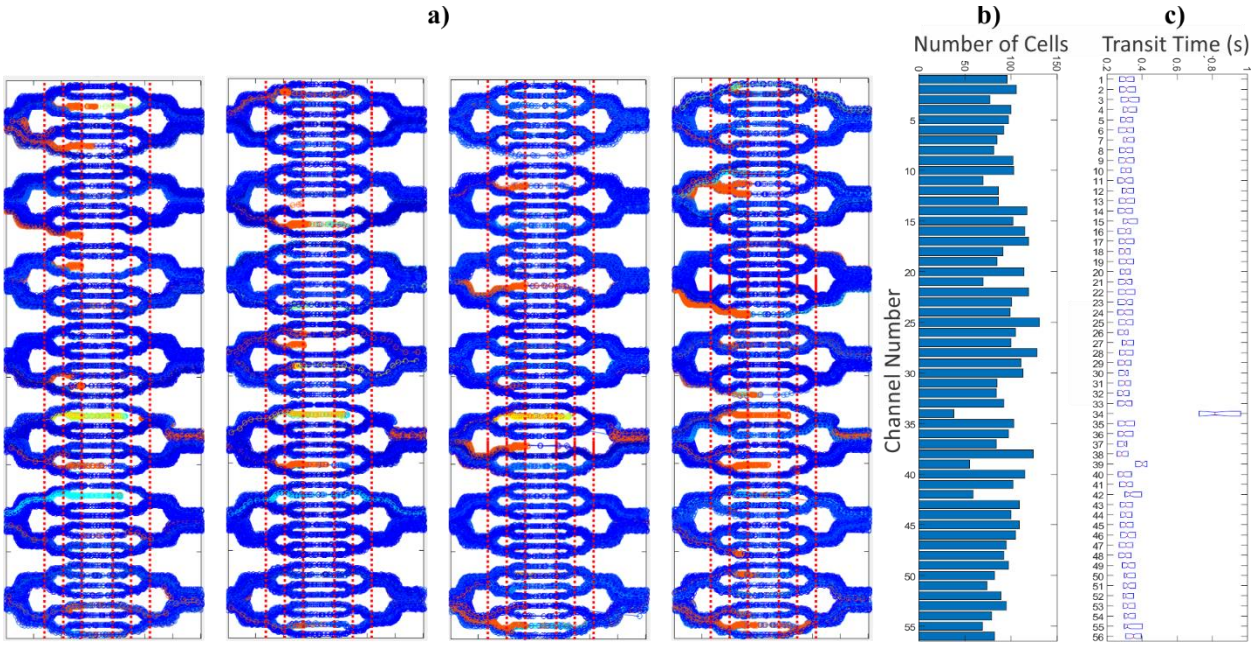

Figure 3-10. Measurement of the transit time of ~6-µm microspheres through 8-µm constrictions at the flow rate of 1 µL/min as obtained from the microscope imaging system. Note that the middle 56 channels out of 72 channels were monitored by the microscope imaging system due to limited field of view. a) Overlay of microspheres' trajectories from four runs within the same device. The color of each trajectory reflects the corresponding transit time (blue indicates small transit time while red indicates large transit time). b) Total number of cells that passed through each of the parallel constriction channels. c) Boxplots showing accumulated transit time distribution within each channel.

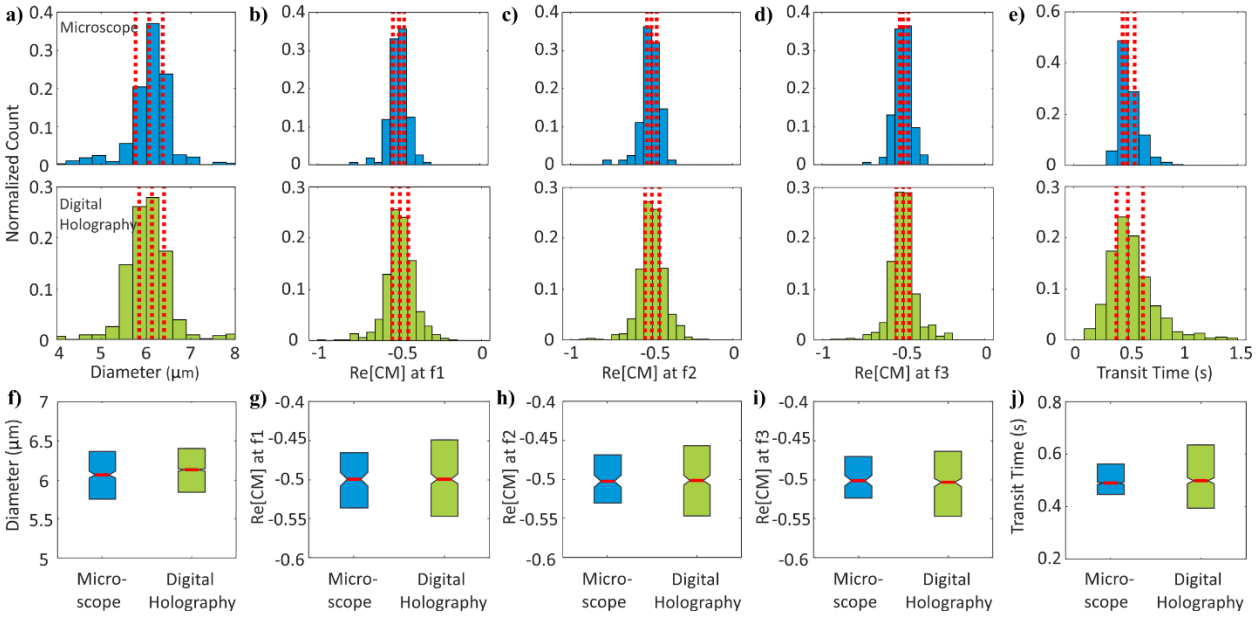

Figure 3-11. Characterization of size standard polystyrene microspheres with mean diameter of 6.20±0.50 μm by the microscope imaging system and the digital holography system. The results show combined data points from three replicates within the same device for each of the two imaging systems. a) Diameter measurements from microscope system (top, n = 579) and digital holography (bottom, n = 3849). b) Re[CM] measurements at the applied frequency of 0.5 MHz from microscope system (top, n = 200) and digital holography (bottom, n = 605). c) Re[CM] measurements at the applied frequency of 2 MHz from microscope system (top, n = 210) and digital holography (bottom, n = 592). d) Re[CM] measurements at the applied frequency of 25 MHz from microscope system (top, n = 180) and digital holography (bottom, n = 584). e) Transit time measurements from microscope system (top, n = 1494) and digital holography (bottom, n = 1199). Red vertical dashed lines indicate 25, 50, and 75 percentiles. f-j) Corresponding boxplots showing 25, 50, and 75 percentiles of the distributions of the five markers.

To verify that object centroids extracted from pre-processed holograms could provide accurate positions of cell centroids required to extract cell polarizability and cell deformability, we performed comparison study between the microscope imaging system and the digital holography system by characterization of size-standard polystyrene microspheres and two cell lines. Note that, for microscope imaging analysis, image stacks with smaller FOVs were acquired and the two measurement modules were monitored separately since microscope imaging could not be used to observe the entire active region of the microfluidic platform simultaneously.

To quantitatively compare the two imaging modalities for the measurements of polarizability and deformability, polystyrene microspheres (6.20±0.50 μm diameter) were characterized using the microscope-based cell-tracking cytometer and the digital holography-based cytometer (with the benchmark blob detection on reconstructed images) are shown in Figure 3-11. The standard

deviations of the balance positions at three frequencies measured from digital holography-based system (< 1.70 μm or 9.9%) were larger than those from microscope-based system (< 1.26 μm or 7.2%). The differences in balance position extraction between the two imaging modalities were expected as there were different specifications in the imagers (e.g., pixel size and magnification) and in the extraction algorithms. Similarly, the standard deviations of the transit time measured from microscope imaging and from digital holography were ~0.10 seconds and ~0.21 seconds, respectively, which were approximately twice the inverse of the imagers' frame rates.

In addition, we showed that the digital holography-based system with a YOLO cell hologram detector was sufficient to distinguish the differences in polarizability and transit time between two cell lines, in agreement with the results from the microscope-based system. Box plots representing distributions of Re[CM] at three frequencies of two leukocyte cell lines, namely BA/F3 and K562, obtained from the digital holographic imaging and from the microscope imaging are shown in Figure 3-12(b-d). Two general trends emerged that were consistent between the two imaging systems. First, as expected, magnitudes of Re[CM] generally decreased as frequency increased ($f1<f2<f3$). Second, the median Re[CM] of BA/F3 populations were larger in magnitude than the median Re[CM] of K562 population for frequency f1 and frequency f3 ($p<0.05$). While there might be some discrepancy in the estimated Re[CM] values measured from the two imaging systems as a result of device-to-device variations and differences in the imagers' spatial resolution, consistency in general trends and statistical analysis showed that Re[CM] estimates from the digital holographic imaging system were in quantitative agreement with the microscope imaging system, resolving the differences in Re[CM] measurements of the two cell lines. Box plots representing distributions of transit time of the two cell lines obtained from the two imaging systems were shown in Figure 3-12e. Both imaging systems consistently showed that the quantiles of transit time were larger in K562 compared to BA/F3. We showed that similar quantitative parameter extraction from particles' dynamics can be obtained from the two systems.

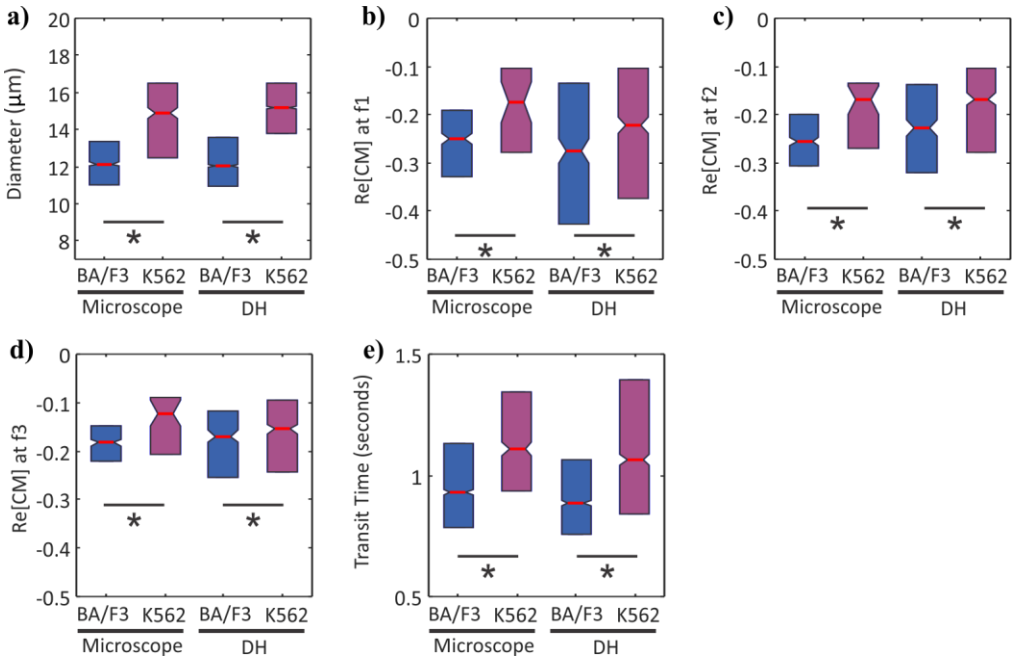

Figure 3-12. a) Boxplots of diameter measurements of BA/F3 and K562 cell lines obtained from microscope imaging and from digital holographic imaging. b-d) Boxplots of Re[CM] measurements at three different frequencies of BA/F3 and K562 cell lines obtained from microscope imaging and from digital holographic imaging. e) Boxplots of transit time measurements of BA/F3 and K562 cell lines obtained from microscope imaging and from digital holographic imaging. * indicates that there is a significant difference among cell populations ($p<0.05$).

3.4.5 Multi-parameter Characterization of Single-cells

To show specific application of the large-FOV real-time integrated system, we performed multiparameter characterization and classification of three established leukemia cell lines, which have been used as cell models to study human leukemia cell deformability and drug response,[196–199] including HL60 acute promyelocytic leukemia, JURKAT acute T lymphocytic leukemia, and K562 chronic myelogenous leukemia. Multiparameter measurements of five intrinsic markers, including cell diameter, Re[CM] at three frequencies, and transit time, of the three cell lines obtained from our integrated system, are shown as boxplots in Figure 3-15(a-e) and as scatter plots in Figure 3-13. To assess the discriminating power of the five measured intrinsic markers, a Random Forest model was trained to classify the three leukemia cell lines using the measurements of these markers as input. Receiver operating characteristic (ROC) curves and confusion matrices, illustrating the ability of the trained classifier to distinguish between the three cell lines in the test dataset, are shown in Figure 3-15(f-g). The overall classification accuracy was 73.1%.

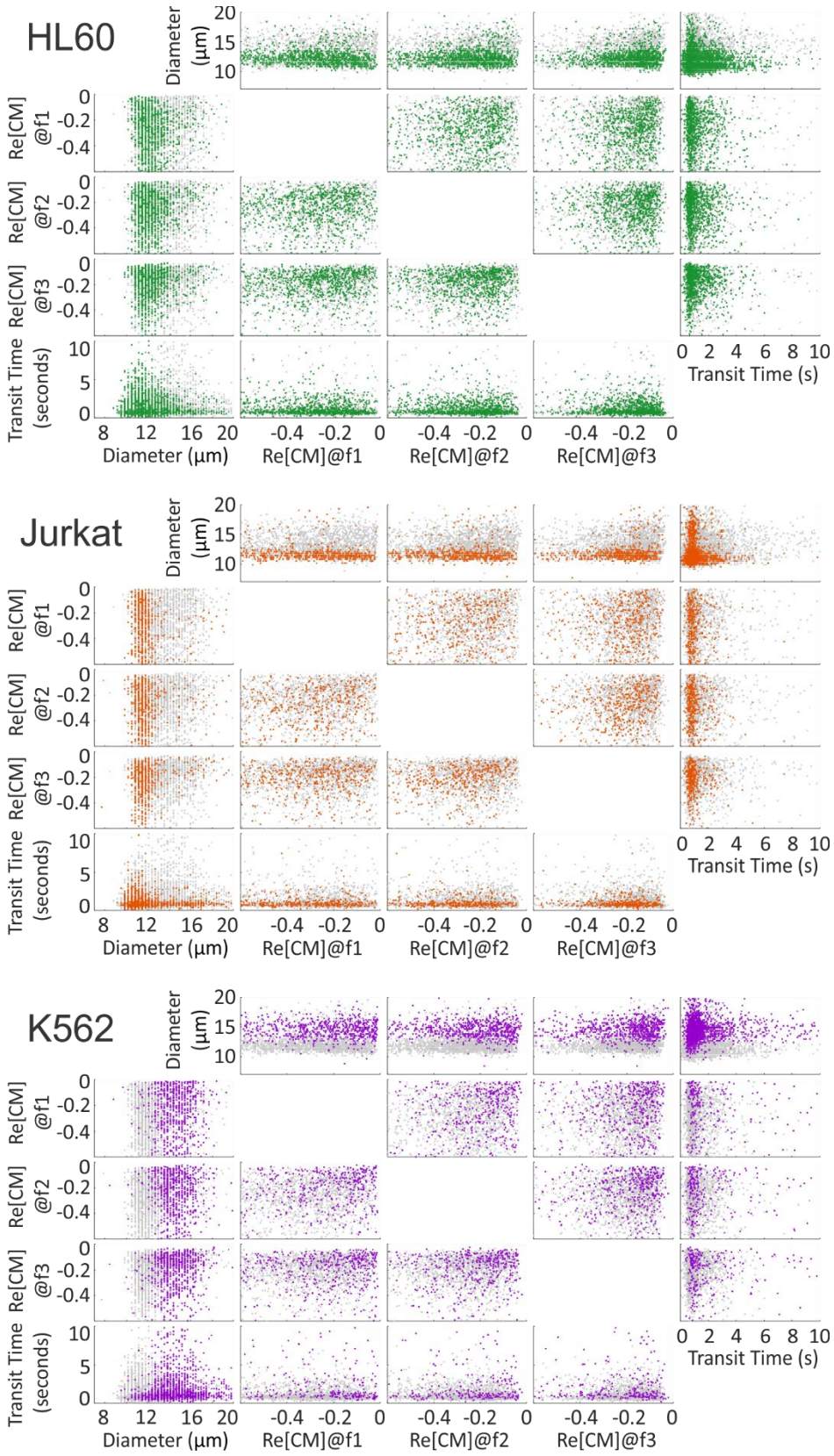
HL60
Jurkat
K562
Diameter (µm)
Re[CM] @f1
Re[CM] @f2
Re[CM] @f3
Transit Time (seconds)
Transit Time (s)
Diameter (µm)
Re[CM]@f1
Re[CM]@f2
Re[CM]@f3

Figure 3-13. Scatter plots showing characterization of five intrinsic markers, including cell diameter, Re[CM] at three different frequencies, and transit time, measured from the integrated platform for HL60 (green, n = 10,559), Jurkat (orange, n = 5169), and K562 (purple, n = 4627) cell lines. The results are combined data from four replicates using two different devices.

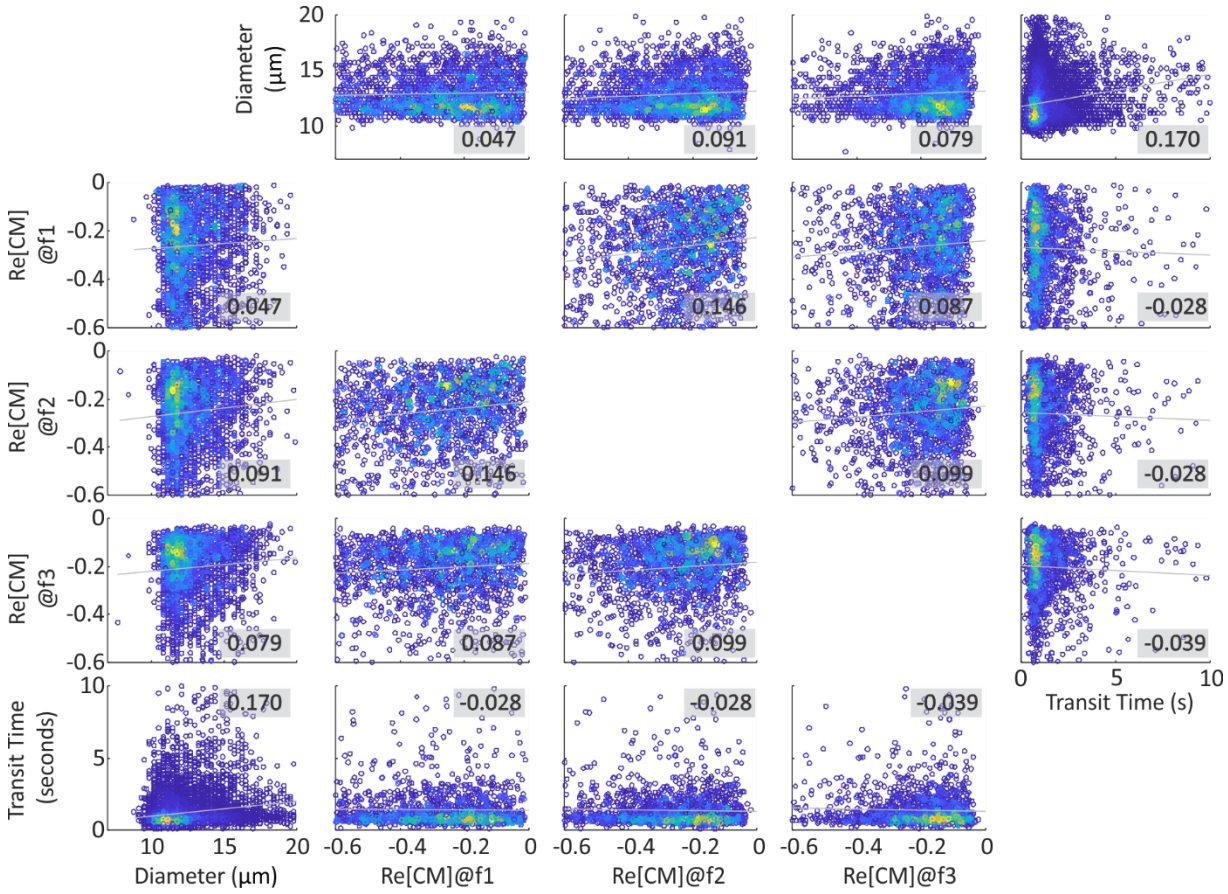

Figure 3-14. Correlation plots among pairs of intrinsic markers measured from the integrated platform. The density scatter plots show combined measurements of the three cell lines (HL60, Jurkat, and K562). The linear correlation coefficients and the corresponding least-squares reference lines are displayed.

The trained classifier was able to detect HL60, JURKAT, and K562 with 74.0%, 68.8%, and 76.5% accuracy, respectively. According to the area under the ROC curve (AUC) and the confusion matrix, the classifier was able to distinguish K562 from the other two cell lines with the highest discriminating capability, while it was more challenging to distinguish between HL60 and JURKAT. To evaluate the contribution of each intrinsic marker to the classification performance, we calculated predictor importance estimates by averaging the improvements in the splitting criterion due to splits on every predictor (Figure 3-15h). The results suggested that cell diameter

was the most important parameters that contributed to the overall classification accuracy between the three cell types.

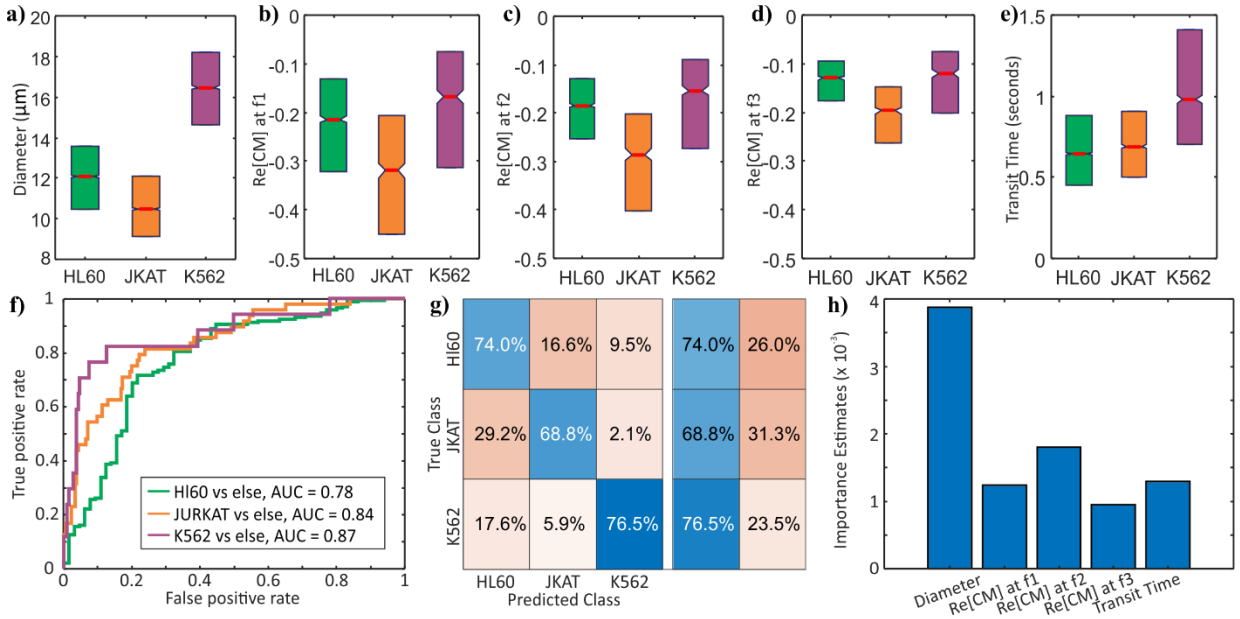

Figure 3-15. Multiparameter measurements and classification of three leukemia cell lines, including HL60, JURKAT, and K562. a) Diameter. b) Re[CM] at f1. c) Re[CM] at f2. d) Re[CM] at f3. e) Transit time. f) ROC curves and g) confusion matrix, illustrating the classifier's ability to distinguish between the three leukemia cell lines in the test dataset. h) Predictor importance estimates from the classifier.

3.4.6 Image Processing Time and Throughput Analysis

To analyze the image processing time and throughput, we introduced different concentrations of cells into the microfluidic platform (Figure 3-16) and estimated the image processing time and throughput as a function of cell concentrations (Figure 3-17). According to Figure 3-17a, the average pre-processing time and YOLO cell hologram detection time per frame are generally constant within the range of cell concentrations tested. However, the current size extraction algorithm, which involves image reconstruction, intensity thresholding, and connected component analysis, results in the average size extraction time that depends on the cell concentration. The recording time, illustrated as a red dashed line, shows that frames with fewer than ~200 cells can be processed faster or as fast as they were recorded. Figure 3-17b reports the final measurement throughput of the size, polarizability, and deformability modules separately. Throughput of the deformability module are 21% - 50% less than the throughput of size measurement, because a small number of cells went through the bypass channels instead of the constriction channels and a number of cell holograms near the narrowest constrictions were not detected. The throughput of

polarizability module is 15% - 40% of the size measurement throughput as some cells did not travel close the centerlines of the coplanar electrodes and did not experience sufficient negative DEP force for the polarizability measurements.

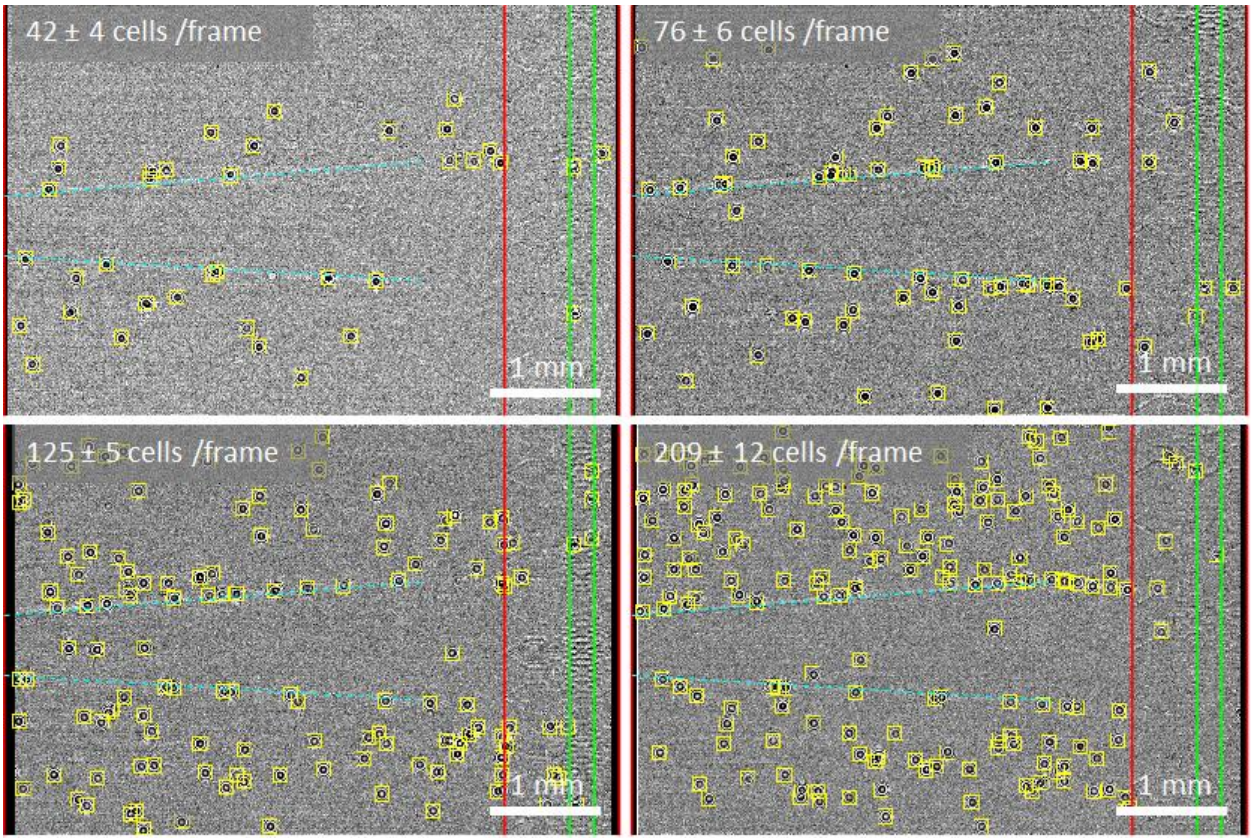

Figure 3-16. Snapshots of time-lapsed pre-processed holograms when various concentrations of cells ($1x10^5$ to $5x10^5$ cells/mL) were introduced into the microfluidic platform.

With our integrated image-based analytical system, we showed that more than hundreds of cells could be monitored simultaneously in an enlarged FOV of 21 mm^2 and an order of magnitude improvement in the final throughput could be achieved compared to our previous system.[193] While an FOV of 21 mm^2 was shown in the applications presented here, the digital holographic imaging system can be extended to ~cm^2 scale simply by replacing the CMOS sensor with an image sensor with a larger active area. For label-free biophysical assays, in particular, an increase in the imager's FOV enlarges the device probe area and enhances flexibility in the design of the microfluidic measurement platforms. An increase in the device probe area would allow parallelization and sequential stacking of the same or different types of the physical probes, which could be used to improve repeatability, throughput, sensitivity, and specificity of the measurements. Similarly, the

spatial resolution of the imaged-based measurements could be improved by replacing the CMOS image sensor with an imager with a smaller pixel size. An increase in the spatial resolution would improve the measurement accuracy and precision of all spatial parameters, as well as enhance their discriminating power.

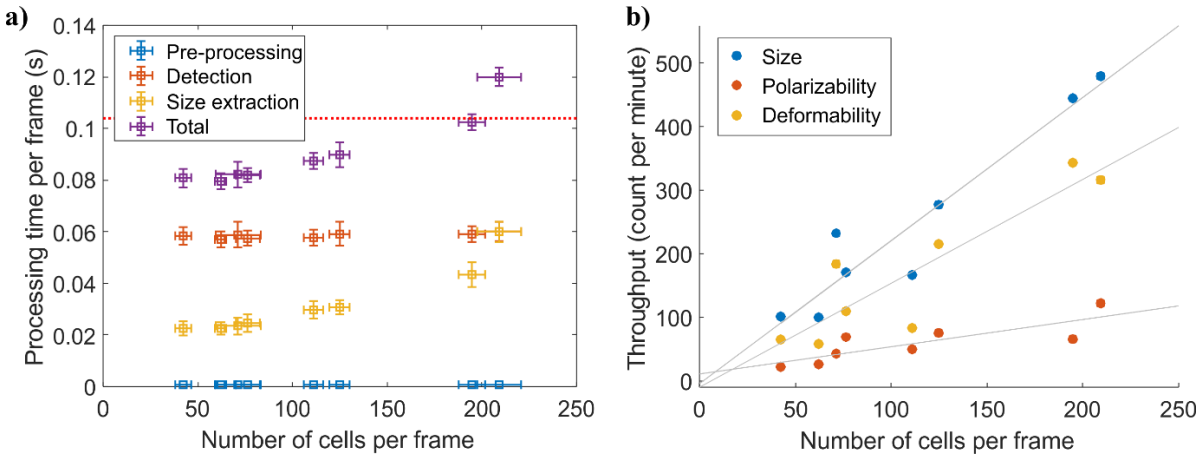

Figure 3-17. Image processing time and throughput versus cell concentrations estimated from the first two hundred frames of eight recorded experiment videos. a) Average processing time per frame for pre-processing, YOLO cell hologram detection, size extraction, and total time. The error bars depict the standard deviations. The red dashed line indicates the recording time per frame. Note that the average size extraction time was computed from applying size extraction every tenth frame. b) The final measurement throughput of each measurement modules, including size, polarizability, and deformability. The throughput in the polarizability module is calculated from the number of cell trajectories with at least one valid polarizability measurement. The grey lines show the least-square lines of throughput versus cell concentration for each module.

3.5 Conclusions

We developed an integrated image-based analytical platform with an enlarged FOV of ~21 mm^2 for real-time analysis of particle dynamics in microfluidic obstacles by using digital holographic imaging and deep learning. The integrated system was applied to an enlarged microfluidic platform that contained two pairs of electrodes for multi-frequency polarizability measurements and 72 parallel constriction channels for deformability measurements. The measurements of the five intrinsic markers obtained from the integrated system were validated with the measurements obtained from a Coulter Counter and a microscope imaging system. Multiparameter measurements and classification of three leukemia cell lines were performed to demonstrate the high-throughput applications of the integrated system.

Chapter 4

Contributions and Future Outlook

In this thesis, a new approach to multiparameter, cell-tracking, intrinsic cytometry platform for single-cell characterization has been conceptualized and developed by leveraging microfluidic technologies, imaging technologies, and computer vision. The specific instantiation of the cytometry platform, which can measure up to five intrinsic markers of cells, has been demonstrated for quantitative investigation of label-free cell profiles and applied for classification of cell types and functional states. The major contributions of this thesis and the potential future directions building upon this work are summarized below.

4.1 Contributions

A new approach to combine the measurement of more than two intrinsic properties of cells

We have developed a new approach to combine the label-free measurement of single cells' biophysical properties across domains (e.g., mechanical, electrical, optical) by utilizing microfluidic techniques to manipulate cells' spatiotemporal positions according to their biophysical properties; and by using image-based tracking to monitor, extract, and connect the measured properties to individual cells. This approach provides a versatile framework for integrating existing and future microfluidic measurement techniques across domains while mitigating the complications from combining different readout systems. In our approach, a number of microfluidic measurement modules can be used as building blocks to be added in parallel or sequentially within the two-dimensional active space of the analytical platform, and be independently optimized. Flexibility in the design space of the microfluidic platform and convenience in the readout system renders the approach readily extensible to investigate a myriad of promising intrinsic markers of single cells that are rarely studied together for explorative analysis, as well as readily customizable for specific biological and clinical applications.

Instantiation of a cell-tracking intrinsic cytometry that measures up to five intrinsic properties of single cells and affirms the utility of combining multiple intrinsic markers

We have implemented a cell-tracking intrinsic cytometry system that measures diameter, polarizability at three frequencies, and deformability of single cells; and, in effect, established a unique screening tool that allows the electrical and the mechanical phenotypes of cells to be measured and studied together at the single-cell level. The multidimensional biophysical profile of single cells, from three treatment conditions of a cytoskeletal drug, measured on our platform has enabled us to perform multivariate studies, including 1.) correlation tests to assess the linear

relationship between cell size, deformability and polarizability; 2.) unsupervised nonlinear dimensionality reduction visualization that illustrates the combined changes of the measured intrinsic markers as a result of different treatment conditions; and 3.) training and testing of supervised machine-learning classification models from subsets of the five measured markers to confirm the additional contribution of each marker to the classification accuracy of drug-induced structural changes in single cells. Using five measured intrinsic markers, we demonstrated that classification accuracy for three drug-induced cell states of ~71.4% could be achieved.

Enhancement of the image-based analytical system using digital holography and deep learning

We have developed an integrated image-based analytical platform with an enlarged FOV of ~21 mm^2 (which is ~ 4 times the FOV of 5X microscope objective and ~ 10 times the FOV of the 10X microscope objective) for real-time detection of particle dynamics in microfluidic obstacles, by using digital holographic imaging and deep learning. The integrated system was applied to monitor an enlarged microfluidic platform that contained two pairs of electrodes for multi-frequency polarizability measurements and 72 parallel constriction channels for deformability measurements. Large-FOV digital holographic microscopy is commonly applied to observe static samples, and moving samples in simple straight microfluidic channels or in large microfluidic chambers. Here, we have demonstrated that the presence of cells in microfluidic obstacles can be reliably and rapidly detected for extraction of their spatiotemporal positions via deep-learning based image analysis, even when their holographic patterns deviate substantially from the regular circular fringe patterns, e.g., the presence of a cell in 6-μm-wide parallel constriction channels (constriction width ~3-4 pixels in the hologram images) can still be detected.

In the context of cell-tracking intrinsic cytometry, the expansion of the imager's FOV and the microfluidic investigation area increases flexibility in the design space for addition and optimization of the microfluidic single-cell measurement modules. For example, the enlarged space can be designed to accommodate parallel single-cell measurement probes for increased throughout, or sequential stacks of new and repeated measurement modules for increased sensitivity and specificity. In our application, we expanded our previously reported cell-tracking intrinsic cytometry platform to accommodate two pairs of parallel electrodes for polarizability

measurement and 72 parallel constriction channels for deformability measurement, and observed more than a magnitude increase in throughput.

4.2 Future Directions

4.2.1 Technological Directions

Next-generation multiparameter cell-tracking intrinsic cytometry

To tackle important biological and biomedical challenges, the next-generation multiparameter cell-tracking intrinsic cytometry must be optimized in terms of sensitivity, specificity, and throughput. This can be achieved by optimizing each of the three subsystems in the cell-tracking intrinsic cytometry. First, the CMOS image sensor can be replaced by a high-speed image sensor with large active area and small pixel size, allowing dynamics of cells' positions and morphology to be recorded with high spatial resolution and high temporal resolution. Second, the label-free measurement modules in the microfluidic platform can be optimized. For example, they can be replaced with modules that are less sensitive to size, e.g., IDS for polarizability measurement and stacks of constriction obstacles with decreasing gap width for deformability measurement. Alternatively, deterministic lateral displacement array (DLD) can be used to separate cells according to size before cells are introduced to constrictions with corresponding widths. Other label-free measurement modules, e.g., cell rolling and acoustophoresis, can also be added to the platform to enable extraction of new intrinsic markers and increase the specificity in cell type classification. Measurement methods, that can be parallelized easily, can increase the throughput of the system significantly.

Deep-learning enabled image analysis

In the current system, we use deep learning models to enable rapid and accurate detection of moving cells in the microfluidic platform from hologram images. The cell centroids and cell diameters are later used to extract the five intrinsic markers for analysis. Nevertheless, there is a wealth of information in the cell holograms (e.g., morphological features, subcellular components, refractive indexes). While it is challenging to extract important image features when the differences are not obvious to human eyes, deep-learning models can be trained to extract useful hologram image features to combine with deformability, polarizability, and diameter for a more accurate cell identification and classification. This would give a unique screening tool that merges

the quantitative measurement of the optical phenotypes (that are beyond cell diameters) with the mechanical and the electrical phenotypes.

Integration of fluorescence measurements

In addition to intrinsic biophysical properties, the platform can be extended to concurrently measure multiple biochemical properties of single cells while they traverse the aforementioned microfluidic platform via fluorescent labels and wide-field fluorescence imaging built upon the computational imager. One approach using a multiband filter and serial switching between the digital holography channels and the fluorescence channels is illustrated in Figure 4-1. Measurements of the additional biochemical properties of single cells can be used to validate cell identification based on single-cell biophysical properties or consolidated with single-cell biophysical properties for improvement in cell classification, as shown in earlier works on microfluidic impedance and fluorescent flow cytometry.[200] More importantly, the correlation maps between multiple biophysical properties and one or more biochemical properties of single cells can be created for studies that were not possible without the single-cell association between intrinsic and extrinsic cellular properties. These studies can potentially lead to discovery of new cell subpopulations, development of new protocol for disease progression monitoring, and unravelling of molecular or biochemical underpinnings of biophysical properties.

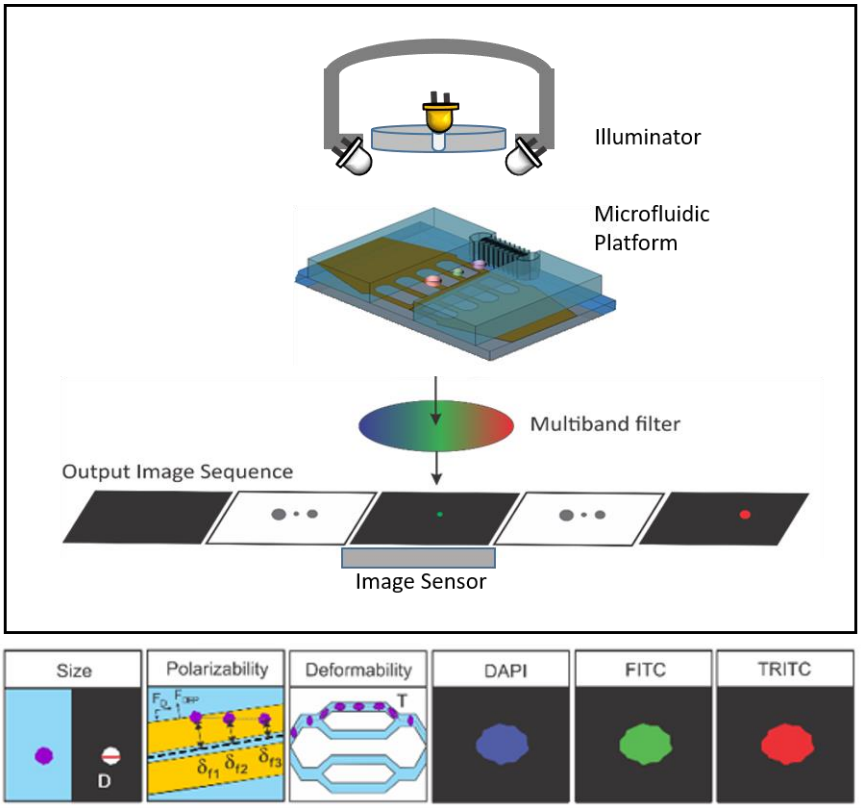

Figure 4-1. An approach to integrate fluorescence measurements with the cell-tracking intrinsic cytometry, which allows biophysical and biochemical phenotyping of single cells.

4.2.2 Biological directions

Optical, mechanical, and electrical phenotypes of cells have each been investigated for numerous applications which often overlap, e.g., leukocyte activation, infection of red blood cells, early detection of apoptosis, and lineage potential of stem cells. The multiparameter cell-tracking intrinsic cytometry can be used to screen the biophysical properties of these samples at the single-cell level and create holistic biophysical profiles of cells to answer important biological and biomedical questions. Interesting questions, that can be answered using our platform, include 1.) how the measured intrinsic markers are related to each other, 2.) how and when certain changes (e.g., biochemical, genetic) in the cells are accompanied by changes in the measured intrinsic markers, and 3.) if their combined discrimination capability can be used to substitute or complement an extrinsic marker.

Appendix

Appendix 1 Fabrication process of the microfluidic channels with SU-8, using a mask aligner

Starting Materials:
150-mm-diameter, 650-μm-thick Silicon wafers (WaferNet, Inc., San Jose, CA)

Photomask: Front Range Photomask, 7"x7", .12" thick (~3.05mm)

Step	Description	Machine	Parameters
0	Dehydration bake	Hotplate 300	200°C, 30 min
1	Adhesion Layer	SU-8 spinner	SU-8 2002(2 μm thickness), Dispense ~6ml SU-8 (1ml per inch diameter) Ramp to 3000 rpm and hold for total of 30 seconds
		Hotplate 2 (95°C)	Hold at 95°C for 1 min; cool to ambient
		EV1	Flood exposure for 10 seconds
		Hotplate 2 (95°C)	Hold at 95°C for 2 min; cool to ambient
2	SU-8 Spin	SU-8 spinner	SU-8 2015(20 μm thickness): Dispense ~6ml SU-8 Ramp to 500 rpm at 100 rpm/sec acceleration and hold for 5-10 seconds Ramp to 2250 rpm at 300 rpm/second and hold for total of 30 seconds
3	Prebake	Hotplate station	Slow ramp from 60°C to 95°C, hold at 95°C for 4 min; cool to ambient
4	UV expose	EV1	Flow chamber mask, 10 seconds. 30 μm separation
5	Post-expose bake	Hotplate station	Slow ramp from 60°C to 95°C, hold at 95°C for 5 min; cool to ambient
6	Develop	SU-8 hood	~ 3-5 min soak in PM Acetate from Pass-Thru Spray with PMA and IPA Dry with Nitrogen gun

Facility: Voldman Group Lab

7	Hard bake	Hotplate 150^{o}C	Leave the SU-8 in the hotplate for ~ 30 minutes up to 2 hours. The purpose is to make remaining solvent evaporates.
8	Silanize	Acid/Base Hood	Put 3-4 drops of trichloro octadecyl silane into aluminum foil cup in vacuum jar. Put wafer in wafer holder in the jar Close jar, turn on vacuum for 5-10 min Turn vacuum off, let it sit for ~ 30 min

9	Mix and degas PDMS		Weigh the PDMS (Polydimethylsiloxane, Sylgard 184) pre-polymer components in a 10:1 ratio. Mix well. Utilize approximately 70 grams of the PDMS. Degas under vacuum (desiccator) until no bubbles appear in the mixture (20~30 minutes). Make sure the PDMS mixture does not foam out of the container.
10	Pour PDMS		Place the SU-8 master wafer into aluminum foil. Carefully pour the PDMS into the foil to minimize bubbles.
11	Cure PDMS		Cure the PDMS on a hotplate at 80^{o}C for 2 hours. After curing, the wafer with the PDMS is stable and may be stored for months.
12	Remove the mold		Carefully peel off the PDMS mold from the SU-8 master, and cut out individual devices with a razor.

Appendix 2 Fabrication process for electrode patterning on Pyrex, using a mask aligner

Starting Materials:

150-mm-diameter, 762-μm-thick Pyrex wafers (Bullen Ultrasonics, Eaton, OH)

Step	Description	TRL Machine	Parameters
Electrode patterning, 6" Pyrex wafer			
1	Piranha clean	Acid hood	
2	Dehydration bake	HMDS oven	HDMS recipe for AZ5214, 155°C, 30 mins, wait for air cool
3	Photolithography	Spin Coater Prebake Oven EV1 Postbake Oven EV1 Hood	Coater: DISPENSE: 500;8s SPREAD: 750rpm;6s; SPIN: 2000rpm; 30s (2um) Prebake for 30mins Expose 2sec with masks 90secs on 120 hotplate (or in postbake oven) flood exposure 70 seconds (w/o mask) develop in AZ422 (90sec)
4	Metal evaporation	eBeamFP	100Å Ti, 2000Å Au
5	Liftoff metal	Solvent-Au	Liftoff with acetone
6	Protective resist coat	Coater	AZ 5214, 500 rpm final speed
7	Bake	Hotplate station	120°C, 2 min

Appendix 2 Fabrication process for electrode patterning on ITO coated glass slides, using a maskless aligner

Starting Materials: (1200 - 1600 A)-thick ITO coated glass slides (75mm-by-25mm-by-0.7mm)

Step	Description	TRL Machine	Parameters
0	Clean ITO glass	Photo-wet	Clean with Acetone, Isopropanol, Methanol
1	Dehydration bake	Hot plate	Dehydration bake at 110^{o}C for 10 minutes
2	Photoresist spin coat	coater	Target thickness (1 um): Dispense SPR700 on substrate Ramp to 3000 rpm and hold for total of 30 seconds
3	Soft bake	Hot plate	At 110^{o}C for 5 minutes
4	Direct write	MLA150	Direct write with i-line(365nm)
5	Post exposure bake	Hot plate	At 115^{o}C for 1 minutes
6	Photoresist develop	Photo-wet	Immerse in CD26 for 30 seconds (visual stop) Rinse with DI water Blow dry
7	Hard bake	Hot plate	At 130^{o}C for 3 minutes
8	ITO etching	Acid-hood2	Prepare etching solution: HCL: $H_2$0: HNO_3 = 4: 2: 1 by volume Immerse for 3 minutes at room temperature Rinse with DI water for 4 cycles Blow dry Dehydration bake at 105^{o}C for 15 minutes
9	Photoresist removal	Photo-wet	Immerse in Acetone for 1 minute with ultrasound on and then Isopropanol (IPA) for 1 minutes with ultrasound on. Rinse with DI water for 4 cycles Blow dry Dehydration bake at 105^{o}C for 15 minutes

Appendix 4: Experiment Protocol

Materials:

1. Assembled device
2. 3 ml, 5 ml, and 10 ml plastic syringes (Becton, Dickinson and Company)
3. 1 mL plastic syringes (Becton, Dickinson and Company)
4. Tubing (Tygon®, 0.020-inch inner diameter)
5. Five 25 mm syringe filters (Pall Corporation, 0.2 µm Tuffryn® membrane)
6. Solution of polystyrene microspheres or cells

Sample preparation

- Microsphere sample
  1. Dispense 100 µL bead solution from bottle into a 1 mL Eppendorf with 900 µL of 0.1% tween® 20 DPBS solution. Keep track of bead concentration. The proportion of beads to buffer can be adjusted according to bottle concentration. Vortex bead container before dispensing.
  2. Centrifuge the Eppendorf according to bead size.

Bead Diameter (µm)	G – Force (cm/s^2)	Time (minutes)
4.5	594	2
6	334	2
10	120	2
15	53	2

  3. Carefully drain the liquid until only the beads are left in the bottom.
  4. Dispense 1 mL filtered DPBS-T into the Eppendorf. Vortex.
  5. Dilute the washed solution to the final concentration of 10^5 to 10^6 particles/ml.
  6. Take 100 µL out for coulter counter analysis.
- Cell sample
  1. Load cells suspended in cell culture media into a 15 mL Falcon tube.
  2. Centrifuge at 1500 rpm for five minutes.
  3. Gently drain the media out of the Falcon tube without discarding the cells.
  4. Dispense 1 mL of 13.3% Dextran in DPBS and mix with cells by gentle pipetting.
  5. Filter the cell sample by pipetting it through a cell strainer.
  6. Take 100 µL out for coulter counter analysis.

Device Pre-conditioning:

1. Position and secure the device under the microscope (Zeiss Axio Imager M1M) equipped with a 12-bit CCD camera (LA Vision Imager QE)
2. Load a 10 mL syringe with 0.5% Pluronic F108 in deionized water. Connect it to a filter, tubing, and metal inserts. Clamp it into place on a syringe pump.
3. Let the pump run at 5-10 µL/min until you see droplets forming at the ends of the tubing. Plug the tubing into outlets of the device, merging the droplets from the tube with droplets over the outlets.

4. Observe. Increase the flow rate for faster bubble elimination. Let the priming solution fill inside the device and disconnect the tubing when all bubbles are removed (~ 10-20 minutes)
5. Load a syringe with 7.5% BSA and connect it to the device. Let the priming solution fill inside the device and wait for at least 30 minutes. Disconnect the tubing.

Device Set-up:

1. Load sample into a 1 mL syringe and load filtered DPBS into 5 mL syringes. Connect to filters (only the DPBS syringes), and tubing. Clamp them on syringe pumps.
2. Let the pump run at 5-10 µL/min until you see droplets forming at the ends of the tubing. Stop the pump. Connect the tubing to the inlets of the device, merging the droplets from the tube with droplets over the inlets.
3. Run the syringe pumps. Set the sample syringe pump such the syringe is vertically pointing the ground. Observe and adjust flow rates if needed.

Clean-up:

1. When the experiment is finished, disconnect the syringes from the device.
2. Flush out the plastic syringes a few times before throwing them away.

References

1. Suresh, S. Biomechanics and biophysics of cancer cells☆. *Acta Biomaterialia* **3**, 413–438 (2007).
2. Zheng, Y., Nguyen, J., Wei, Y. & Sun, Y. Recent advances in microfluidic techniques for single-cell biophysical characterization. *Lab on a Chip* **13**, 2464–2483 (2013).
3. Nair, A., Chauhan, P., Saha, B. & Kubatzky, K. F. Conceptual Evolution of Cell Signaling. *International Journal of Molecular Sciences* **20**, 3292 (2019).
4. Yusko, E. C. & Asbury, C. L. Force is a signal that cells cannot ignore. *MBoC* **25**, 3717–3725 (2014).
5. Wouters, F. S., Verveer, P. J. & Bastiaens, P. I. H. Imaging biochemistry inside cells. *Trends in Cell Biology* **11**, 203–211 (2001).
6. Chattopadhyay, P. K., Hogerkorp, C.-M. & Roederer, M. A chromatic explosion: the development and future of multiparameter flow cytometry. *Immunology* **125**, 441–449 (2008).
7. Bandura, D. R. *et al.* Mass Cytometry: Technique for Real Time Single Cell Multitarget Immunoassay Based on Inductively Coupled Plasma Time-of-Flight Mass Spectrometry. *Anal. Chem.* **81**, 6813–6822 (2009).
8. Spitzer, M. H. & Nolan, G. P. Mass Cytometry: Single Cells, Many Features. *Cell* **165**, 780–791 (2016).
9. Adan, A., Alizada, G., Kiraz, Y., Baran, Y. & Nalbant, A. Flow cytometry: basic principles and applications. *Critical Reviews in Biotechnology* **37**, 163–176 (2017).
10. Brown, M. & Wittwer, C. Flow Cytometry: Principles and Clinical Applications in Hematology. *Clin Chem* **46**, 1221–1229 (2000).
11. Ding, M., Kaspersson, K., Murray, D. & Bardelle, C. High-throughput flow cytometry for drug discovery: principles, applications, and case studies. *Drug Discovery Today* **22**, 1844–1850 (2017).
12. Darling, E. M. & Di Carlo, D. High-Throughput Assessment of Cellular Mechanical Properties. *Annual Review of Biomedical Engineering* **17**, 35–62 (2015).
13. Di Carlo, D. A Mechanical Biomarker of Cell State in Medicine. *J Lab Autom.* **17**, 32–42 (2012).
14. Chen, J. *et al.* Microfluidic Impedance Flow Cytometry Enabling High-Throughput Single-Cell Electrical Property Characterization. *International Journal of Molecular Sciences* **16**, 9804–9830 (2015).
15. Van Vliet, K. J., Bao, G. & Suresh, S. The biomechanics toolbox: experimental approaches for living cells and biomolecules. *Acta Materialia* **51**, 5881–5905 (2003).
16. Gossett, D. R. *et al.* Label-free cell separation and sorting in microfluidic systems. *Anal Bioanal Chem* **397**, 3249–3267 (2010).
17. Carey, T. R., Cotner, K. L., Li, B. & Sohn, L. L. Developments in label-free microfluidic methods for single-cell analysis and sorting. *Wiley Interdisciplinary Reviews: Nanomedicine and Nanobiotechnology* **11**, e1529 (2019).
18. Sun, G. & Lu, H. Recent Advances in Microfluidic Techniques for Systems Biology. *Anal. Chem.* **91**, 315–329 (2019).
19. Moeendarbary, E. & Harris, A. R. Cell mechanics: principles, practices, and prospects. *WIREs Systems Biology and Medicine* **6**, 371–388 (2014).
20. Lee, G. Y. H. & Lim, C. T. Biomechanics approaches to studying human diseases. *Trends in Biotechnology* **25**, 111–118 (2007).

21. Mierke, C. T. The fundamental role of mechanical properties in the progression of cancer disease and inflammation. *Rep. Prog. Phys.* **77**, 076602 (2014).
22. Nematbakhsh, Y. & Lim, C. T. Cell biomechanics and its applications in human disease diagnosis. *Acta Mech Sin* **31**, 268–273 (2015).
23. Shelby, J. P., White, J., Ganesan, K., Rathod, P. K. & Chiu, D. T. A microfluidic model for single-cell capillary obstruction by Plasmodium falciparum-infected erythrocytes. *PNAS* **100**, 14618–14622 (2003).
24. Bow, H. *et al.* A microfabricated deformability-based flow cytometer with application to malaria. *Lab Chip* **11**, 1065–1073 (2011).
25. J. Rosenbluth, M., A. Lam, W. & A. Fletcher, D. Analyzing cell mechanics in hematologic diseases with microfluidic biophysical flow cytometry. *Lab on a Chip* **8**, 1062–1070 (2008).
26. Hou, H. W. *et al.* Deformability study of breast cancer cells using microfluidics. *Biomed Microdevices* **11**, 557–564 (2009).
27. Byun, S. *et al.* Characterizing deformability and surface friction of cancer cells. *Proceedings of the National Academy of Sciences* **110**, 7580–7585 (2013).
28. Adamo, A. *et al.* Microfluidics-Based Assessment of Cell Deformability. *Anal. Chem.* **84**, 6438–6443 (2012).
29. Zheng, Y., Shojaei-Baghini, E., Azad, A., Wang, C. & Sun, Y. High-throughput biophysical measurement of human red blood cells. *Lab on a Chip* **12**, 2560–2567 (2012).
30. Guan, G. *et al.* Real-time control of a microfluidic channel for size-independent deformability cytometry. *J. Micromech. Microeng.* **22**, 105037 (2012).
31. Forsyth, A. M., Wan, J., Ristenpart, W. D. & Stone, H. A. The dynamic behavior of chemically 'stiffened' red blood cells in microchannel flows. *Microvasc. Res.* **80**, 37–43 (2010).
32. Mietke, A. *et al.* Real-time deformability cytometry: on-the-fly cell mechanical phenotyping. *Nature Methods* **12**, 199 (2015).
33. Gossett, D. R. *et al.* Hydrodynamic stretching of single cells for large population mechanical phenotyping. *PNAS* **109**, 7630–7635 (2012).
34. Guck, J. *et al.* The Optical Stretcher: A Novel Laser Tool to Micromanipulate Cells. *Biophysical Journal* **81**, 767–784 (2001).
35. Guck, J. *et al.* Optical Deformability as an Inherent Cell Marker for Testing Malignant Transformation and Metastatic Competence. *Biophysical Journal* **88**, 3689–3698 (2005).
36. Ekpenyong, A. E. *et al.* Viscoelastic Properties of Differentiating Blood Cells Are Fate- and Function-Dependent. *PLoS One* **7**, (2012).
37. Sawetzki, T., Eggleton, C. D., Desai, S. A. & Marr, D. W. M. Viscoelasticity as a biomarker for high-throughput flow cytometry. *Biophys. J.* **105**, 2281–2288 (2013).
38. Chen, J. *et al.* Electrodeformation for single cell mechanical characterization. *J. Micromech. Microeng.* **21**, 054012 (2011).
39. Doh, I., Lee, W. C., Cho, Y.-H., Pisano, A. P. & Kuypers, F. A. Deformation measurement of individual cells in large populations using a single-cell microchamber array chip. *Appl Phys Lett* **100**, 173702-173702–3 (2012).
40. Du, E., Dao, M. & Suresh, S. Quantitative Biomechanics of Healthy and Diseased Human Red Blood Cells using Dielectrophoresis in a Microfluidic System. *Extreme Mech Lett* **1**, 35–41 (2014).

41. Leung, S. L., Lu, Y., Bluestein, D. & Slepian, M. J. Dielectrophoresis-Mediated Electrodeformation as a Means of Determining Individual Platelet Stiffness. *Ann Biomed Eng* **44**, 903–913 (2016).
42. Qiang, Y., Liu, J., Yang, F., Dieujuste, D. & Du, E. Modeling erythrocyte electrodeformation in response to amplitude modulated electric waveforms. *Scientific Reports* **8**, 1–10 (2018).
43. Teng, Y., Zhu, K., Xiong, C. & Huang, J. Electrodeformation-Based Biomechanical Chip for Quantifying Global Viscoelasticity of Cancer Cells Regulated by Cell Cycle. *Anal. Chem.* **90**, 8370–8378 (2018).
44. Voldman, J. Electrical Forces for Microscale Cell Manipulation. *Annual Review of Biomedical Engineering* **8**, 425–454 (2006).
45. Schwan, H. P. Electrode Polarization Impedance and Measurements in Biological Materials*. *Annals of the New York Academy of Sciences* **148**, 191–209 (1968).
46. Schwan, H. P. Electrical properties of tissues and cell suspensions: mechanisms and models. in *Proceedings of 16th Annual International Conference of the IEEE Engineering in Medicine and Biology Society* vol. 1 A70-A71 vol.1 (1994).
47. Wang, X. B. *et al.* Changes in Friend murine erythroleukaemia cell membranes during induced differentiation determined by electrorotation. *Biochim. Biophys. Acta* **1193**, 330–344 (1994).
48. Yang, J. *et al.* Dielectric Properties of Human Leukocyte Subpopulations Determined by Electrorotation as a Cell Separation Criterion. *Biophysical Journal* **76**, 3307–3314 (1999).
49. Zimmermann, D. *et al.* Effects on capacitance by overexpression of membrane proteins. *Biochem. Biophys. Res. Commun.* **369**, 1022–1026 (2008).
50. Huang, Y., Wang, X.-B., Holzel, R., Becker, F. F. & Gascoyne, P. R. C. Electrorotational studies of the cytoplasmic dielectric properties of Friend murine erythroleukaemia cells. *Phys. Med. Biol.* **40**, 1789–1806 (1995).
51. Duncan, L. *et al.* Dielectrophoretic analysis of changes in cytoplasmic ion levels due to ion channel blocker action reveals underlying differences between drug-sensitive and multidrug-resistant leukaemic cells. *Phys. Med. Biol.* **53**, N1–N7 (2007).
52. COULTER, W. H. High speed automatic blood cell counter and cell size analyzer. *Proceedings of the National Electronics Conference, 1956* **12**, 1034 (1956).
53. Gawad, S., Schild, L. & Renaud, P. Micromachined impedance spectroscopy flow cytometer for cell analysis and particle sizing. *Lab on a Chip* **1**, 76–82 (2001).
54. Sun, T. & Morgan, H. Single-cell microfluidic impedance cytometry: a review. *Microfluid Nanofluid* **8**, 423–443 (2010).
55. Jang, L.-S. & Wang, M.-H. Microfluidic device for cell capture and impedance measurement. *Biomed Microdevices* **9**, 737–743 (2007).
56. Malleo, D., Nevill, J. T., Lee, L. P. & Morgan, H. Continuous differential impedance spectroscopy of single cells. *Microfluid Nanofluid* **9**, 191–198 (2010).
57. James, C. D. *et al.* Impedimetric and optical interrogation of single cells in a microfluidic device for real-time viability and chemical response assessment. *Biosensors and Bioelectronics* **23**, 845–851 (2008).
58. Chen, N.-C., Chen, C.-H., Chen, M.-K., Jang, L.-S. & Wang, M.-H. Single-cell trapping and impedance measurement utilizing dielectrophoresis in a parallel-plate microfluidic device. *Sensors and Actuators B: Chemical* **190**, 570–577 (2014).

59. Asphahani, F. *et al.* Single-cell bioelectrical impedance platform for monitoring cellular response to drug treatment. *Phys. Biol.* **8**, 015006 (2011).
60. Sun, T., Green, N. G., Gawad, S. & Morgan, H. Analytical electric field and sensitivity analysis for two microfluidic impedance cytometer designs. *IET Nanobiotechnology* **1**, 69–79 (2007).
61. Cheung, K., Gawad, S. & Renaud, P. Impedance spectroscopy flow cytometry: On-chip label-free cell differentiation. *Cytometry* **65A**, 124–132 (2005).
62. Gou, H.-L. *et al.* Label-free electrical discrimination of cells at normal, apoptotic and necrotic status with a microfluidic device. *Journal of Chromatography A* **1218**, 5725–5729 (2011).
63. Bernabini, C., Holmes, D. & Morgan, H. Micro-impedance cytometry for detection and analysis of micron-sized particles and bacteria. *Lab on a Chip* **11**, 407–412 (2011).
64. Sun, T., Holmes, D., Gawad, S., Green, N. G. & Morgan, H. High speed multi-frequency impedance analysis of single particles in a microfluidic cytometer using maximum length sequences. *Lab Chip* **7**, 1034–1040 (2007).
65. Chen, J. *et al.* Classification of cell types using a microfluidic device for mechanical and electrical measurement on single cells. *Lab on a Chip* **11**, 3174–3181 (2011).
66. Zhao, Y. *et al.* Tumor cell characterization and classification based on cellular specific membrane capacitance and cytoplasm conductivity. *Biosensors and Bioelectronics* **57**, 245–253 (2014).
67. Luo, Y. N. *et al.* A constriction channel based microfluidic system enabling continuous characterization of cellular instantaneous Young's modulus. *Sensors and Actuators B: Chemical* **202**, 1183–1189 (2014).
68. Song, H. *et al.* A microfluidic impedance flow cytometer for identification of differentiation state of stem cells. *Lab on a Chip* **13**, 2300–2310 (2013).
69. Pethig, R. & Talary, M. S. Dielectrophoretic detection of membrane morphology changes in Jurkat T-cells undergoing etoposide-induced apoptosis. *IET Nanobiotechnology* **1**, 2–9 (2007).
70. Zhou, T., Ming, Y., Perry, S. F. & Tatic-Lucic, S. Estimation of the physical properties of neurons and glial cells using dielectrophoresis crossover frequency. *J Biol Phys* **42**, 571–586 (2016).
71. Labeed, F. H. *et al.* Biophysical Characteristics Reveal Neural Stem Cell Differentiation Potential. *PLoS One* **6**, (2011).
72. Huang, Y., Wang, X. B., Becker, F. F. & Gascoyne, P. R. Introducing dielectrophoresis as a new force field for field-flow fractionation. *Biophysical Journal* **73**, 1118–1129 (1997).
73. Markx, G. H., Rousselet, J. & Pethig, R. DEP-FFF: Field-Flow Fractionation Using Non-Uniform Electric Fields. *Journal of Liquid Chromatography & Related Technologies* **20**, 2857–2872 (1997).
74. Wang, X.-B. *et al.* Cell Separation by Dielectrophoretic Field-flow-fractionation. *Anal Chem* **72**, 832–839 (2000).
75. Poklepovic, A., Davis, D., Melnikova, V. & Anderes, K. 439 Comparison of Dielectrophoretic Field Flow Fractionation (DEP-FFF) with ApoStream™, an Antibody Independent Platform, with Immunomagnetic Capture Using CellSearch™ for Enumeration of Circulating Tumor Cells in Patients with Metastatic Prostate Cancer. *European Journal of Cancer* **48**, 136 (2012).

76. Lee, D., Hwang, B. & Kim, B. The potential of a dielectrophoresis activated cell sorter (DACS) as a next generation cell sorter. *Micro and Nano Syst Lett* **4**, 2 (2016).
77. Vahey, M. D. & Voldman, J. An equilibrium method for continuous-flow cell sorting using dielectrophoresis. *Anal. Chem.* **80**, 3135–3143 (2008).
78. Vahey, M. D. & Voldman, J. High-throughput cell and particle characterization using isodielectric separation. *Anal. Chem.* **81**, 2446–2455 (2009).
79. L. Prieto, J. *et al.* Monitoring sepsis using electrical cell profiling. *Lab on a Chip* **16**, 4333–4340 (2016).
80. Jundi, B. *et al.* Leukocyte function assessed via serial microlitre sampling of peripheral blood from sepsis patients correlates with disease severity. *Nature Biomedical Engineering* **3**, 961–973 (2019).
81. Su, H.-W., L. Prieto, J. & Voldman, J. Rapid dielectrophoretic characterization of single cells using the dielectrophoretic spring. *Lab on a Chip* **13**, 4109–4117 (2013).
82. Jaffe, A. & Voldman, J. Multi-frequency dielectrophoretic characterization of single cells. *Microsystems & Nanoengineering* **4**, 23 (2018).
83. Morgan, H., Sun, T., Holmes, D., Gawad, S. & Green, N. G. Single cell dielectric spectroscopy. *J. Phys. D: Appl. Phys.* **40**, 61 (2007).
84. Keim, K. *et al.* On-chip technology for single-cell arraying, electrorotation-based analysis and selective release. *Electrophoresis* **40**, 1830–1838 (2019).
85. Marina, O. C., Sanders, C. K. & Mourant, J. R. Correlating light scattering with internal cellular structures. *Biomed Opt Express* **3**, 296–312 (2012).
86. Liu, P. Y. *et al.* Cell refractive index for cell biology and disease diagnosis: past, present and future. *Lab Chip* **16**, 634–644 (2016).
87. Zhou, Q. & Kim, T. Review of microfluidic approaches for surface-enhanced Raman scattering. *Sensors and Actuators B: Chemical* **227**, 504–514 (2016).
88. Vembadi, A., Menachery, A. & Qasaimeh, M. A. Cell Cytometry: Review and Perspective on Biotechnological Advances. *Front. Bioeng. Biotechnol.* **7**, (2019).
89. Chen, C. L. *et al.* Deep Learning in Label-free Cell Classification. *Scientific Reports* **6**, 21471 (2016).
90. Li, Y. *et al.* Deep Cytometry: Deep learning with Real-time Inference in Cell Sorting and Flow Cytometry. *Scientific Reports* **9**, 1–12 (2019).
91. Stavrakis, S., Holzner, G., Choo, J. & deMello, A. High-throughput microfluidic imaging flow cytometry. *Current Opinion in Biotechnology* **55**, 36–43 (2019).
92. Chen, H.-T., Fu, L.-M., Huang, H.-H., Shu, W.-E. & Wang, Y.-N. Particles small angle forward-scattered light measurement based on photovoltaic cell microflow cytometer. *ELECTROPHORESIS* **35**, 337–344 (2014).
93. Fu, L.-M. & Wang, Y.-N. Optical microflow cytometer based on external total reflection. *ELECTROPHORESIS* **33**, 3229–3235 (2012).
94. Dannhauser, D. *et al.* Optical signature of erythrocytes by light scattering in microfluidic flows. *Lab Chip* **15**, 3278–3285 (2015).
95. Blasi, T. *et al.* Label-free cell cycle analysis for high-throughput imaging flow cytometry. *Nature Communications* **7**, 10256 (2016).
96. Headland, S. E., Jones, H. R., D'Sa, A. S. V., Perretti, M. & Norling, L. V. Cutting-Edge Analysis of Extracellular Microparticles using ImageStream X Imaging Flow Cytometry. *Scientific Reports* **4**, 1–10 (2014).

97. Eulenberg, P. *et al.* Reconstructing cell cycle and disease progression using deep learning. *Nature Communications* **8**, 463 (2017).
98. Doan, M. *et al.* Label-free assessment of red blood cell storage lesions by deep learning. *bioRxiv* 256180 (2018) doi:10.1101/256180.
99. Claire Hur, S., Kwong Tse, H. T. & Carlo, D. D. Sheathless inertial cell ordering for extreme throughput flow cytometry. *Lab on a Chip* **10**, 274–280 (2010).
100. Schonbrun, E., Gorthi, S. S. & Schaak, D. Microfabricated multiple field of view imaging flow cytometry. *Lab Chip* **12**, 268–273 (2011).
101. Rane, A. S., Rutkauskaite, J., deMello, A. & Stavrakis, S. High-Throughput Multi-parametric Imaging Flow Cytometry. *Chem* **3**, 588–602 (2017).
102. Seo, S. *et al.* High-Throughput Lens-Free Blood Analysis on a Chip. *Anal. Chem.* **82**, 4621–4627 (2010).
103. Goda, K. *et al.* High-throughput single-microparticle imaging flow analyzer. *PNAS* **109**, 11630–11635 (2012).
104. Tang, A. H. L. *et al.* Microfluidic Imaging Flow Cytometry by Asymmetric-detection Time-stretch Optical Microscopy (ATOM). *J Vis Exp* (2017) doi:10.3791/55840.
105. Xavier, M. *et al.* Mechanical phenotyping of primary human skeletal stem cells in heterogeneous populations by real-time deformability cytometry. *Integrative Biology* **8**, 616–623 (2016).
106. Sajeesh, P., Raj, A., Doble, M. & Sen, A. K. Characterization and sorting of cells based on stiffness contrast in a microfluidic channel. *RSC Adv.* **6**, 74704–74714 (2016).
107. Zheng, Y., Nguyen, J., Wang, C. & Sun, Y. Electrical measurement of red blood cell deformability on a microfluidic device. *Lab on a Chip* **13**, 3275–3283 (2013).
108. Nyberg, K. D. *et al.* The physical origins of transit time measurements for rapid, single cell mechanotyping. *Lab Chip* **16**, 3330–3339 (2016).
109. Holmes, D. *et al.* Leukocyte analysis and differentiation using high speed microfluidic single cell impedance cytometry. *Lab on a Chip* **9**, 2881–2889 (2009).
110. Carlo, D. D. *et al.* High-throughput physical phenotyping of cell differentiation. *Microsystems & Nanoengineering* **3**, 17013 (2017).
111. Yang, D., Zhou, Y., Zhou, Y., Han, J. & Ai, Y. Biophysical phenotyping of single cells using a differential multiconstriction microfluidic device with self-aligned 3D electrodes. *Biosensors and Bioelectronics* **133**, 16–23 (2019).
112. Love, J. C., Roederer, M., Chattopadhyay, P. K. & Gierahn, T. M. Single-cell technologies for monitoring immune systems. *Nature Immunology* **15**, 128 (2014).
113. Bendall, S. C. *et al.* Single-Cell Mass Cytometry of Differential Immune and Drug Responses Across a Human Hematopoietic Continuum. *Science* **332**, 687–696 (2011).
114. Ornatsky, O. *et al.* Highly multiparametric analysis by mass cytometry. *Journal of Immunological Methods* **361**, 1–20 (2010).
115. Suresh, S. *et al.* Connections between single-cell biomechanics and human disease states: gastrointestinal cancer and malaria. *Acta Biomaterialia* **1**, 15–30 (2005).
116. Suresh, S. Mechanical response of human red blood cells in health and disease: Some structure-property-function relationships. *Journal of Materials Research* **21**, 1871–1877 (2006).
117. Kim, D.-H., Wong, P. K., Park, J., Levchenko, A. & Sun, Y. Microengineered Platforms for Cell Mechanobiology. *Annual Review of Biomedical Engineering* **11**, 203–233 (2009).

118. Diez-Silva, M., Dao, M., Han, J., Lim, C.-T. & Suresh, S. Shape and Biomechanical Characteristics of Human Red Blood Cells in Health and Disease. *MRS Bulletin* **35**, 382–388 (2010).
119. Zheng, Y. & Sun, Y. Microfluidic devices for mechanical characterisation of single cells in suspension. *IET Micro Nano Letters* **6**, 327–331 (2011).
120. Mao, X. & Jun Huang, T. Exploiting mechanical biomarkers in microfluidics. *Lab on a Chip* **12**, 4006–4009 (2012).
121. Lenshof, A. & Laurell, T. Continuous separation of cells and particles in microfluidic systems. *Chemical Society Reviews* **39**, 1203–1217 (2010).
122. Chen, J., Li, J. & Sun, Y. Microfluidic approaches for cancer cell detection, characterization, and separation. *Lab on a Chip* **12**, 1753–1767 (2012).
123. Iv, C. W. S., D. Reyes, C. & P. López, G. Microfluidic cell sorting: a review of the advances in the separation of cells from debulking to rare cell isolation. *Lab on a Chip* **15**, 1230–1249 (2015).
124. Autebert, J. *et al.* Microfluidic: An innovative tool for efficient cell sorting. *Methods* **57**, 297–307 (2012).
125. Bhagat, A. A. S. *et al.* Microfluidics for cell separation. *Med Biol Eng Comput* **48**, 999–1014 (2010).
126. Park, E. S. *et al.* Continuous Flow Deformability-Based Separation of Circulating Tumor Cells Using Microfluidic Ratchets. *Small* **12**, 1909–1919 (2016).
127. Tse, H. T. K. *et al.* Quantitative Diagnosis of Malignant Pleural Effusions by Single-Cell Mechanophenotyping. *Science Translational Medicine* **5**, 212ra163-212ra163 (2013).
128. Amir, E. D. *et al.* viSNE enables visualization of high dimensional single-cell data and reveals phenotypic heterogeneity of leukemia. *Nature Biotechnology* **31**, 545–552 (2013).
129. Lloyd, A. C. The Regulation of Cell Size. *Cell* **154**, 1194–1205 (2013).
130. Davis, J. A. *et al.* Deterministic hydrodynamics: Taking blood apart. *PNAS* **103**, 14779–14784 (2006).
131. W. Inglis, D. *et al.* Microfluidic device for label-free measurement of platelet activation. *Lab on a Chip* **8**, 925–931 (2008).
132. S. Kuntaegowdanahalli, S., S. Bhagat, A. A., Kumar, G. & Papautsky, I. Inertial microfluidics for continuous particle separation in spiral microchannels. *Lab on a Chip* **9**, 2973–2980 (2009).
133. Voldman, J. Electrical Forces for Microscale Cell Manipulation. *Annual Review of Biomedical Engineering* **8**, 425–454 (2006).
134. Huang, L. R., Cox, E. C., Austin, R. H. & Sturm, J. C. Continuous Particle Separation Through Deterministic Lateral Displacement. *Science* **304**, 987–990 (2004).
135. Abkarian, M., Faivre, M. & Stone, H. A. High-speed microfluidic differential manometer for cellular-scale hydrodynamics. *PNAS* **103**, 538–542 (2006).
136. P. Beech, J., H. Holm, S., Adolfsson, K. & O. Tegenfeldt, J. Sorting cells by size, shape and deformability. *Lab on a Chip* **12**, 1048–1051 (2012).
137. Preira, P. *et al.* Passive circulating cell sorting by deformability using a microfluidic gradual filter. *Lab on a Chip* **13**, 161–170 (2013).
138. Holmes, D. *et al.* Separation of blood cells with differing deformability using deterministic lateral displacement. *Interface Focus* **4**, 20140011 (2014).
139. C. Hodgson, A. *et al.* A microfluidic device for characterizing nuclear deformations. *Lab on a Chip* **17**, 805–813 (2017).

140. Wakatsuki, T., Schwab, B., Thompson, N. C. & Elson, E. L. Effects of cytochalasin D and latrunculin B on mechanical properties of cells. *Journal of Cell Science* **114**, 1025–1036 (2001).
141. Cho, Y. H., Yamamoto, T., Sakai, Y., Fujii, T. & Kim, B. Development of microfluidic device for electrical/physical characterization of single cell. *Journal of Microelectromechanical Systems* **15**, 287–295 (2006).
142. Chen, J. *et al.* A microfluidic device for simultaneous electrical and mechanical measurements on single cells. *Biomicrofluidics* **5**, 014113 (2011).
143. Wang, K. *et al.* Specific membrane capacitance, cytoplasm conductivity and instantaneous Young's modulus of single tumour cells. *Scientific Data* **4**, 170015 (2017).
144. Zhou, Y. *et al.* Characterizing Deformability and Electrical Impedance of Cancer Cells in a Microfluidic Device. *Anal. Chem.* **90**, 912–919 (2018).
145. Zmijan, R. *et al.* High throughput imaging cytometer with acoustic focussing. *RSC Advances* **5**, 83206–83216 (2015).
146. Kalb, D. M. *et al.* Line-Focused Optical Excitation of Parallel Acoustic Focused Sample Streams for High Volumetric and Analytical Rate Flow Cytometry. *Anal. Chem.* **89**, 9967–9975 (2017).
147. Raj, A., Dixit, M., Doble, M. & K. Sen, A. A combined experimental and theoretical approach towards mechanophenotyping of biological cells using a constricted microchannel. *Lab on a Chip* **17**, 3704–3716 (2017).
148. Lindken, R., Rossi, M., Große, S. & Westerweel, J. Micro- Particle Image Velocimetry (μPIV): Recent developments, applications, and guidelines. *Lab on a Chip* **9**, 2551–2567 (2009).
149. Raffel, M. *et al. Particle Image Velocimetry: A Practical Guide*. (Springer, 2018).
150. Wereley, S. T. & Meinhart, C. D. Recent Advances in Micro-Particle Image Velocimetry. *Annual Review of Fluid Mechanics* **42**, 557–576 (2010).
151. Ljosa, V. *et al.* Comparison of Methods for Image-Based Profiling of Cellular Morphological Responses to Small-Molecule Treatment. *J Biomol Screen* **18**, 1321–1329 (2013).
152. Boutros, M., Heigwer, F. & Laufer, C. Microscopy-Based High-Content Screening. *Cell* **163**, 1314–1325 (2015).
153. Aubin, J., Ferrando, M. & Jiricny, V. Current methods for characterising mixing and flow in microchannels. *Chemical Engineering Science* **65**, 2065–2093 (2010).
154. Devasenathipathy, S., Santiago, J. G., Wereley, S. T., Meinhart, C. D. & Takehara, K. Particle imaging techniques for microfabricated fluidic systems. *Exp Fluids* **34**, 504–514 (2003).
155. Wu, J. & Gu, M. Microfluidic sensing: state of the art fabrication and detection techniques. *JBO* **16**, 080901 (2011).
156. Wu, J., Zheng, G. & Man Lee, L. Optical imaging techniques in microfluidics and their applications. *Lab on a Chip* **12**, 3566–3575 (2012).
157. Zhu, Y. & Fang, Q. Analytical detection techniques for droplet microfluidics—A review. *Analytica Chimica Acta* **787**, 24–35 (2013).
158. Heo, Y. J., Lee, D., Kang, J., Lee, K. & Chung, W. K. Real-time Image Processing for Microscopy-based Label-free Imaging Flow Cytometry in a Microfluidic Chip. *Scientific Reports* **7**, 11651 (2017).

159. Jeong, J., Frohberg, N. J., Zhou, E., Sulchek, T. & Qiu, P. Accurately tracking single-cell movement trajectories in microfluidic cell sorting devices. *PLOS ONE* **13**, e0192463 (2018).
160. Mudanyali, O. *et al.* Compact, light-weight and cost-effective microscope based on lensless incoherent holography for telemedicine applications. *Lab Chip* **10**, 1417–1428 (2010).
161. Su, T.-W., Erlinger, A., Tseng, D. & Ozcan, A. Compact and Light-Weight Automated Semen Analysis Platform Using Lensfree on-Chip Microscopy. *Anal. Chem.* **82**, 8307–8312 (2010).
162. Su, T.-W., Xue, L. & Ozcan, A. High-throughput lensfree 3D tracking of human sperms reveals rare statistics of helical trajectories. *PNAS* **109**, 16018–16022 (2012).
163. Redmon, J., Divvala, S., Girshick, R. & Farhadi, A. You Only Look Once: Unified, Real-Time Object Detection. *arXiv:1506.02640 [cs]* (2015).
164. [1612.08242] YOLO9000: Better, Faster, Stronger. https://arxiv.org/abs/1612.08242.
165. Redmon, J. & Farhadi, A. YOLOv3: An Incremental Improvement. *arXiv:1804.02767 [cs]* (2018).
166. Tahara, T., Quan, X., Otani, R., Takaki, Y. & Matoba, O. Digital holography and its multidimensional imaging applications: a review. *Microscopy (Oxf)* **67**, 55–67 (2018).
167. Ozcan, A. & McLeod, E. Lensless Imaging and Sensing. *Annual Review of Biomedical Engineering* **18**, 77–102 (2016).
168. Lindquist, N. C. An Introduction to Lensless Digital Holographic Microscopy. in *Miniature Fluidic Devices for Rapid Biological Detection* (eds. Oh, S.-H., Escobedo, C. & Brolo, A. G.) 147–170 (Springer International Publishing, 2018). doi:10.1007/978-3-319-64747-0_6.
169. Goodman, J. W. *Introduction to Fourier Optics*. (Roberts and Company Publishers, 2005).
170. Wu, Y. & Ozcan, A. Lensless digital holographic microscopy and its applications in biomedicine and environmental monitoring. *Methods* **136**, 4–16 (2018).
171. Chanchal, Panigrahi, P. K. & Panigrahi, P. K. Comparison Between Digital Inline and Off-axis Holography System for Particle field Characterization. in *13th International Conference on Fiber Optics and Photonics (2016), paper W3A.8* W3A.8 (Optical Society of America, 2016). doi:10.1364/PHOTONICS.2016.W3A.8.
172. Wang, F., Wang, D., Rong, L., Wang, Y. & Zhao, J. In-line and off-axis hybrid digital holography. in *Unconventional Optical Imaging* vol. 10677 106771Q (International Society for Optics and Photonics, 2018).
173. Flewellen, J. L., Zaid, I. M. & Berry, R. M. A multi-mode digital holographic microscope. *Review of Scientific Instruments* **90**, 023705 (2019).
174. Deng, Y. & Chu, D. Coherence properties of different light sources and their effect on the image sharpness and speckle of holographic displays. *Scientific Reports* **7**, 1–12 (2017).
175. Liu, J.-P., Tahara, T., Hayasaki, Y. & Poon, T.-C. Incoherent Digital Holography: A Review. *Applied Sciences* **8**, 143 (2018).
176. Isikman, S. O. *et al.* Color and monochrome lensless on-chip imaging of Caenorhabditis elegans over a wide field-of-view. *Lab Chip* **10**, 1109–1112 (2010).
177. Rivenson, Y., Wu, Y. & Ozcan, A. Deep learning in holography and coherent imaging. *Light: Science & Applications* **8**, 85 (2019).
178. Pitkäaho, T., Manninen, A. & Naughton, T. J. Focus prediction in digital holographic microscopy using deep convolutional neural networks. *Appl. Opt., AO* **58**, A202–A208 (2019).

179. Rivenson, Y., Zhang, Y., Günaydın, H., Teng, D. & Ozcan, A. Phase recovery and holographic image reconstruction using deep learning in neural networks. *Light: Science & Applications* **7**, 17141 (2018).
180. Wu, Y. *et al.* Extended depth-of-field in holographic imaging using deep-learning-based autofocusing and phase recovery. *Optica, OPTICA* **5**, 704–710 (2018).
181. Wu, Y. *et al.* Bright-field holography: cross-modality deep learning enables snapshot 3D imaging with bright-field contrast using a single hologram. *Light: Science & Applications* **8**, 1–7 (2019).
182. Liu, T. *et al.* Deep learning-based super-resolution in coherent imaging systems. *Scientific Reports* **9**, 1–13 (2019).
183. Liu, T. *et al.* Deep learning-based color holographic microscopy. *Journal of Biophotonics* **12**, e201900107 (2019).
184. Im, H. *et al.* Design and clinical validation of a point-of-care device for the diagnosis of lymphoma via contrast-enhanced microholography and machine learning. *Nature Biomedical Engineering* **2**, 666 (2018).
185. Mateos-Pérez, J. M. *et al.* Comparative evaluation of autofocus algorithms for a real-time system for automatic detection of Mycobacterium tuberculosis. *Cytometry Part A* **81A**, 213–221 (2012).
186. Su, H.-W. The development of an automated system for electrical characterization of cells using a novel force balance method. (Massachusetts Institute of Technology, 2012).
187. McConnell, G. *et al.* A novel optical microscope for imaging large embryos and tissue volumes with sub-cellular resolution throughout. *eLife* **5**, e18659 (2016).
188. Su, T., Seo, S., Erlinger, A., Tseng, D. & Ozcan, A. Towards Wireless Health: Lensless On-Chip Cytometry. *Optics & Photonics News, OPN* **19**, 24–24 (2008).
189. Ozcan, A. & Demirci, U. Ultra wide-field lens-free monitoring of cells on-chip. *Lab on a Chip* **8**, 98–106 (2008).
190. Greenbaum, A. *et al.* Wide-field computational imaging of pathology slides using lens-free on-chip microscopy. *Science Translational Medicine* **6**, 267ra175-267ra175 (2014).
191. Zheng, G., Horstmeyer, R. & Yang, C. Wide-field, high-resolution Fourier ptychographic microscopy. *Nature Photonics* **7**, 739–745 (2013).
192. Aidukas, T., Eckert, R., Harvey, A. R., Waller, L. & Konda, P. C. Low-cost, sub-micron resolution, wide-field computational microscopy using opensource hardware. *Sci Rep* **9**, 1–12 (2019).
193. Apichitsopa, N., Jaffe, A. & Voldman, J. Multiparameter cell-tracking intrinsic cytometry for single-cell characterization. *Lab on a Chip* **18**, 1430–1439 (2018).
194. Pinto, N., Cox, D. D. & DiCarlo, J. J. Why is Real-World Visual Object Recognition Hard? *PLOS Computational Biology* **4**, e27 (2008).
195. Zhao, Z.-Q., Zheng, P., Xu, S.-T. & Wu, X. Object Detection With Deep Learning: A Review. *IEEE Transactions on Neural Networks and Learning Systems* **30**, 3212–3232 (2019).
196. Rosenbluth, M. J., Lam, W. A. & Fletcher, D. A. Force Microscopy of Nonadherent Cells: A Comparison of Leukemia Cell Deformability. *Biophysical Journal* **90**, 2994–3003 (2006).
197. Lam, W. A., Rosenbluth, M. J. & Fletcher, D. A. Chemotherapy exposure increases leukemia cell stiffness. *Blood* **109**, 3505–3508 (2007).

198. Wang, G. *et al.* Microfluidic cellular enrichment and separation through differences in viscoelastic deformation. *Lab on a Chip* **15**, 532–540 (2015).
199. Islam, M. *et al.* Microfluidic cell sorting by stiffness to examine heterogenic responses of cancer cells to chemotherapy. *Cell Death & Disease* **9**, 1–12 (2018).
200. Spencer, D., Elliott, G. & Morgan, H. A sheath-less combined optical and impedance micro-cytometer. *Lab on a Chip* **14**, 3064–3073 (2014).